Technical University of Denmark

DTU

Alternative Actuation and Detection Principles for Resonating Cantilevers

Grigorov, Alexander; Boisen, Anja

Publication date:
2006

Document Version
Early version, also known as pre-print

Link back to DTU Orbit

Citation (APA):
Grigorov, A., & Boisen, A. (2006). Alternative Actuation and Detection Principles for Resonating Cantilevers.

DTU Library
Technical Information Center of Denmark

Alternative actuation and detection principles for resonating cantilevers

Ph.D. Thesis
Alexander Vladimirov Grigorov[1]

16 May 2006
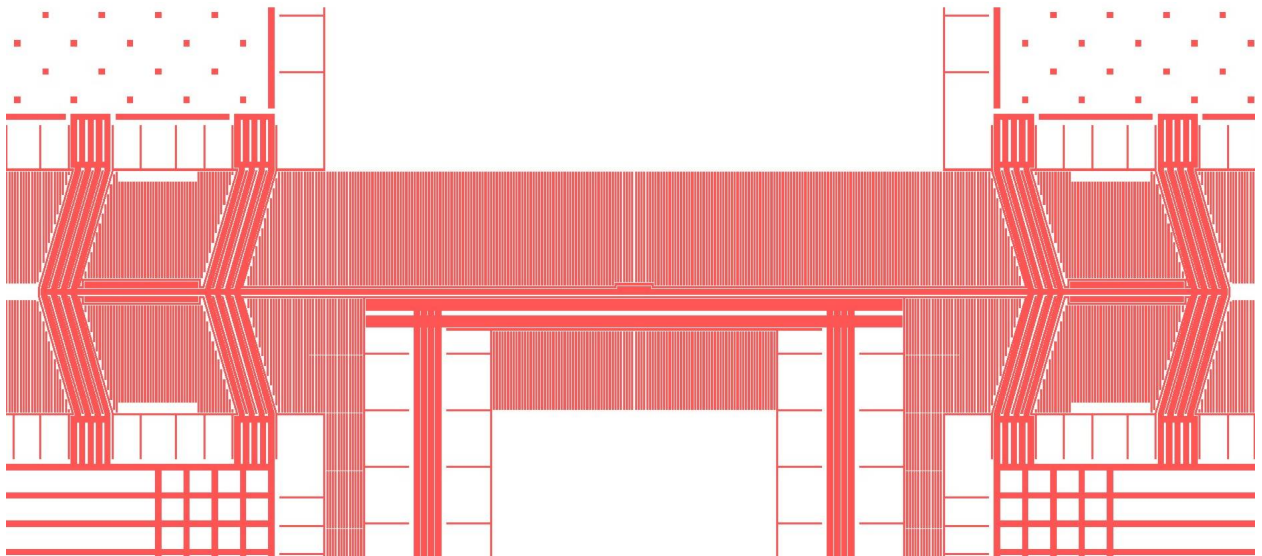
[1]MIC – Department of Micro and Nanotechnology, Technical University of Denmark, DTU-Bldg 345E

DK-2800 Kgs. Lyngby, Denmark

Preface

This thesis was completed as a part of the requirements for obtaining a Ph.D. degree; a Ph.D. degree is useful if one wants to do science, like I do.

The work that I have done and described in this thesis was the biggest motivation I had in doing it, in the vain hope of making the world a better place and being famous. I would like to thank the Danish government for funding it, and Technical University of Denmark for the scholarship that made it possible.

I would like to thank the following people for their help and support throughout the three years of my project:

- Prof. Anja Boisen, my supervisor, for providing the initial connection and support in coming to Denmark, scholarship application, and allowing me to do what I liked scientifically

- Prof. Winnie Svendsen and Rasmus Sandberg for the moral and scientific support with device characterization

- Morten Fugl for being invaluable at automating measurements

- Peter Andreas Rasmussen for spending a month with me in the cleanroom to get me started, and for fruitful discussions on bulk and surface stress.

- Yvonne Gyrsting for being exceptionally helpful with cleanroom work and processing related problems

- Prof. Ole Hansen, for help with measurement theory, and giving my initial project idea a go

- Peixiong Shi, for all the help with E-beam fabrication, and for being Peixiong Shi

- Pieter Telleman for his moral and financial support

- Vladimir Grigorov for the many useful discussions on engineering or electronics related problems in my research.

- All present and former members of the Bioprobes/Nanoprobes group

Alexander Vladimirov Grigorov, May 16, 2006

MIC – Department of Micro and Nanotechnology
Technical University of Denmark, DTU – Bldg. 345 East
DK-2800 Kgs. Lyngby
Denmark

Abstract

Micro-electro mechanical systems (MEMS) are an emerging technology with a big potential for commercial applications in for general and biochemical sensing and biomolecular detection. Cantilever sensors are and existing MEMS concept that can be used for sensing and detection by either static surface stress detection, induced by a bimolecular interactions, or by mass-detection using resonance detection.

The goal of this research has been to invent, discover and research alternative actuation and detection principles for resonating cantilevers.

In our research, we adhered to fixed set of research values that we believe would make its products commercially competitive. We researched only planar, one mask devices, strove to limit the number of processing steps and aimed for device designs that use as little as possible external equipment in the form of electronics, for field measurements.

We invented a new dynamic electro-thermal actuation principle and researched its performance experimentally and theoretically. A device that is actuated using the above principle was then characterized using laser/optical detection and we performed basic mass measurements.

We discovered a new detection principle (rupture detection) to be used in conjunction with an electro-thermally actuated cantilever, performed resonant frequency detection and performed basic characterization of the new detection method.

General research into resonant MEMS devices that are not plain cantilevers was also attempted and yielded a device that is actuating.

In order to improve our existing device designs we then made a transition from UV lithography fabrication to electron beam lithography fabrication. This fabrication method is expensive depending on writing time, so we strove to reduce this with innovative processing solutions such as dot patterning and outline writing. We researched metal fabrication of suspended structures and invented a new process involving top layer peel-of an angled deposition. We applied this process to fabrication of beam structures that have Z-shaped, U-shaped, and rectangular cross sections.

The novel structures and process were than used for system level integration and possible functionalization of devices for static and dynamic measurements using solid and suspended channels, spotting, and capillary action to make various fluids flow along.

Dansk Resume

Mikro-elektro mekaniske systemer (MEMS) er ny en teknologi med stort potentiale for kommerciel anvendelse indenfor såvel generel og biokemisk som biomolekylær detektion. Cantilever sensorer er et eksisterende MEMS koncept, der kan bruges til detektion af enten statisk overfladestress fremkaldt af et bimolekylært samspil eller minutiøs masseændring ved resonansbestemmelse.

Formålet med denne forskning har været at opfinde, opdage og undersøge alternative påvirknings- og detektionsprincipper af cantilevers drevet i resonans tilstanden.

I vores forskning har vi holdt os til et fast sæt forskningsværdier, som vi mener ville gøre produkterne kommercielt konkurrencedygtige. Vi undersøgte kun enkelt-maske planar komponenter, forsøgte at begrænse antallet af behandlingstrin og sigtede efter element designs der så lidt som muligt bruger eksternt elektronisk udstyr til aktuelle målinger.

Vi opfandt et nyt dynamisk elektro-termisk aktiveringsprincip og undersøgte dets ydeevne både i praksis og teoretisk. En komponent der bringes til resonans ved hjælp af det ovennævnte princip blev derefter karakteriseret ved hjælp af laser/optisk detektion, og vi udførte basale massemålinger.

Vi opdagede et nyt detektionsprincip (gennemslagsprincippet), som brugtes i forbindelse med en elektro-termisk betjent cantilever, udførte resonansfrekvens bestemmelse samt basal karakterisering af den nye detektionsmetode.

Generel forskning i resonans MEMS apparater som ikke er rene cantilevers blev også forsøgt og frembragte et styrende apparat.

For at kunne forbedre vores eksisterende instrument designs gik vi fra UV litografi fabrikation til elektronstråle litografi fabrikation. Omkostningerne ved denne fremstillingsmetode er afhængig af skrivetiden, derfor bestræbte vi os på at reducere denne med innovative procesløsninger som punktstrukturering og omrids skrivning. Vi undersøgte metal fabrikationen af hængende strukturer og opfaldt en ny proces, der involverer top-lag-afskrælning af en vinklet deponering. Vi anvendte denne proces til fremstillingen af vippe strukturer, der har z-formede, u-formede og rektangulære tværsnit.

De nye strukturer og processer blev derefter brugt til integration på system niveau og mulig funktionalisering af enheder til statiske og dynamiske målinger, der bruger solide og afbrudte kanaler, "spotting", og kapilær handlinger til at få diverse væsker til at flyde.

Table of Contents

List of Figures

List of Tables

Chapter 1

Introduction

1.1 Motivation

Micro electro-mechanical systems (MEMS) can be applied to a wide range of existing product applications where a MEMS-based system replaces a bulkier non-integrable device; MEMS technology also offers immense possibilities for future applications such as sensing and nano-scale manipulation.

At present, there are few commercially successful MEMS devices and systems. Inc-jet and bubble-jet printer heads [1], digital projectors [2,3,4], accelerometers [5,6] and AFM cantilevers [7] are some of the few micro-electro-mechanical devices that have succeeded in a competitive market environment or displaced an older technology. There are some emerging MEMS based products that might prove to be superior to existing technology in the future, such as the Millipede ™ project [8] that aims to offer better cost/data storage ratio than existing options such as flash memory.

MEMS sensors for general and biological applications have so far been unsuccessful commercially; individual MEMS devices that are capable of detecting specific bio-molecular interactions, have been unable, so far, to offer an advantage of over existing technology from a system point of view

For instance, at present Surface Plasmon Resonance (SPR) is one of the dominant market technologies when it comes to bio-molecular interactions sensing and measurements [9]. From a system point of view SPR equipment incorporates a laser, optics, electronics and fluidic devices (pumps and tubes). The actual sensing part is a chip that is effectively a gold layer covered glass slide.

So, we believe that a MEMS based system that aims to be competitive on the free-market for general sensing and bio-chemical application should strive to be as simple as a gold covered glass slide when it comes to the sensing element, and eliminate as much of the external off-chip equipment as possible, i.e. offer a system advantage.

Hence, we strove to keep the MEMS devices that we have researched as simple and cheep as possible, while aiming to use as little as possible external equipment and electronics for measurements.

To do this, we restricted our research to planar devices, that need only one lithography step for fabrication (one mask, no alignment), and strove to limit the number of fabrication steps.

We resolved to look for on-chip MEMS solutions to problems that are otherwise solvable by external equipment (electronics etc.)

We also took an inventive approach to research, aiming to only explore devices, actuation and detection methods that have not been done before, the rationale being that innovative and original solutions, devices and systems create their own market niches.

Our goal in this research was to invent, discover and research alternative actuation and detection principles for resonating cantilevers, using the cheapest possible device and system implementation.

1.2 Cantilever sensors

One of the simpler MEMS bases sensor devices is a micro/nanometer sized cantilever sensor.

Microcantilever sensors were introduced with the invention of the atomic force microscope (AFM) by Binnig et al. [7] in 1986; and development, characterization and application of micro- and nanocantilevers has since then become a continuously expanding, global field of research, mainly because of their potential as low-cost and high-sensitivity measurement probes.

Cantilever sensing falls into two basic categories – static and dynamic.

1.2.1 Static cantilever sensors

Static cantilever sensors aim to measure a deflection of a suspended cantilever device, that is induced by surface stress on one of the cantilever sides [10]. Bimolecular layers usually result in surface stress, so, static cantilever devices can be used as bio-sensors. There are two dominant means for static cantilever detection – optical [11] and piezo-resistive [12].

Piezo-resistive detection is implementable as a strain-gauge fabricated within the cantilever side that is to be functionalized.

Optical sensing can take many different forms. In its most basic form a laser beam is deflected of a reflective side of a cantilever device – in this sense the cantilever device acts as an optical element (a mirror). Minute cantilever deflections result in large changes of the laser trajectory, so, at a distance those deflections can be measured using a photo-detector, or a CDD array [13].

One could also use interferometry [14] and detect a change in cantilever curvature. And last but not least an optical wave guide integrated on a cantilever could also provide the means for deflection measurements [15].

Biomaker proteins and transcription factors detection has successfully been demonstrated using static cantilever sensors with sensitivities of 20 µg ml^{-1} and 80-100 nM respectively [16, 17]

1.2.2 Dynamic cantilever sensors

General theory

Dynamic cantilever sensing aims to measure a resonant frequency shift due to a mass or elasticity change. Resonant cantilevers can be used as mass sensors by actuating them around a resonant frequency and monitoring the frequency response in terms of vibration amplitude and phase shift.

The cantilever surface can be coated with a functionalization layer for adsorption of specific chemical compounds. Adsorbed molecules will add to the mass of the cantilever and the resulting frequency shift can be detected.

Resonance phenomena in general are based on the same basic theory, which is best illustrated with a mass on a spring under the influence of dampening and an external harmonic force [18]. Newtons 2nd law for this phenomena is

$$m\,a = -k\,x - \lambda\,v + F_0 \cos(\omega_f t) \tag{1.1}$$

where m is the mass, k the spring constant, λ the damping, F_0 the external force and ω_f its angular frequency. It can be rewritten into

$$\frac{d^{2x}}{dt^2} + \gamma\,\frac{dx}{dt} + \omega_0^2 x = \frac{F_0}{m}\cos(\omega_f t) \tag{1.2}$$

where $\omega_0 = \sqrt{\dfrac{k}{m}}$ is the systems Eigen frequency and $\gamma = \lambda/m$. The stationary solution for the above equation is

$$x = A_0 \cos(\omega_f t - \alpha) \tag{1.3}$$

for large t when the transient has died out. A_0 is the amount of oscillation (amplitude). The frequency where it is largest is the resonant frequency. The phase α and the amplitude A_0 are defined by

$$\tan\alpha = \frac{\gamma\,\omega_f}{\omega_0^2 - \omega_f^2} \tag{1.4}$$

and

$$A_0 = \frac{F_0/m}{\sqrt{(\omega_0^2 - \omega_f^2)^2 + \gamma^2 \omega_f^2}} \tag{1.5}$$

An approximation to the resonance frequency change Δf when a mass Δm is applied at the tip of rectangular cantilever is [19]

$$\frac{-\Delta f}{f_0} \approx \frac{1}{2}\frac{\Delta m}{m_0} \tag{1.6}$$

where f_0 is the initial resonance frequency and m_0 the initial mass of the cantilever (Figure 1.1).
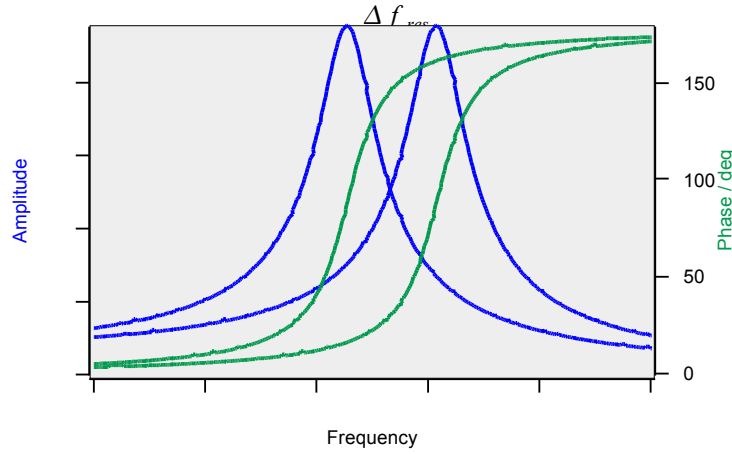
Figure 1.1: Amplitude and phase resonant shift due to mass change

A model for the correspondence between the resonance frequency in vacuum (f_{vacuum}) and in a fluid (f_{fluid}) is [20]

$$\frac{f_{vacuum}}{f_{fluid}} = \sqrt{1 + \frac{\pi \rho_{fluid}\, h}{4 \rho_{cantilever}\, w}} \qquad (1.7)$$

where w is width of the cantilever, h - height of the cantilever, ρ_{fluid} - the density of the surrounding fluid, $\rho_{cantilever}$ - the density of the cantilever material. This can be rearranged into an expression for the relationship between two fluids

$$\frac{f_{fluid1}}{f_{fluid2}} = \sqrt{\frac{1 + \dfrac{\pi \rho_{fluid2}\, w}{4 \rho_{cantilever}\, h}}{1 + \dfrac{\pi \rho_{fluid1}\, w}{4 \rho_{cantilever}\, h}}} \qquad (1.8)$$

For a plain rectangular cantilever clamped at one side, the resonant frequency is determined by the cantilever geometrical and material properties:

$$f_{res} = \frac{\omega_o}{2\pi} = \frac{1}{2\pi}\sqrt{\frac{k}{m_{eff}}}$$

$$k = \frac{Ehw^3}{4l^3}, \quad m_{eff} = \frac{3m}{C_n^4} \quad (C_n = 1.875,\ 4.694..), \quad m = \rho\, lwh \qquad (1.9)$$

$$f_{res} = \frac{C_n^2}{4\sqrt{3}\,\pi}\sqrt{\frac{E}{\rho}}\frac{w}{l^2}$$

where E is the cantilever material Young's modulus, h - cantilever height, l - cantilever length, m - cantilever mass, ρ – cantilever material density, C - a dimensionless constant related to the

harmonic mode of oscillation (n), m_{eff}– the effective cantilever mass related to the mode of oscillation.

MEMS based resonant cantilever sensors fall into many sub-categories with respect to various means of actuating a cantilever device to a certain frequency and detecting the phase or amplitude of the movement in order to find the resonant frequency. The most commonly used are described in a review article by Stemme [21].

Actuation methods

There are three basic methods for actuation: electrostatic, electromagnetic and piezoelectric. Electrostatic actuation works by fabricating one or more electrodes in parallel of the cantilever. An alternating voltage signal applied between the cantilever and electrode results in alternating electrostatic potential field that attracts and repels the cantilever at the frequency of the driving signal.
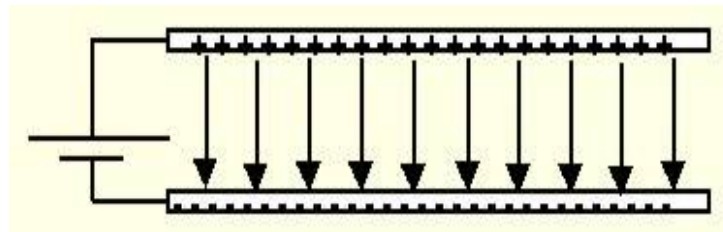
Figure 1.2: Parallel plates capacitor

The force between a parallel capacitor's plates due to the potential difference between the plates (Figure 1.2) is

$$F = \frac{CV^2}{2d} = \varepsilon \frac{AV^2}{2d^2}$$
(1.10)

where C is capacitance, V – applied voltage, d – plate spacing, A – plate area, ε – dielectric constant.

Electromagnetic actuation uses a similar principle where an alternating current is applied to a bridge cantilever device placed in a strong external field, perpendicular to the current vector. A charged particle moving in an electromagnetic field experience a force (Lorenz, left-hand rule), so the cantilever is actuated perpendicularly to the field.

$$F = \int_0^l IBdx = IBl$$
(1.11)

Piezoelectric actuation is the simplest of all actuation mechanisms. A piezoelectric layer can be fabricated either on one of the cantilever sides or a piezoelectric element can be attached externally to a chip [22]. PZT films are most commonly used for fabrication of piezo-electric layers on a cantilever. Piezo-electric materials, however are difficult to fabricate and integrate on a cantilever devices, and are expensive.

Detection methods

Resonant cantilever detection can either be electrostatic, electromagnetic, piezo-resistive or

optical.

An electrostaticly actuated resonant cantilever forms a capacitor with its driving electrode(s). Measuring the capacitative current between cantilever and electrode as the the cantilever oscillates allows to infer the resonant frequency; the current is highest at the resonant frequency, as the cantilever moves closest to the electrode at that frequency due to the high amplitude [23, 24]. Figure 1.3 shows a cantilever between two electrodes, and defines the mechanical and electrical parameters in such a system, for the equations of motion and current (1.12).
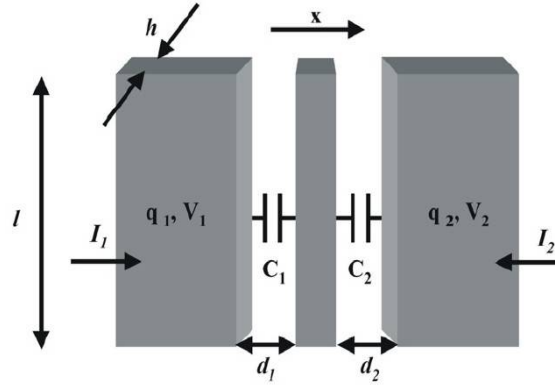
Figure 1.3: Resonant cantilever between two electrodes

$$m\ddot{x} = -\frac{V_1^2 C_1}{2(d_1+x)} + \frac{V_2^2 C_2}{2(d_2+x)} - kx - D\dot{x}$$

$$I_n = C_n V_n + V_n \frac{\partial C_n}{\partial x} \dot{x}$$

(1.12)

V is the potential difference between an electrode an the cantilever, d – the distance at rest between an electrode an the cantilever and C – the capacitance between an electrode and the cantilever, and q is charge for each electrode [25].

An electromagnetically actuated cantilever moves in its actuating field. This induces an EMF within the conductor line formed by the cantilever bridge that is proportional to the movement velocity. Measuring the induced EMF allows to infer the device amplitude and hence determine the resonant frequency [26].

$$EMF = \int_0^L B \frac{dY(x,t)}{dt} dx$$

$$Y(x,t) = Y(x) e^{i\omega t}$$

$$EMF = i\omega \int_0^L BY(x) dx = 1.59 \ i\omega BLY_{mid}$$

(1.13)

where L is the length of a cantilever bridge, Y(x,t) describes the oscillating movement of the cantilever, and B is the external magnetic field.

Piezo-resistive readout for dynamic sensing is similar to the static case. This is effectively a plain cantilever device with and integrated strain-gauge on one of its sides. External resonant actuation

of such a device translates directly to a change in resistance that follows the cantilever amplitude/deflection in time.

Optical detection for dynamic sensing is also in principle the same as for the static sensing case, except that the cantilever is dynamically actuated.

Applications and summary

Applications for resonant cantilever sensors include gas- or vapor-detection of e.g. mercury [27], ethanol [28] or relative humidity [29], and recently Ledermann et al.[30] reported on CO_2 detection of concentrations down to 330 ppm. In the biomolecular area, protein masses of specific antigens have been measured using cantilevers in liquid, with a sensitivity of 100 ng/ml [31], and even liquid in a channeled cantilever has been implemented by Burg et al.[32] with a surface density sensitivity of 10 ag/μm^2 on an channel surface of 53000 μm^2.

As the dimensions of the cantilevers decrease, the sensitivity increases, implying that resonant cantilever sensors have the future potential of detecting the mass of individual molecules. Current state–of–the–art includes demonstrated mass detection in the order of a few ag [33] and fabrication of cantilever sensors with sub-ag estimated mass sensitivities [33, 34].

The only unexplored method for resonant cantilever actuation is planar electro-thermal actuation most commonly used in micro-cantilever manipulators [35]. This provided initial motivation for exploring the principle for dynamic cantilever actuation. Electro-thermal actuation for resonant cantilevers is not a new concept [36], but past work on the subject only explores applications for vertically moving cantilevers that are fabricated using more than one material layer, i.e. fall outside our research motivation values.

A useful application for cantilever sensing is the implementation of resonant cantilever mass detection in a liquid medium. The operation of the cantilever in a liquid poses actuation and detection challenges not present in air measurements; the electrostatic actuation which is most widely used is inefficient in water and also poses physical interference problems with the driving electrode – a acoustic cushion effect and cantilever adhesion. Piezoelectric actuation which is commonly used in atomic force microscopy works well in all media, but it is relatively complex to integrate on the cantilever structure as it involves the use of more than one material (for the structure and for the piezoelectric elements).

Electro-thermal actuation is not subject to such restrictions, so we decided to investigate its implementation for dynamic sensing (Chapter 2). We further characterized a device that is actuated using the above principle using laser/optical detection and we performed basic mass measurements.

We then discovered a new detection principle (rupture detection) to be used in conjunction with an electro-thermally actuated cantilever, performed resonant frequency detection and performed basic characterization of the new detection method.

We also undertook general research into resonant MEMS devices that are not plain cantilevers and discovered a device that is actuating (Chapter 3).

We then made a transition to electron beam lithography fabrication and continued our research into the discovered new actuation and detection principles using metal devices (Chapter 4).

Chapter 2

Dynamic electro-thermal actuation and detection

2.1 Dynamic electro-thermal actuation

2.1.1 Concept overview

Existing work on planar cantilever electro-thermal actuation examines mostly the actuators' static performance, and strives to maximize tip displacement and minimize the DC current. Actuator configurations mimic bimorph actuation, and actuation is achieved along the length of a cantilever, limiting the ability to vary dimensional parameters separately [37].

We propose a new electro-thermal actuator configuration, which can be optimized for static or dynamic performance, separately from the actual device/cantilever dimensions.

It consists of two in-plane resistors perpendicularly connected to the cantilever base, one on each side with a 20 μm offset between the points of connection (Figure 2.1)
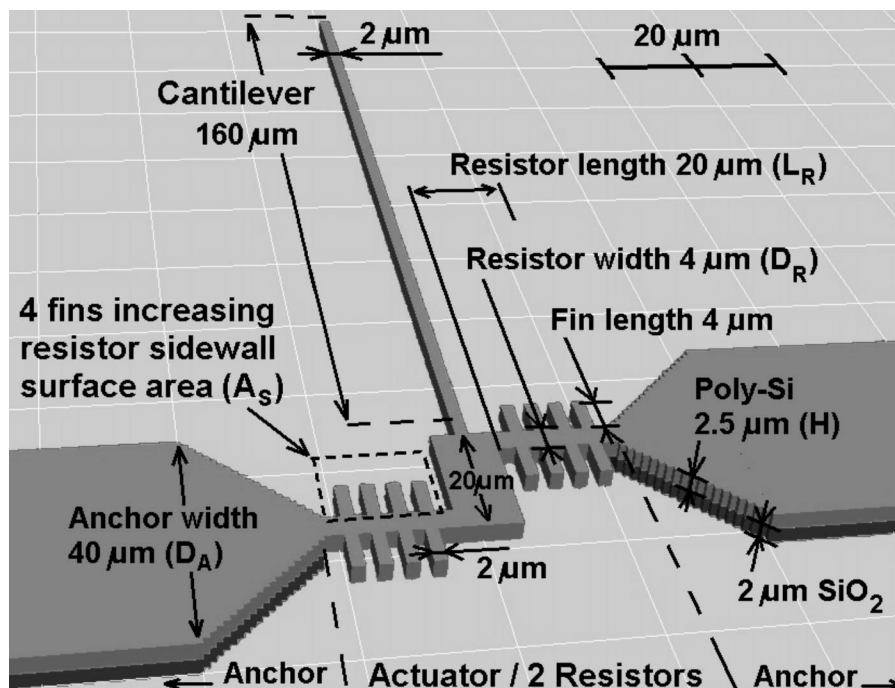
Figure 2.1: Dynamic elector-thermal actuation device schematic and definitions

To operate, a square pulse signal is applied to the resistors. At the peaks of the signal the resistors heat up and expand; at the troughs the resistors cool down and shrink. This longitudinal motion actuates the cantilever laterally at the frequency of the driving signal (Figure 2.2).
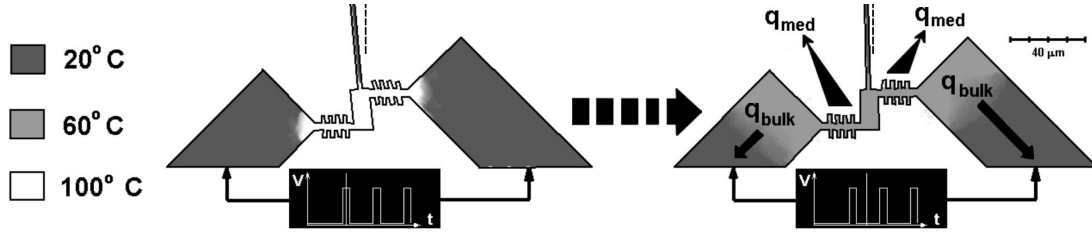
Figure 2.2: Dynamic electro-thermal actuation principle operation

2.1.2 Theoretical investigation

The device ability to actuate dynamically at a certain frequency depends mostly on its ability to cool down between current peaks; a perfectly insulated resistor would remain stationary in a "hot" expanded state. If ΔT is the temperature difference between the medium (at infinity) and the resistor at its hottest state, then we define the maximum actuation frequency (f_{maz}) as the frequency at which the actuator cools down by $\Delta T/2$ between signal peaks. This can be approximated to

$$f_{max} = \frac{1}{t} = \frac{q/(\ln 2)}{Q_{stored}} = \frac{q}{(\ln 2)C_{Si}\Delta T \rho_{si}(2L_R D_R H)} \qquad (2.1)$$

where q is the power output of the device in its hottest state (during a signal peak), and assuming that q depends exponentially on ΔT; C_{SI} is the heat capacity of silicon, ρ_{SI} is the density of silicon, L_R is the resistor length, D_R is the resistor width and H is the resistor height.

Boiling and bubbles might easily destroy the devices so the upper operational temperature limit is 100^0 C for potential water medium operation. This sets $\Delta T = 80K$.

There are two easily distinguishable cooling mechanisms – by heat conduction to the anchor and substrate (q_{bulk})and by convection to the medium (q_{med}), q = q_{bulk} + $q_{med.}$

Using classic fluid dynamic theory, the heat transfer by convection from a vertical plate is given by [38]:

$$q_{med} = h.A_S.\Delta T, \quad h = \frac{k_{medium} Nu}{H}, \quad Nu = \frac{4}{3}\left(\frac{Gr_L}{4}\right)^{0.25} \frac{0.75\,Pr^{0.5}}{\left(0.609 + 1.221\,Pr^{0.5} + 1.238\,Pr\right)^{0.25}} \quad (2.2)$$

($Pr = C_p.\mu / k_{medium}$, $Gr = \beta g\rho^2 H^3 \Delta T / \mu^2$)

Where A_S is the resistor sidewall surface area, k_{medium} is the heat conductivity of the medium, H is the resistor height, Gr and Pr are the respective Grashof and Prandtl numbers for the resistor, C_p is the heat capacity of the medium, μ – the dynamic viscosity of the medium, β – the coefficient of cubical expansion of the medium, g – the acceleration due to gravity and ρ – the density of the medium. For operation in water this gives

h = 101 kW, q_{med} = 0.26 mW.

However, the formula for the Nusselt number (Nu) is probably outside its applicable range, as this is an empirical formula for macro-sized objects.

The heat conductivity of SiO_2 is five orders of magnitude lower than that of polysilicon; hence the heat flux from the resistors to the anchors is confined to the poly-Si layer in the anchors. This

can be used to simplify the problem to that of 1D heat conduction along an insulated bar, one end kept at a constant ΔT_0 (the resistor), the other infinitely long- this is the anchor which is essentially a conductor several millimeters long and 40 µm wide:

$$\Delta T(x,t) = \Delta T_0 \, erfc\left(\frac{x}{2\sqrt{kt}}\right) \qquad (2.3)$$

Integrating this equation from x=0 to x=∞, and then differentiating in time, gives the transient average power necessary to maintain the temperature difference ΔT_0:

$$q_{average}(t) = \Delta T_0 \rho_{si} C_{si} D_A H \cdot \sqrt{\frac{k_{si}}{\pi \, t}} = 4.3 \ mW \quad (\Delta T_0 = 40K, t = 60s) \qquad (2.4)$$

where D_A is the anchor width, H is the anchor height, and t is the total time of operation. ΔT_0 was set at 40 K as this is half the temperature difference between room temperature (20° C) and boiling (100° C). A feasible operating time scale for a measurment is a minute, hence t was set to 60s. For a square pulse signal that has a 1-to-5 time ratio between troughs and peaks this becomes $q_{bulk} = 5q_{average} = 21.5$ mW, assuming that the chosen ratio does not result in transient temperature peaks above 100^0 C.

Assuming that q_{med} and q_{bulk} are independent, $q_{total} = q_{bulk} + q_{med} = 21.76$ mW, and from (2.1):

$f_{max} = 610$ kHz (in water)

$f_{max} = 600$ kHz (in air)

which is higher than the designed resonant frequency of the cantilever which is approx. 80 kHz.

This means that the operation of the actuator is largely independent of the medium as the cooling rate is dominated by the heat conduction term q_{bulk} even in a medium that is has a high heat capacity such as water.

Different mediums, however, will result in different damping on the cantilever itself, reducing the resonant amplitude.

2.1.3 Parametric investigation

In order to investigate the optimal actuator design we took a parametric approach to fabrication; an array of varying actuator design devices were fabricated using a 2.5 µm thick LPCVD polysilicon layer on top of a 2 µm thick oxide layer on a Si substrate. The structures were defined by dry plasma etching of the polysilicon layer and subsequently the oxide was under-etched in HF to release the cantilever and the resistor.

The design parameters that were varied were resistor width (2 or 4 µm), number of fins on resistor sides (0 to 4), fin length (2 or 4 µm) and a single or double actuator design -"L-type" or "Z-type" (Figure 2.3). Figure 2.4 shows all the different resistor/actuator variations that were experimented with for the Z-type devices. L-type devices were varied in a similar fashion.
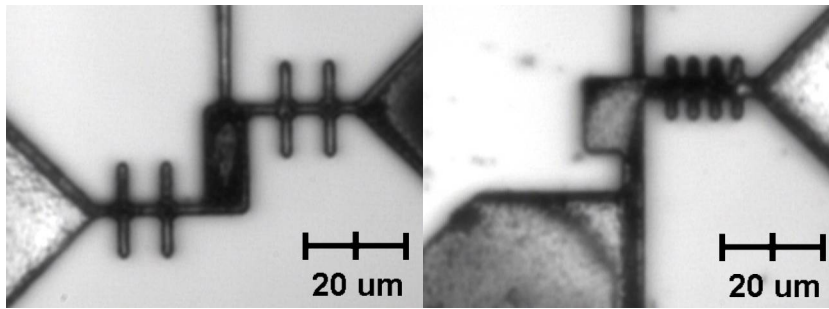
Figure 2.3: Z-type and L-type actuator designs

A third arrangement was considered ("U-type"), that is similar to the Z-type but has both resistors on the same side. This was rejected, as it would have had a large parasitic resistance and capacitance, due to the close proximity of the resistors.
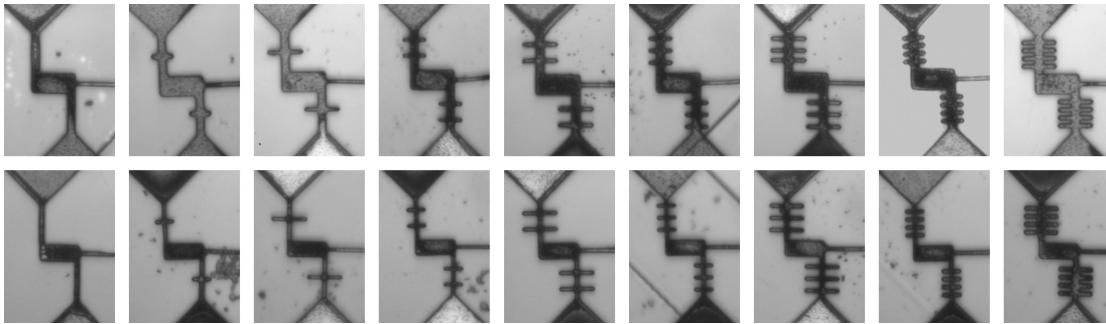
Figure 2.4: Actuator parametric variations (Z-type)

The power input/output of the different designs were measured at 100^0 C in water. DC voltage was applied to the resistors, at the same time observing them under a microscope. When a bubble appeared the voltage was recorded, and knowing the resistance of the particular device the power input was calculated (Figure 2.5).

The power output (i.e. dissipated heat at the resistor) is equal to the power input minus the power dissipated due to the parasitic resistance of the device. The parasitic resistance was measured by breaking a device off its anchors and measuring the resistance again in water. Device resistances varied between 1.6 and 2.3 kΩ in air, while the parasitic resistance was found to be 8 kΩ. Taking the parasitic resistance to be in parallel, the power outputs were calculated. The error in those calculations and measurements is estimated to be up to +-20% for the final result.

The performance, i.e. maximum frequency is dependent on area (surface and cross-sectional), and is inversely dependent on volume. So, to actually compare the devices in terms of performance and not power outputs - the 2 μm resistor width devices power output must be doubled, as they have twice less volume and hence twice less heat stored to be removed. This is not the case for the L-type devices as they have both twice less area and mass, as they have only one resistor.

The resistance of the part where the resistors attach to the cantilever was decreased to prevent heating and thermal expansion of the cantilever base. This was done by widening the cantilever base. The surface areas of the widened cantilever bases were also included in the total sidewall surface area for the devices on the graph. Not all of the device configurations that were fabricated survived the testing, resulting in fewer data points on the power graph.
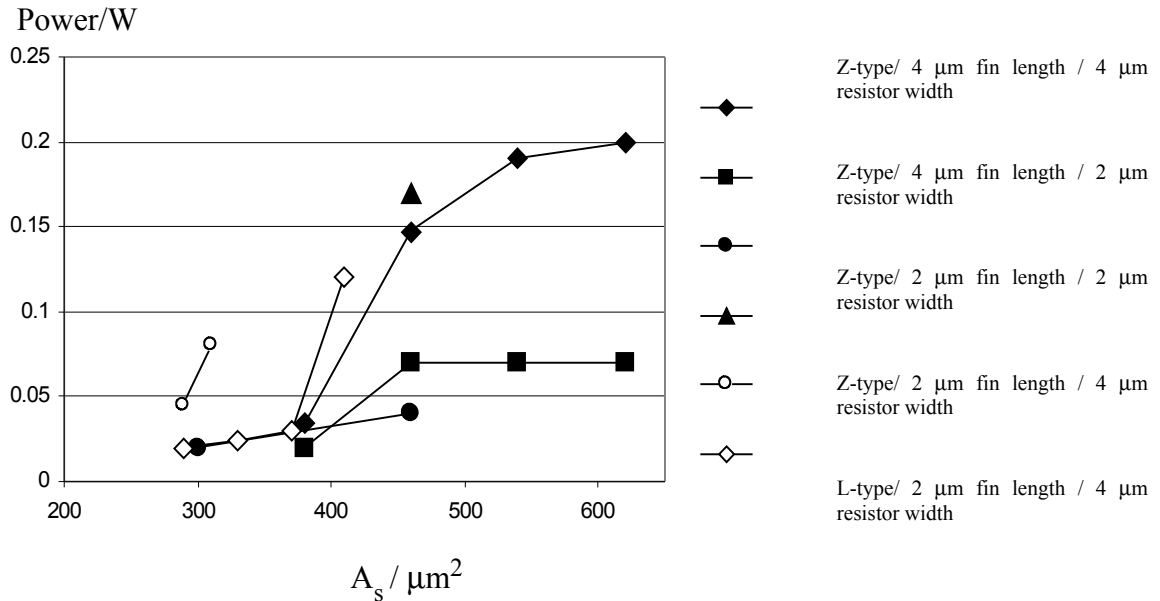
Power/W

Figure 2.5: Power output in water at 100 deg. C vs. sidewall surface area

The power outputs were found to be one order of magnitude larger than the ones calculated theoretically (theoretical q_{bulk} = 0.022 W for all devices, and theoretical q_{med} = 0.26 mW for the largest sidewall area device), suggesting a third power dissipation mechanism or better thermal conduction. Probably, heat is dissipated by convection to the water from the anchors' polysilicon layer that is heated by conduction from the resistor. This in turn increases the thermal gradient in the polysilicon layer making heat conducted from the resistor much larger. It is also possible that the actual Nusselt number of the resistor is larger than the one suggested by the theory for macro size vertical plates, increasing convection. Finally, bubbles appear when the surface of the resistor is above 100 deg. C. However, the center of the bulk of the resistor might be at a higher temperature, again increasing the actual thermal conduction in the polysilicon layer

The graph (Figure 2.5) shows that there is a step-change in power dissipation at around 380 μm^2 for most devices, meaning that above 380 μm^2 a power-dissipation mechanism is activated. However, the step change is larger for the devices with larger cross-sectional area. This suggests that larger cross-sectional area is not only better for heat conduction to the polysilicon layer, but also for heat conduction along the cantilever and into the fins to be carried away by convection. This is further evident on the graph, as the transition occurs at a lower total surface area for the "L-type/2μm fins/4μm resistor" devices compared to the other "4μm fins/4μm resistor" devices. For example it is better to have 4 short fins than 2 long fins of the same total area, as heat would travel less distance along the resistor before reaching a fin, and the thermal gradient would be steeper making heat conduction faster.

The "Z-type/4μm fins/4μm resistor/4 fin pairs per resistor" device has the highest power output – 0.2W. This gives a maximum actuation frequency in water of f_{max} = 11.5 MHz (2.1) . This result is an order of magnitude higher than the required 80 kHz to actuate the design 160 μm long and 2 μm wide polysilicon cantilever to resonance.

As to resonance in air, one can assume that the lowest point on the power graph (0.02 W) is the power output that is mainly due to conduction to the substrate. This is also in good accordance

with out theoretical estimate of the heat output due to conduction (q_{bulk}= 0.022 W). Taking the dominant cooling mechanism in air to be conduction, and putting q = 0.02W gives a maximum actuation frequency in air of 1.12 MHz (2.1). Static deflection at the tip of the cantilever at 100 deg. C was also measured in water using the same setup. It was found to be approximately 0.4 μ m.

2.1.4 Experimentation

In order to design the best detection mechanism for possible fluid medium sensing, it is necessary to have knowledge of the Q-factor and the maximum amplitude at resonance in water. In order to calculate these, measurements in air were performed using the largest power output actuator configuration using optical inspection.

Figure 2.7: Q-factor in air by optical inspection

Figure 2.6: Resonance in air

Resonance for the particular device was observed at 54 kHz and the Q factor was determined to be 21 (Figures 2.6 and 2.7). The amplitude was measured on a computer screen image connected to a microscope camera. The input signal used was 20 V zero-to-peak square pulses, with 1-to-5 time ratio between pulses and troughs.

This is lower than the calculated resonant frequency of 80 kHz and is probably due to lower Young's modulus of the material or slightly larger cantilever thickness, than the numbers used in the calculation.

For this particular cantilever design, the experimental results in air suggest resonance at 37 kHz, Q=3, and maximum amplitude of about 0.9 μm in water, using the theory developed by Kirstein et al. [39]. The device was also tested in water, but the resonance wasn't observed. However, it is difficult to focus a microscope at the tip when it is in water, and the focus drifts due to evaporation, so an amplitude of 0.9 μm is probably beyond what is observable with a standard optical microscope underwater.
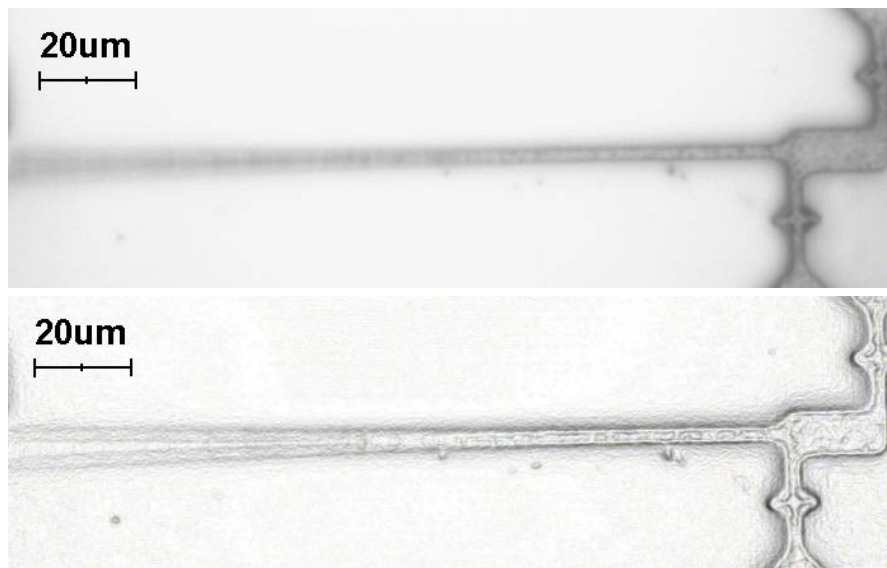
Figure 2.8: Digital filtering of an individual frame example

The theoretical calculations for the maximum actuation frequency in air were also tested using a "Z-type/2µm fins/2µm resistor/1 fin pairs per resistor" actuator devices. Pictures of the resonating cantilever were taken at discrete frequency steps, digitally filtered to restore the cantilever shape and the resonant amplitude was measured in each individual picture. Figure 2.9 gives an example of one such frame.

The individual amplitude measurements were then used to create an input signal frequency vs. amplitude graph (Figure 2.10).
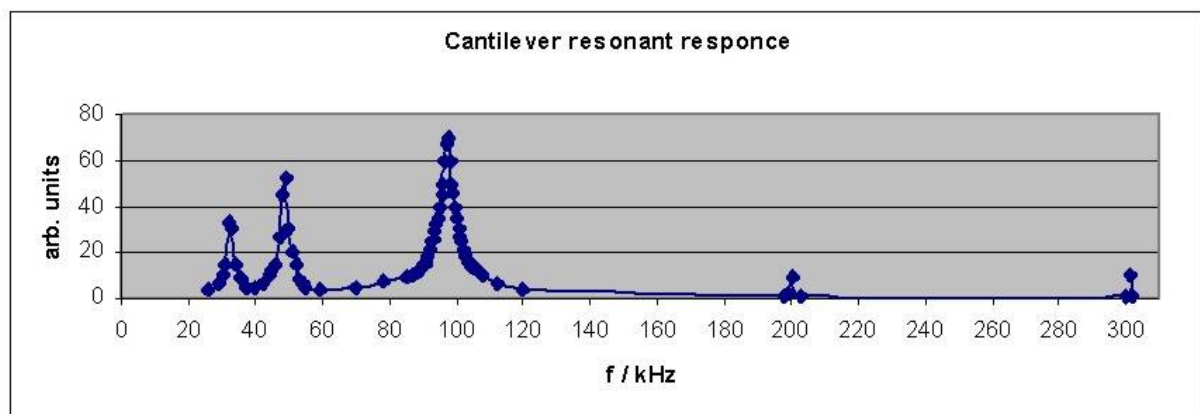
Figure 2.9: Amplitude vs. frequency by frequency scanning and digital filtering

It must be noted that the resonant peaks are one and the same harmonic, i.e. the cantilever is resonating at 100 kHz. This harmonic, however, is also induced at driving signal frequencies that are fractions or multiples of the base resonant frequency – 33, 50, 200 and 300 kHz.

This allowed us to verify the order of magnitude for the theoretical and experimental maximum actuation frequency, we observe resonant actuation at 300 kHz, which is twice less than our theoretical estimate of 600 kHz and four times less than our experimental estimate of 1150 kHz.

2.1.5 Applications and summary

The resonant frequency of a cantilever is inversely proportional to its size ($f \propto W/L^2$). The heat stored in the resistors depends on their volume, i.e. cubically proportional to size. The heat transfer to the substrate is proportional to the cross-sectional area of the resistors, i.e. quadratically proportional to size. Hence both the resonant frequency and the maximum actuating frequency increase linearly as size goes down, and the actuation principle is fully scalable. This allows scaling down the device to reduce its power requirements, which are quite high at the moment, without compromising performance. Scaling down is also desirable for better mass-detection resolution.

While in theory the actuator design performs better in a fluid medium, the cantilever itself is subject to damping that reduces its sensitivity as scale goes down. Therefore, when it comes to applications and actual mass sensing the concept is only applicable to gas medium sensing and lends itself improvement by down-scaling only in a gas medium.

2.2 Rupture detection

Rupture detection is a novel method for resonant cantilever detection that we discovered and implemented for use in conjunction with an electro-thermally actuated cantilever.

2.2.1 Concept overview

The device consists of a 2 µm wide Z-type resistor actuator without fins, that has the same layout as the devices used to investigate the actuator's performance, but which has one extra suspension/anchoring point at the tip of the cantilever. The cantilever tip and the third anchor are connected via a narrow meniscus (Figure 2.11).
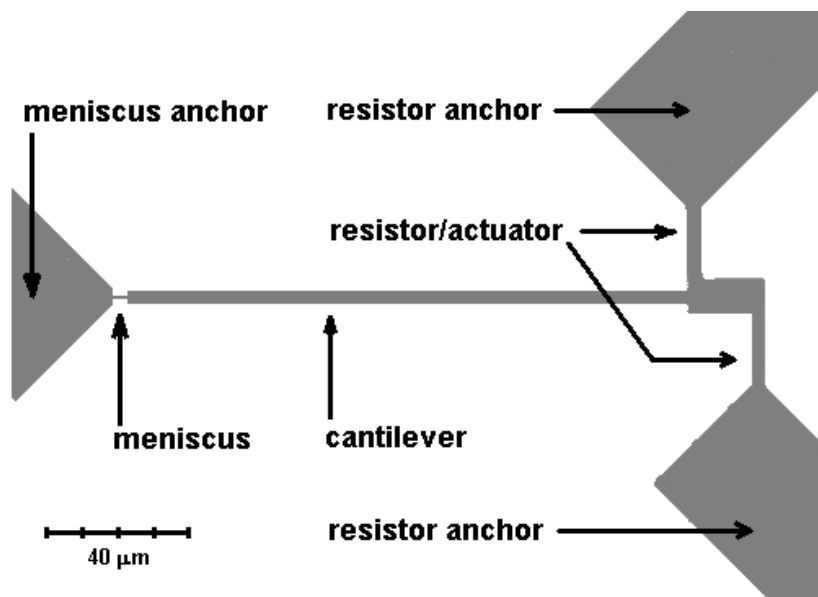
Figure 2.10: Rupture detection concept overview and definitions

When the actuating frequency overlaps with the resonant frequency of the structure, the meniscus breaks, as it is the weakest mechanical point. Therefore, the resonant frequency of the

device can be found without optical inspection – one only has to scan the signal frequency until the current between the cantilever and the meniscus anchor becomes zero.

There are two useful ways to connect the anchors electrically. The input signal can be applied between the resistor anchors and current will flow along the resistors, or it can be applied between the meniscus anchor and the resistor anchors – the current flows along the cantilever and into each resistor.

In the second case, the cantilever also "sees" the signal, but takes little part in the actuation. Due to its length, it cannot cool down much between signal pulses by heat conduction and remains heated up. So the transient temperature of the cantilever is more a function of the average power of the signal, compared to the resistors/actuators whose temperature follows the signal shape more closely. The thermal expansion of the cantilever varies with average signal power, and can be controlled by varying the input signal pulses height.

This expansion results in a compressive stress inside the cantilever and lowers its resonant frequency, i.e. there is a cross-dependence between resonant frequency and power. Mass detection is usually performed by scanning signal frequency to detect resonance. The above dependence allows scanning for resonance at a fixed frequency by varying signal power, which is simpler to implement electronically for most sensor applications.

This concept is better than the state-of-the-art concept [40]. The mass-detection limit is directly related to resonator size. However, there is a limit to how much an electrostaticly actuated cantilever can be scaled down, while still being able to actuate the resonator and detect capacitive changes. At small sizes, detection is only possible with on-chip electronics. This also creates problems with CMOS integration, as e-beam writing on a chip with existing CMOS would lower the yield due to back-scattering of electrons and high electromagnetic fields – both can destroy semiconductor devices and CMOS.

In the proposed concept, actuation and detection are separated. Dynamic electro-thermal actuation is improved as size is reduced, while the detection of a rupture depends only on the ability to detect the current that preceded it, in order to distinguish between the two. Current detection is considerably easier to perform and does not require on-chip electronics, and the currents involved would remain high down to the existing fabrication limits and beyond.

The proposed devices can be used only once, but the same holds for the state-of-the-art device when used as a gas detection sensor [40]; once a cantilever is functionalized with a coating that can selectively bind to certain gas molecules (to be detected), it can not be removed after detection, at least in the field.

2.2.2 Parametric investigation

Devices were fabricated using a 2.5 μm thick LPCVD polysilicon layer on top of a 2 μm thick oxide layer on a Si substrate. The structures were defined by dry plasma etching of the polysilicon layer and subsequently the oxide was under-etched in HF to release the cantilever and the resistors/actuators.

The poly layer was implanted with boron (10^{17} dose), in order to lower the resistivity of the device as much as possible. This was done in order to reduce the signal voltages (required to reach the maximum signal power achievable with the device) to within the limits of the available equipment.

Wet release of suspended structures lowers considerably the yield in the case of cantilevers clamped at one end. The tips are usually pulled to the surface of the substrate during the drying process, and they adhere to it after the drying has been completed. Bridge-cantilever structures like the proposed device, do not suffer from this effect.

The most important part in the device is the meniscus, as it has to be much weaker mechanically compared to the rest of the cantilever, and it has to be weak enough to break at resonance. This requires a cross-section line-width which is an order of magnitude lower than that of the rest of the device. The choice of 2 μm overall line-width precludes the use of conventional lithography to achieve what is required for the meniscus fabrication.

To solve this, the mask design did not include the meniscus – a 1 μm gap was left between the anchor and the cantilever (tip). Photoresist exposure times were incremented from 6 to 8 seconds in successive batches. An increase in exposure time increased the mask linewidth in the final resist pattern and decreased the gap separation until the cantilever tip and electrode resist pattern were connected by the required meniscus (Figure 2.11).
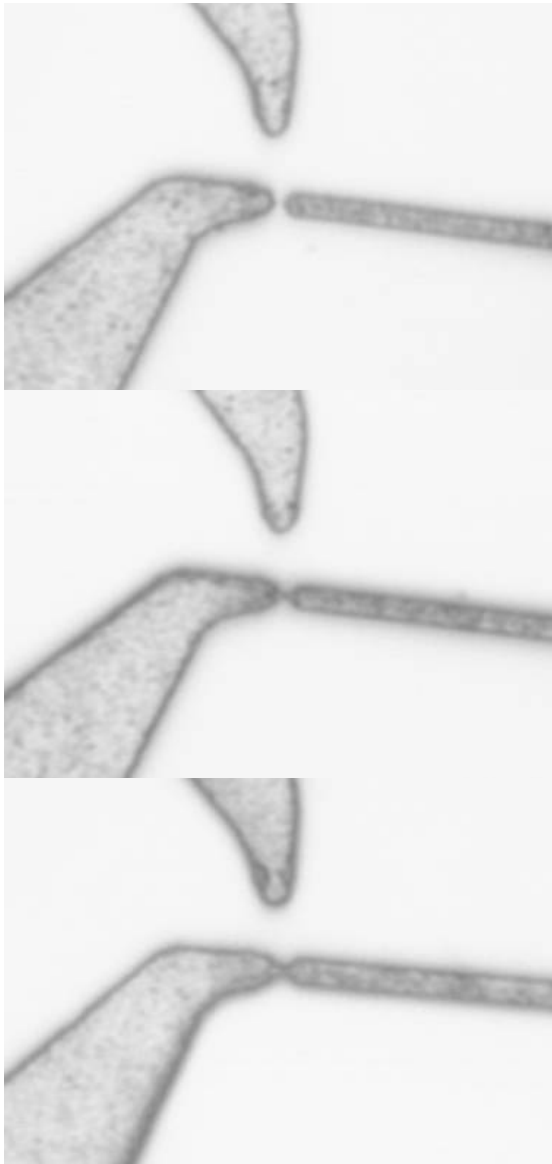
Figure 2.11: Meniscus connection at 9, 11 and 13 sec exposure times

However, the yield of this method is very low. In some batches the same results were obtained between 9-11-13 sec. exposures as in the 6-7-8 sec. batches. There is also a big variation between devices on the same wafer, which is probably due to small variations in the mask itself. We suspect that development of the resist plays a major role in achieving the right tip-anchor connection. The "7 sec" structures are the most rare of all while at the same time being the most useful. We suspect that they are not a function of exposure timing only, but also of using developer into which more wafers have been developed previously, i.e. a "dirty" developer solution might be best. This, however, is a speculative conclusion, given our very low yields.

2.2.3 Experimentation

The resistance between the resistors anchors was measured to be 1.6 kΩ in different devices. The resistance between the meniscus anchor and one of the resistors anchors was 4.4 kΩ. Those values include parasitic resistances such as those between the device bonding pads and the device anchors, as well as the bonding contact resistance.

There were no devices that could achieve a meniscus rupture if actuated by applying the input signal between the resistors anchors, although resonance was clearly visible (the center section of the cantilever is blurred).

When the signal was applied between the

meniscus anchor and the resistor anchors, only the "7 sec" devices could be clearly seen to rupture at resonance. This was done by scanning the input frequency. If, at the chosen power level, the resonant frequency happens to be 180 kHz and the input frequency is scanned from 120 kHz upwards - the center section of the cantilever would start getting more and more blurred from 175 kHz upwards, and the meniscus would break between 178 and 180 kHz (Figure 2.12).
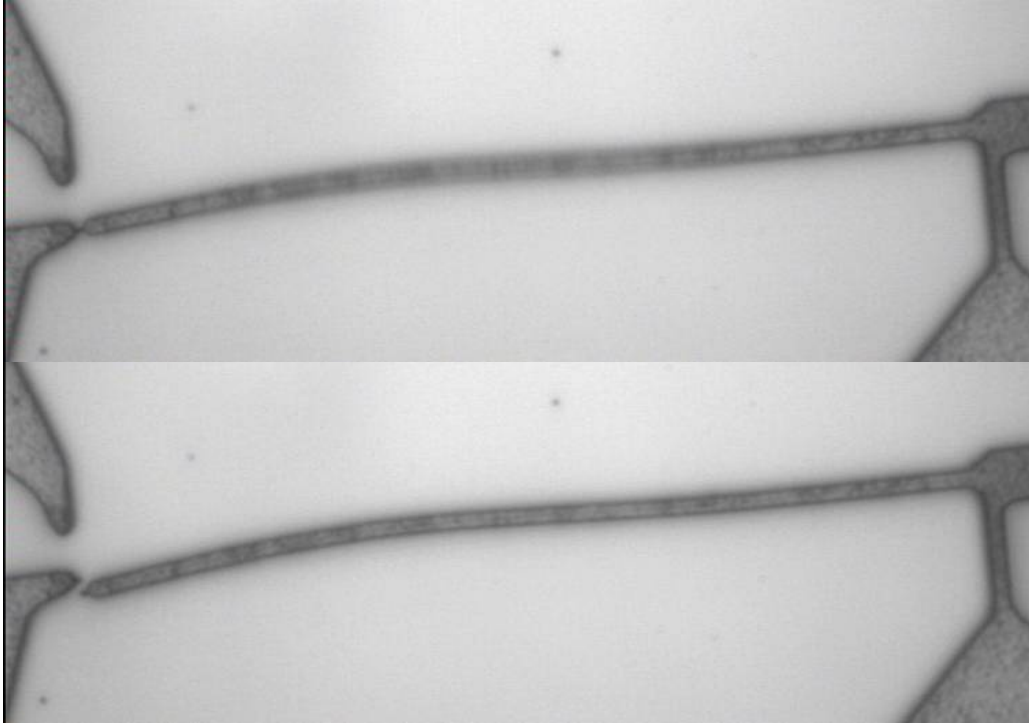
Figure 2.12: Resonant rupture

Dynamic electro-thermal actuation performance has an inverse relation to signal frequency, and direct relation to signal power. The procedure was to increase signal power at steps, and scan signal frequency upwards at each step in order to find the resonant frequency at that power setting step (Figure 2.13).
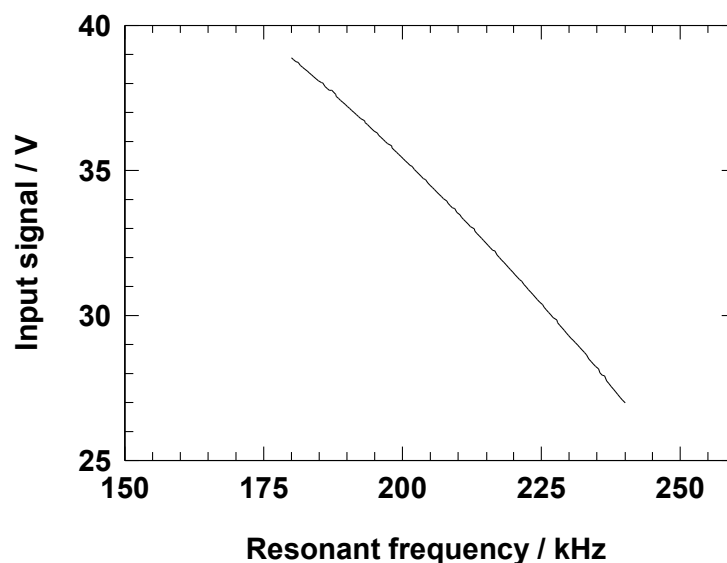
Figure 2.13: Resonant frequency of devices (prior to rupture)
as a function of input signal voltage levels.

The resonant amplitude was too small to be observed below 27V zero-to-peak pulses input signal. At higher signal powers the resonance point was observable, but there was no rupture. Above 38V zero-to-peak pulses input signal the resonant amplitude was large enough to rupture a device, while scanning the input frequency upwards.

In the case of the "8 sec" devices such a rupture would not occur at all, to the limit of the current densities that can be put through the device – above 50V zero-to-peak signal the cantilever center section glows white, and devices break due to too much compressive stress.

Some "8 sec" devices "ruptured" after operation, when power was switched off. This suggested that they had ruptured during operation, but as their meniscus cross-sectional area is bigger, and the meniscus shorter, compared to "7 sec" devices, the cantilevers remain compressed against the anchor even after rupture, maintaining contact. Only after power is switched off and the cantilever cools down, does its (newly acquired) tip slide/move to the side of the anchor, allowing it to be observed/measured.

2.2.4 Applications and summary

To detect mass adsorbing on the cantilever, the input signal frequency can be adjusted at a level slightly lower than a known average resonant frequency for such devices at the chosen signal power. Sufficient adsorbed mass will lower the resonant frequency of the cantilever, making it coincide with the signal frequency, breaking the device and signaling the adsorption event. This would require a "cold" cantilever, i.e. it can only work with a device that ruptures when signal is applied between the resistor anchors.

An alternative is desorption of pre-adsorbed mass on the cantilever surface. Operating at higher signal voltages will heat up the cantilever evaporating a volatile coating. Here an input signal frequency higher than a known resonant frequency will result in a break, only when combined with the presence of such a layer. This approach will work best when the input signal is applied between the meniscus anchor and the resistor anchors.

Both method require prior knowledge of the rupture frequency of the cantilever.

In the case where the input signal is applied between the resistor anchors, this can be achieved by optical/laser detection means after fabrication, for each individual device; the resonant frequency would not vary with power and lower power settings can be used to detect it optically without this leading to a rupture.

A more general approach is to aim for high device uniformity, and then "break-test" all devices after fabrication in a wide frequency range, but with a very narrow window where the rupture frequency is most likely to be. This would rupture all devices that would otherwise rupture outside the narrow frequency range window, and eliminate them. The higher the device uniformity, the narrower that window can be, while preserving a high yield. The narrower the window, the better the maximum mass resolution; this window is essentially the error in the mass measurement.

For that reason, the aim of future research in the area is to achieve the highest uniformity possible, and this is best done by electron beam lithography writing of the whole device including the meniscus. E-beam use would also allow to scale down the devices to, and beyond, the size of the state-of-the-art devices. The statistical distribution of rupture frequencies can then be explored in order to determine the mass sensitivity limits.

2.3 Optical detection

Optical detection and characterization of the dynamically actuated electro-thermal cantilever devices (Figure 2.8) was investigated by Morten Fugl, using a setup built for the purpose by Prof. Winnie Svendsen and Rasmus Sandberg [22].

Our research has focused on developing and optimizing a measurement procedure to obtain the highest possible mass resolution for such a sensor, and experimentally testing the mass sensitivity of the sensor by performing mass measurements on latex beads and gas phase attached mass using argon and nitrogen.

2.3.1 Concept overview
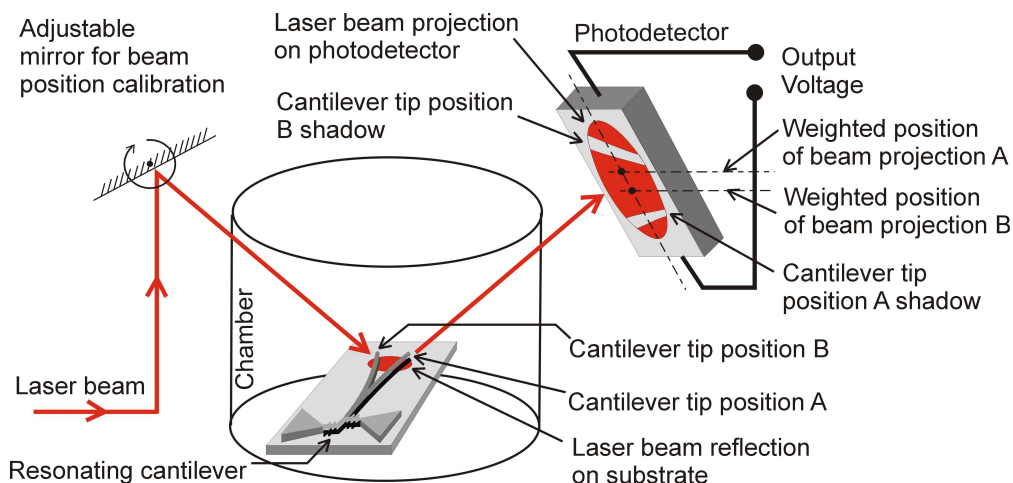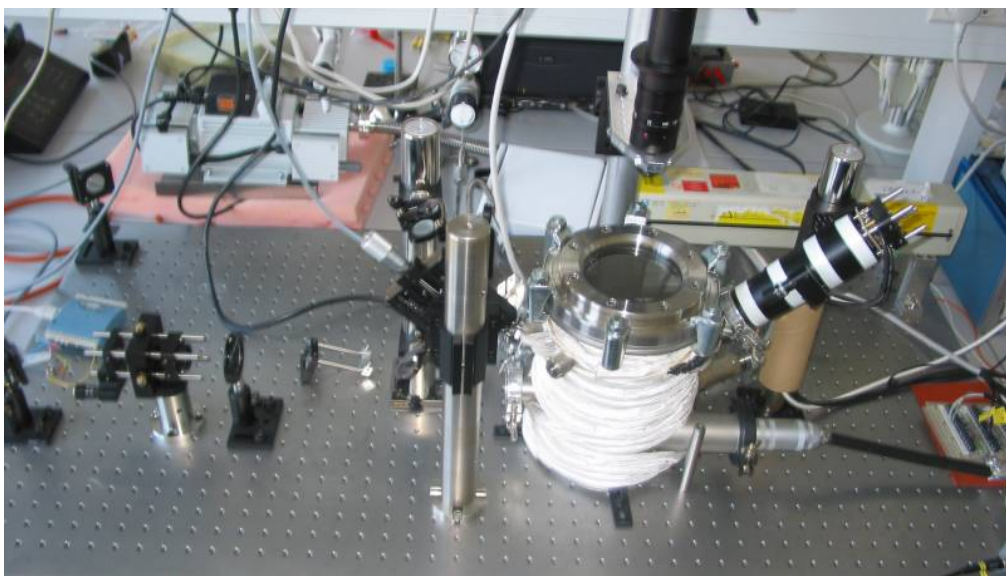
Figure 2.14: Experimental setup front view and schematic drawing

Figure 2.14 shows the laser and chamber setup. The chamber is located in the center of the setup. It has means of changing temperature, reducing pressure and control of a gas mixture inside it. A laser beam enters from the left side and is subsequently reflected off the device. It exits out of the right side of the chamber where a photo sensor measures the weighted position of the beam

reflection. The setup has lenses and a diaphragm which control the beam size and intensity. Before the beam enters the chamber, it is reflected on a mirror which has fine controls for its direction. One can then calibrate the beam and position the laser spot on a particular spot on the device under test, using a microscope camera above the setup.

The laser beam is not deflected by the cantilever curvature, which is most commonly used to optically detect cantilever movement. The device surface is grainy and non-reflective. The silicon substrate beneath is flat and reflective. The laser beam which is approximately 20 µm wide, is reflected at the silicon base beneath the cantilever towards the detector, thus projecting a shadow of the cantilever onto the detector. The photo sensor output transduces the weighted position of the beam into a voltage signal and this weighted position changes as the shadow of the cantilever device moves across the beam. So, the photo sensor output is a sinusoidal signal at the frequency of the cantilever movement, which allows detection of amplitude and phase with respect to the driving frequency.

A gain-phase analyser (HP 4194A) and a operational amplifier driven into saturation were used to create the square wave input signal and to detect the output voltage of the photo sensor. The gain-phase analyser scans a chosen frequency range and draws phase and amplitude curves for. It also calculates the phase difference between the square wave input signal created and the measured signal. From this, graphs like Figure 2.15 are produced, transducing mechanical amplitude and phase to voltage.
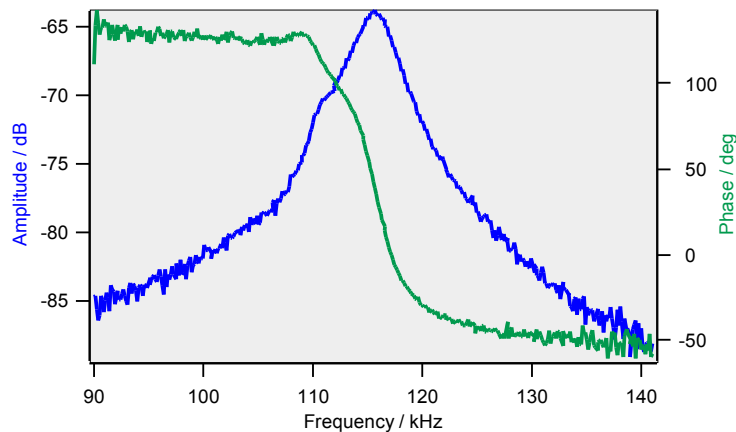
Figure 2.15: An overview sample sweep from the gain phase analyzer.

2.3.2 Parametric investigation

Figure 2.16 shows sample variations over frequency range and sampling duration. The higher the sampling duration, the less the noise, for large sweep ranges (top row). The reverse holds for narrow sweep ranges (bottom row). Here low frequency noise is introduced with the 120s sampling duration. This is due to fluctuations in amplitude over time; the gain-phase analyser measures every individual point over a longer period of time, rather than averaging many fast sweeps. The bottom row also shows, that the phase plot is much less noisy than the amplitude plot. Two frequency span ranges has been chosen for further investigation: 16kHz and 6kHz. Three sampling durations were chosen, 1s, 6s and 120s.

Rather than just finding the maximum amplitude point and using its frequency as the resonance frequency, it is much better to fit a uniform function to the curve and finding the resonance point this way. When doing this, all the curve points contribute to the function and much of the noise is eliminated.

There are three different sampling times and two frequency ranges, which makes a total of 6 combinations. For each combination, 20 sweeps are recorded and each sweep fitted with a certain type of function. From this its resonance frequency is determined. The uncertainty of the resonance frequency is calculated using [41]

$$u(f_{res}) = \sqrt{\frac{\sum_{j=1}^{20}(f_{res_j} - \bar{f}_{res})^2}{20-1}} \cdot 1.03 \tag{2.5}$$
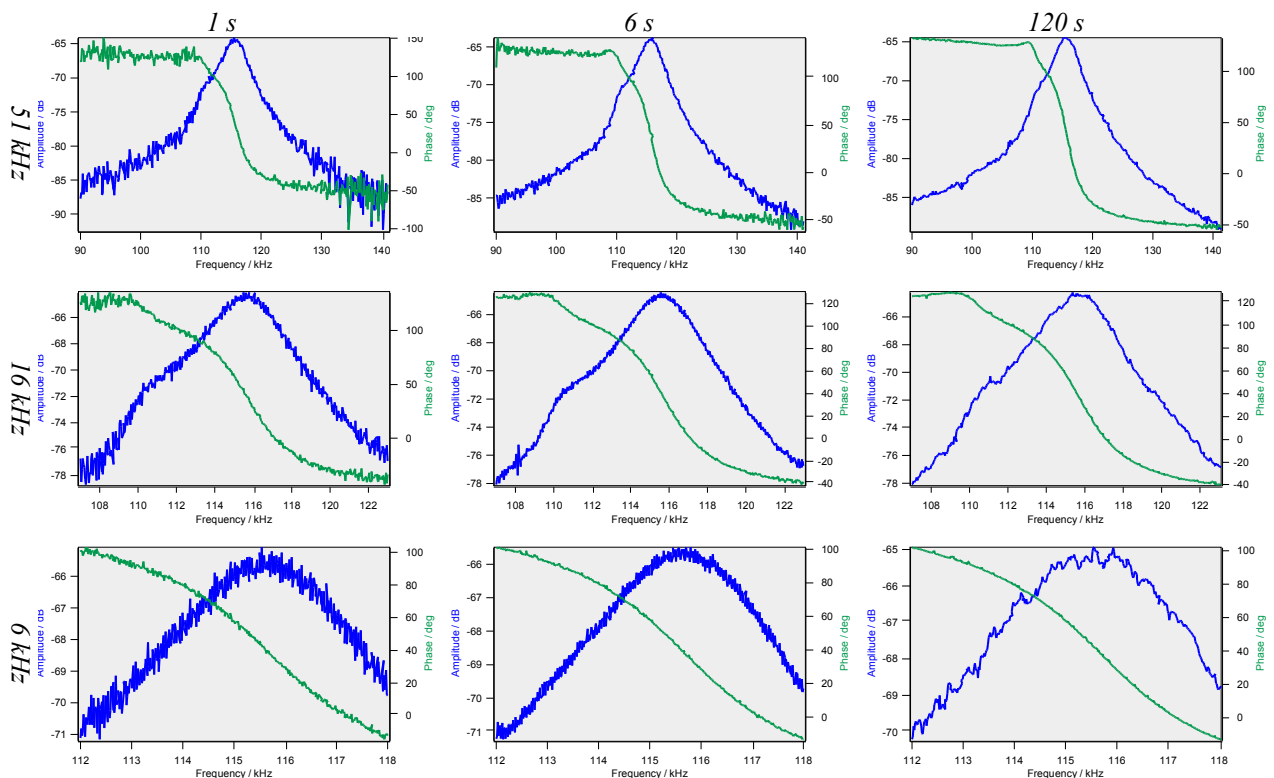
Figure 2.16: Sample sweeps. Horizontally three sampling durations. Vertically three frequency ranges.

This value is the uncertainty when doing one measurement. The processing was software automated (Appendix B).

Table 2.1, shows the different fitting-functions that have been examined. "Raw" means raw data, which is included to show the benefit of curve-fitting. "Smoothed" means raw data that has been digitally filtered to some degree, removing higher frequencies (noise). The rest are real functions. Figure 2.17 and Figure 2.18 map directly to Table 2.1, showing the fitting-functions together with raw data. Gaussian peak (amplitude) and sigmoid (phase) are on the same graphs.

Measurements were done at 23.9 °C, pressure 100670 Pa and input voltage of 12.0 V zero-to-peak.

	1 s 6 kHz	6 s 6 kHz	120 s 6 kHz	1 s 16 kHz	6 s 16 kHz	120 s 16 kHz
Amplitude:						
Raw	176.7	203.7	227.5	164.5	185.0	249.2
Smoothed (100)	97.0	170.2	203.2	50.5	63.1	152.7
Polynomial 3 deg.	31.0	47.7	48.7	31.2	35.9	35.3
Polynomial 5 deg.	40.7	56.2	74.0	30.3	43.9	40.8
Polynomial 8 deg.	40.1	56.8	73.5	42.6	56.4	72.2
Polynomial 15 deg.	37.9	54.3	83.9	27.5	53.3	87.4
Gaussian peak	30.2	48.0	52.0	33.1	44.1	35.7
Phase:						
Raw	20.9	9.1	5.8	25.4	6.3	4.8
Smoothed (200)	7.9	4.9	5.9	5.3	3.7	4.4
Polynomial 3 deg.	8.0	5.3	7.0	11.1	7.6	9.6
Polynomial 5 deg.	7.0	4.7	5.9	9.4	5.0	6.5
Polynomial 8 deg.	7.0	4.7	5.9	8.4	4.1	5.7
Polynomial 15 deg.	7.6	4.6	5.7	7.5	3.9	5.8
Sigmoid	6.8	4.7	5.7	7.8	4.3	5.7

Table 2.1: Uncertainties for the resonance frequency (Hz) using different means of graph fitting (left column) and different sample durations and frequency ranges (top row).
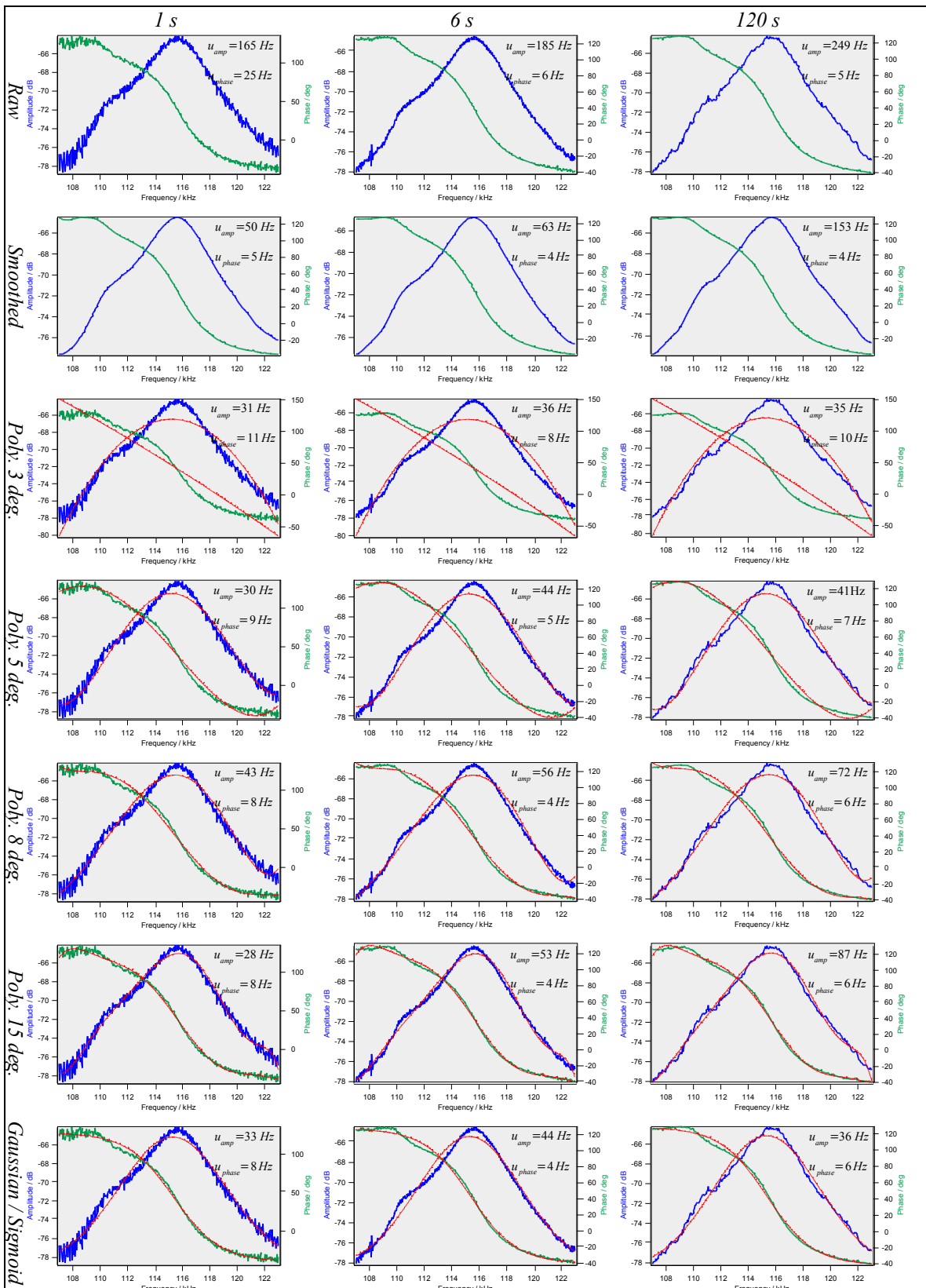
Figure 2.17: These graphs have a 16kHz scan range and correspond to the three right columns of Table 2.1, with amplitude and phase on the same graph, along with their fitting-function plots. The uncertainty for a measurement is printed on each graph, for both amplitude and phase method.
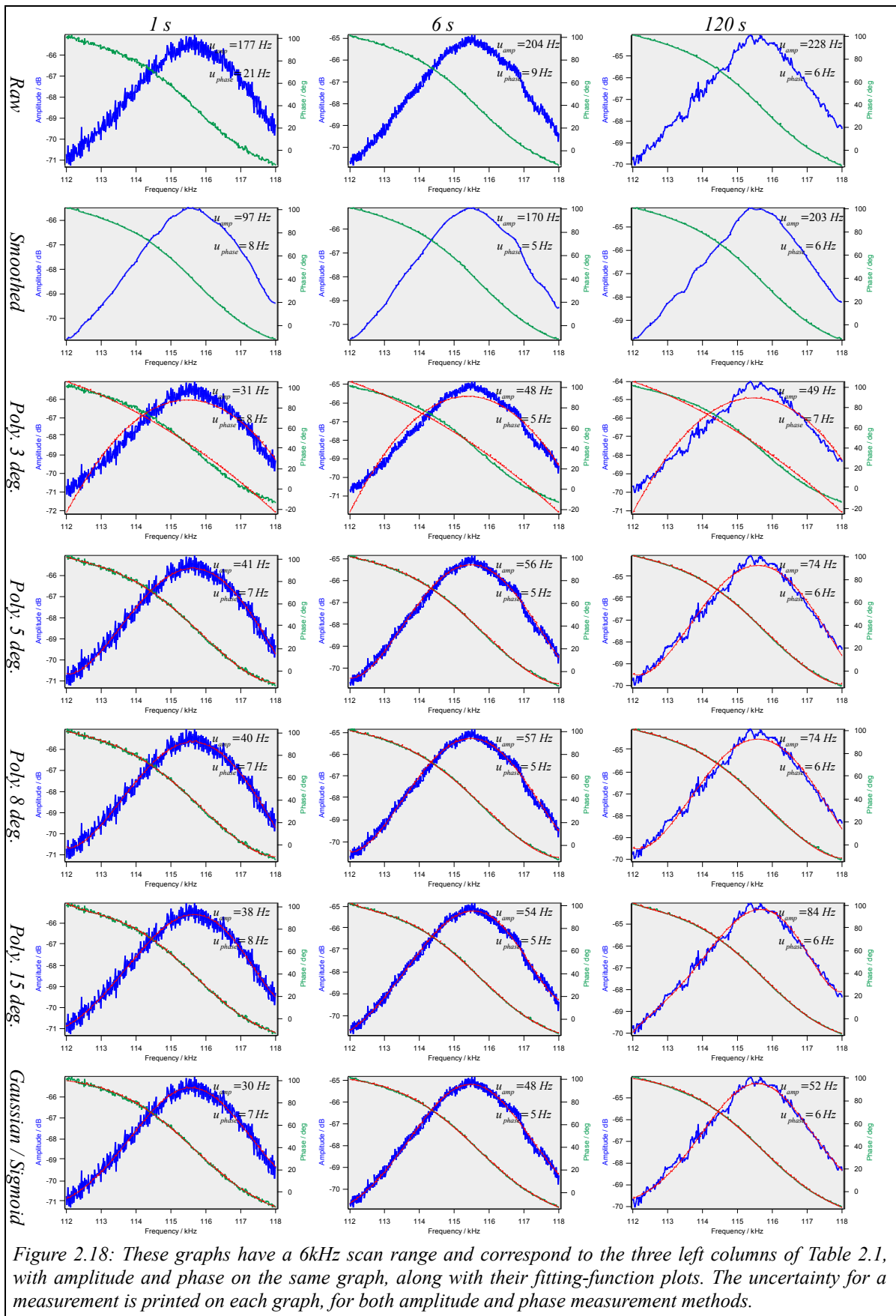
Figure 2.18: These graphs have a 6kHz scan range and correspond to the three left columns of Table 2.1, with amplitude and phase on the same graph, along with their fitting-function plots. The uncertainty for a measurement is printed on each graph, for both amplitude and phase measurement methods.

Conclusions about the amplitude fitting methods of Table 2.1:

- Raw: Using raw data is by far the least precise method. The error range is [164; 249] Hz. High frequency noise dominates the lower sampling times. Error increases with sampling time, which means that the low frequency noise has larger amplitude than the higher frequencies.

- Smoothed: This is the second worst method. The error range is [50; 203] Hz. The error is lower for the 1s sampling time, because the higher frequencies are filtered out. Again error increases with sampling time, because the lower frequencies remain.

- Polynomials: Errors are diminished further by a large amount, with an error range of [28; 83] Hz. Generally, the errors does not change much for the lower polynomial degrees. For the higher degrees, again the error increases with sampling time. For the 120s sampling time, the error increases with polynomial degree. This is due to the higher polynomial degree, the more resemblance to the raw data and therefore low frequency noise dominates. For 1s and 6s, error does not vary much with polynomial degree.

- Gaussian peak: An error range of [30; 52] Hz. It resembles the polynomials in precision. It is fairly invariant to sampling time and frequency range.

Generally, the error difference between two frequency ranges is insignificant. The polynomials and the Gaussian peak have the best accuracy. The smallest error is 28 Hz for a polynomial of 15. degree, 1s, 16kHz sweep. Several other combinations have similar accuracy though. Considering that the amplitude peak is about 16kHz wide, a 28Hz is error very low, a factor of 1:500.

Conclusions about the phase methods of Table 2.1:

- Raw: The error range is [5; 21]. Again the raw data is the least precise way of measuring, but this is only true for fast sweeps. With 120s, the precision is among the best in the table. This means that higher frequency noise is filtered out and that apparently low frequency noise is not present, as with the amplitude fitting results.

- Smoothed: The error range is [4; 8]. The variations are quite low. The 6s sweeps have a little better accuracy than the others.

- Polynomials: The error range is [4; 11]. The functions are similar to the smoothed functions. The lower polynomial degrees have slightly higher errors.

- Sigmoid: The error range is [4; 8]. It behaves much like the higher polynomial degrees.

Generally the error difference between two frequency ranges is insignificant, as with the amplitude fitting results. The best accuracy of 4Hz appears in a couple of places in Table 2.1, e.g. a smoothed 6s, 16kHz measurement. A peak width of 16kHz and 4Hz error is very good result, a factor of 1:4000.

Clearly, using the phase curve gives the best precision. The 4Hz can be translated into a minimal mass change that we should be able to detect. The volume of the cantilever device is 160x2x2.5 μm^3 , and the density is ρ=2330 kg/m³. Using (1.6) with $f_0 = 116\,kHz$ and $\Delta f = -3.7 \text{Hz}$, the minimum detectable mass becomes

$$\Delta m \approx \frac{-2\,\Delta f\,m_0}{f_0} = \frac{-2\,\Delta f\,l\,w\,h\,\rho}{f_0} = 7.2 \cdot 10^{10}\,u = 120\,fg$$

The sensitivity of the cantilever with respect to mass change per frequency change becomes

$$\left|\Delta m / \Delta f\right| = -1.9 \cdot 10^{10}\,u/Hz = 32\,fg/Hz$$

A way of lowering the uncertainty is to do many subsequent measurements in a row. A mean value of the resonant frequency can be calculated from this. The uncertainty after n repetitions is [41]

$$u(\bar{f}_{res}) = \frac{u(f_{res_i})}{\sqrt{n}} \tag{2.6}$$

Though a 6s scanning is a little more accurate than a 1s one, repeating a 1s scan six times, lowers the uncertainty to 41% compared to the uncertainty for a single 1s scan. Sixty 1s scans lower the uncertainty to 13%, which gives a mass sensitivity of

$$\Delta m \approx 22\,fg$$

So in conclusion, it can be seen that better sensitivity is possible, when measurement speed is sacrificed. Performing many short time interval scans gives better mass resolution compared to one long scan of equal total time length.

2.3.3 Experimentation

Characterization, input signal power

Figure 2.19 shows the graph series for input voltage changes. Measurements were done at 27.3 °C and 97360 Pa. With increasing voltage, the base amplitude level and the base phase level increase too. Since the base phase level changes vertically, the current phase method can not be used to determine the resonance frequency shift. In the last three graphs the amplitude peak starts to bend down, having a reverse resonance effect (anti-amplitude resonance). We believe this is a by-product of large resonant amplitudes; the shadow of the cantilever moves across and outside the laser beam.

The resonance frequency changes in a decreasing linear manner with voltage, Figure 2.20. It may be approximated with the equation

$$f_{res}(U_f) = -56.3\,\frac{Hz}{V} \cdot U_f + 116340\,Hz$$

Which means that the resonance frequency decreases with 56 Hz when increasing the input voltage by 1V.

This effect could possibly be due to temperature; the temperature of actuator, cantilever and their immediate environment increases with increasing input power.

The results suggest that the optimal input voltage signal is between 10V and 13V zero-to-peak,

as this setting gives the lowest noise.

Figure 2.19: Graphs for voltage changes (starting top left, going down, increasing the voltage). Axis have fixed ranges.
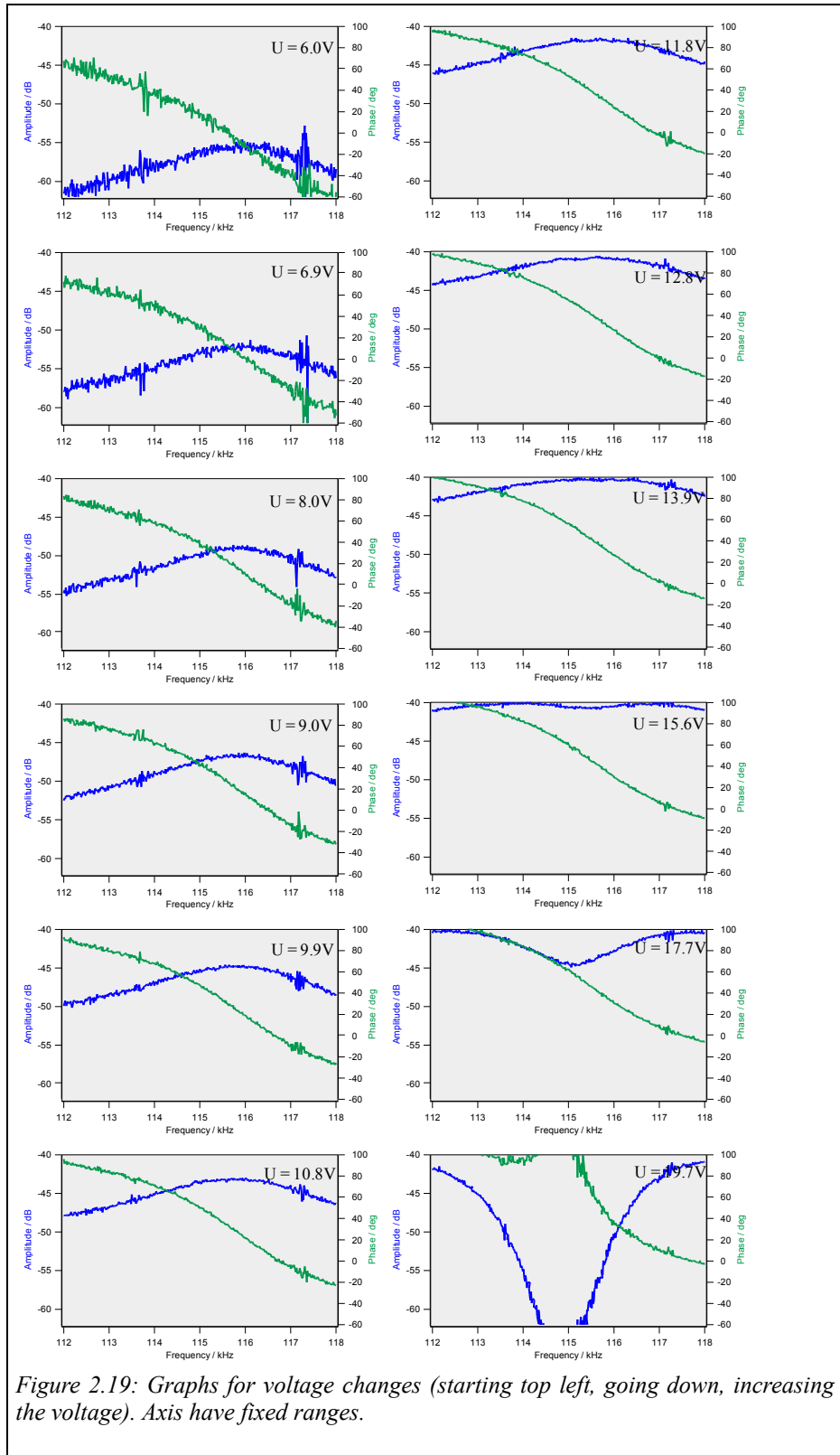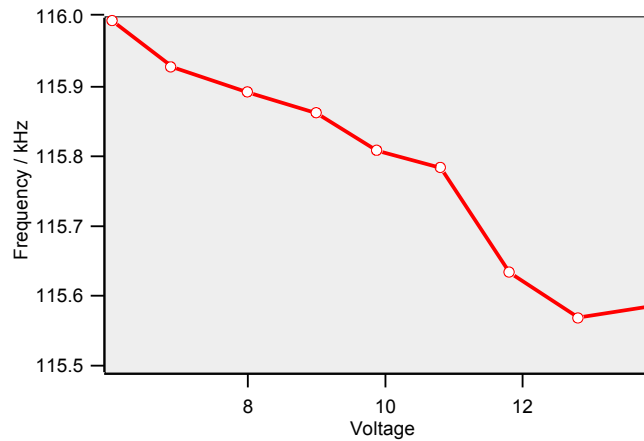
Figure 2.20: Resonant frequency vs. voltage, using the amplitude measurement method.

Characterization, temperature

Environmental temperature characterization was done by raising the temperature in the chamber to about 80 °C and measurements were taken as it slowly cooled down. During the cooling process, it was necessary to calibrate the laser beam spot several times in order to get a good curve. Measurements become more unreliable with higher temperatures.

Figure 2.21 plots the resonance frequency vs. temperature. To test the reliability, the measurements were done twice, therefore two graph pairs. The amplitude method fails to produce reliable graphs, which is caused by the very noisy amplitude readings. The phase does not change so much and its graph is more reliable. It is seen clearly where the laser spot position was calibrated, the graph changes suddenly a lot. Apart from these sudden changes, the graph is quite smooth, but it is difficult to estimate a fair equation. Ignoring the parts of the plot where there are large sudden variations in resonant frequency, it can be said that the resonant frequency increases with temperature. Further conclusions can not be drawn, given the large experimental uncertainties. A source of the noise could be turbulence in the chamber, and subsequent small scale pressure fluctuations caused by the high temperature.

This result, however, seems to confirm the speculation that input signal power affects the resonant frequency through a temperature dependence.
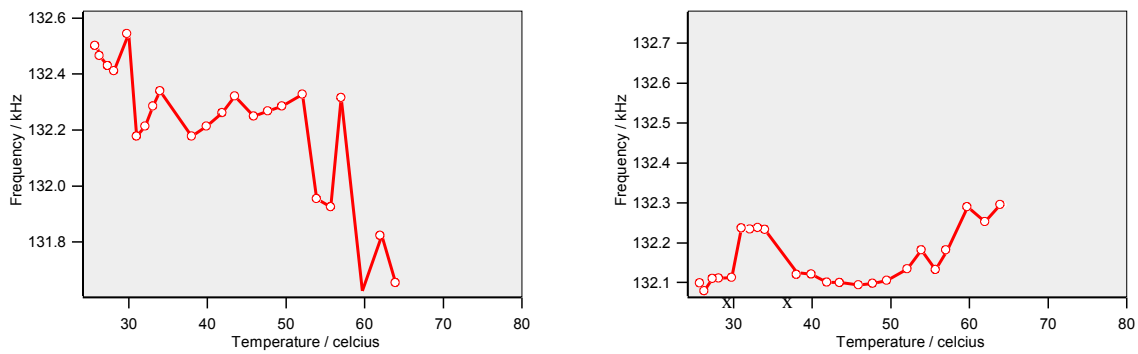
Figure 2.21: Resonant frequency vs. temperature. Left, using the amplitude measurement method. Right, using the phase measurement method. Re-calibration points are marked by x.

Characterization, pressure changes

Figure 2.22 shows sample plots from the measurements used to characterize the dependence of resonant frequency to pressure. Measurements were done at 27.4 °C and 8V input signal voltage; The operating voltage was lowered from the optimal 10-13V to 8 V to prevent the overheating the actuator at very low pressures. Measurement plots were similar to the voltage characterization plots with respect to the bending down of the amplitude peak (anti-amplitude resonance). Another observed feature is that the amplitude curve gets slightly narrower with decreasing pressure due to the decreasing dampening; the quality factor Q increases with decreasing pressure. Figure 2.23 shows the resonance frequency versus pressure dependence, using both the amplitude and phase methods. Both show similar linear behavior and as expected with the phase method being the most precise. It may be approximated with the equation

$$f_{res}(P) = -1.28\frac{Hz}{kPa} \cdot P + 115970 \text{Hz}$$

Which means that the resonance frequency decreases by 1.28 Hz when increasing the pressure by 1 kPa.

This result is in agreement with the general theory for resonant cantilever devices operating in a fluid medium (1.8). Lowering the environmental pressure lowers the medium density which results in lower attached mass and higher resonant frequency.

However, lowering medium pressures also leads to less convective cooling for the cantilever device, and higher overall operating temperatures.

Further experiments were performed with argon and nitrogen to separate those two possible effects and perform a true mass measurement.

Figure 2.22: Graphs for pressure changes (starting top left, going down with decreasing pressure).
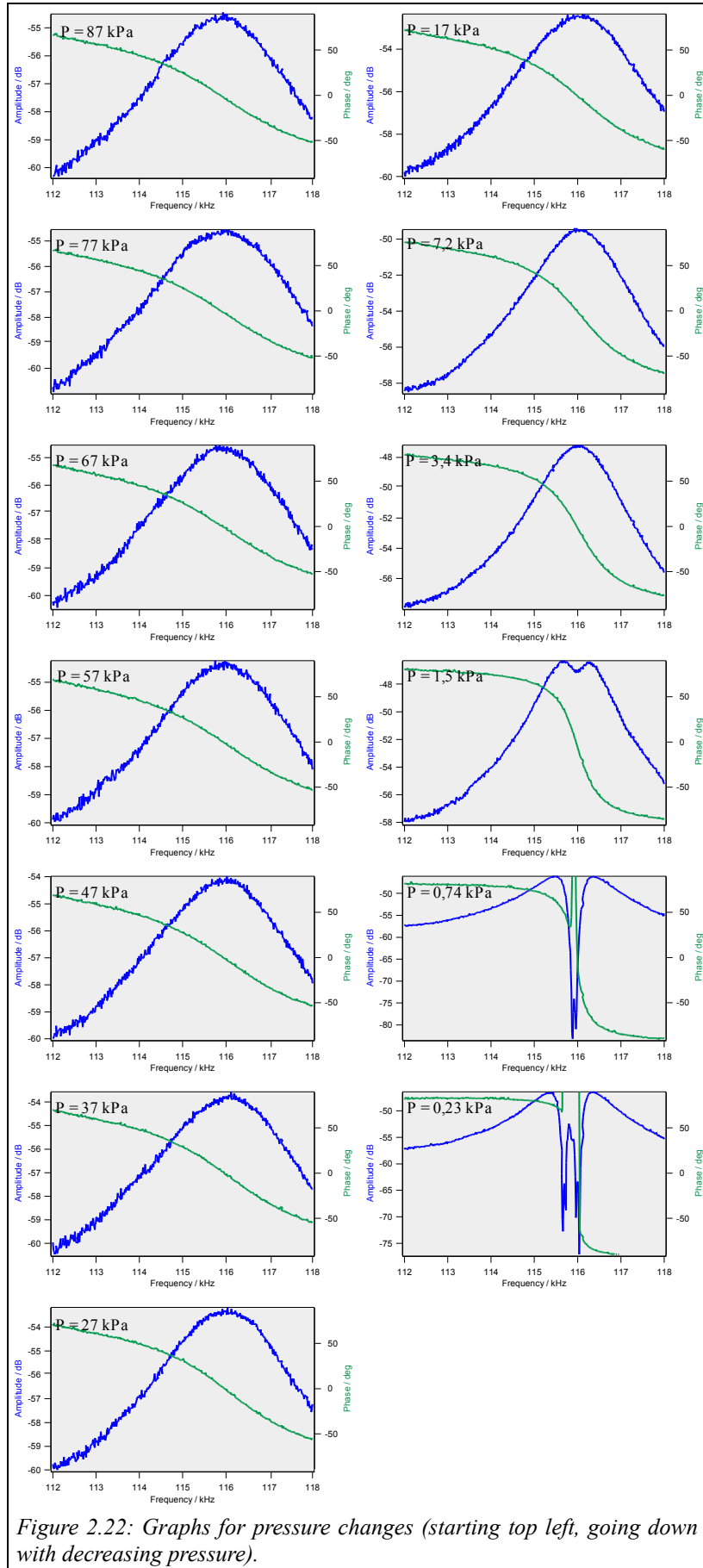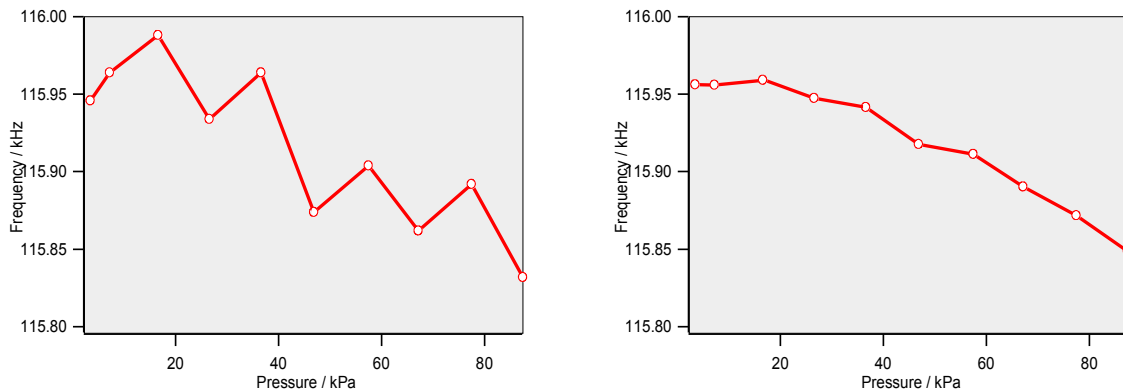
Figure 2.23: Resonant frequency vs. pressure. Left, using the amplitude measurement method. Right, using the phase measurement method.

Mass measurements, latex beads

We performed two real mass measurement experiments, in order to empirically determine the mass sensitivity of the cantilever sensor.

The devices' mass sensitivity was characterized using latex beads approx. 2-3 μm in diameter, placed on the cantilever tip.
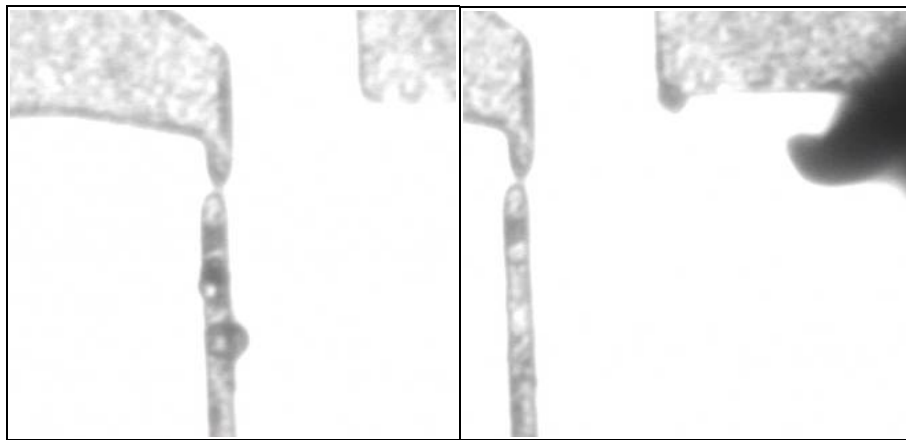

Figure 2.24: #1 cantilever with and without two beads. The needle probe used for deposition can be seen.

A small drop of latex beads in a water suspension were spotted on a silicon substrate using a syringe. A drop of glycerin was placed on top of the beads after the water had evaporated. As the glycerin evaporated, small glycerin covered clusters of latex beads were left outside the edges the evaporating glycerin drop. Individual beads were then picked up from those clusters using a probe-station micro-manipulator with a tungsten needle probe tip, by lowering the tip towards a bead and then lifting it up, the beads sticking to the probe's underside. The reverse procedure was followed to place a bead on a cantilever tip; the probe tip was lowered towards a cantilever device tip and then lifted up leaving the previously picked bead stuck to the cantilever.
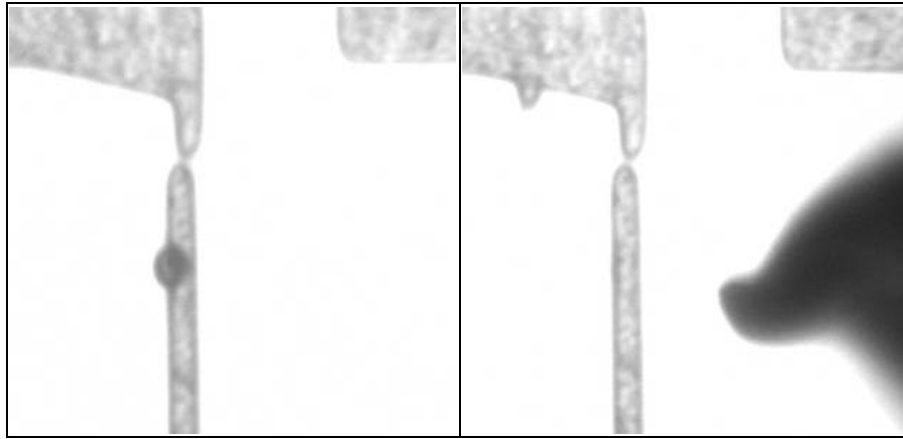
Figure 2.25: #2 cantilever with and without one bead. The needle probe can be seen.

Resonant frequency measurements were performed before and after the beads were placed. Two devices were used; one with two beads, Figure 2.24, and one with one bead, Figure 2.25. The resonance point was measured with and without beads, Table 2.2. The resonance shift due to a mass change, can be compared to the theoretical expected shift using (1.6):

$$\Delta f \approx -\frac{1}{2}\frac{\Delta m\, f_0}{m_0}$$

The results show that the actual frequency shift is better then the expected frequency shift by a factor of 3. The latex beads have the density of water. From this an actual mass sensitivity can be calculated using $\Delta f_{min} = 3.7\, Hz$

$$\Delta m_{min} = \frac{\Delta f_{min}\Delta m}{\Delta f_{res}}$$

	#1 cantilever	#2 cantilever
Number of beads	2	1
Δm total bead mass (fg)	37633	18817
f_{res} measured (no beads) (Hz)	127830	121270
f_{res} measured (with beads) (Hz)	124206	119286
Δf_{res} measured (Hz)	**3624**	**1984**
Δf_{res} theoretical (Hz)	**1290**	**612**
Δm_{min} actual mass sensitivity (fg)	*38*	*35*

Table 2.2: Results from mass measurement experiment using latex beads .

So, the actual mass sensitivity of the cantilever devices is 38fg, given the experimental conditions and procedures that we have set.

Density measurements, gas phase

Resonant frequency of the devices under test was characterized with respect to environmental density using three different gases – argon, air and nitrogen. An increase in density of the medium leads to an increase in 'attached mass', and lowers the resonant frequency (1.8). The measured resonant frequencies follow this rule, in the case of nitrogen/air and argon.

Figure 2.26 shows the resonance frequency of each gas, using scatter plots to show the related uncertainty. Table 2.3 compares the measured and theoretically expected resonant frequency shifts for each gas.

The experiments show one order of magnitude larger resonant shifts than the ones predicted by theory, i.e. device sensitivity to gas dynamic viscosity is unexpectedly good.
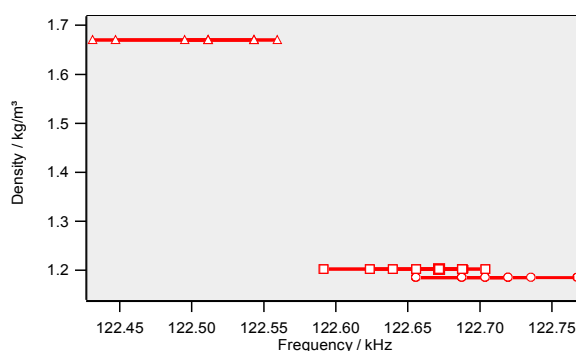

Figure 2.26: Scatter plots of density vs. resonant frequency. Circles are nitrogen, triangles argon and squares air.

	Argon	**Air**	**Nitrogen**
Density $\rho_{fluid} (kg/m^3)$	1.67	1.202	1.185
Viscosity η_{fluid} (Poise)	0.0002099	0.0001695	0.0001657
f_{res} theoretical relative to argon (Hz)	122509	122532	122533
f_{res} measured (Hz)	122509	122662	122703
Δf_{res} theoretical relative to argon (Hz)	0	**23**	**44**
Δf_{res} measured (Hz)	0	**153**	**194**

Table 2.3: Resonant frequencies measured in three different fluids. Using (2), the theoretical value is calculated relative to argon.

2.3.4 Applications and summary

The setup and in-plane cantilever device type have been characterized. The input voltage and

pressure dependencies were determined successfully. Different means of measurements have been tested, e.g. changing scanning duration, frequency scanning interval, type of curve fitting, use of amplitude or phase shift measurements. The phase method was found to be more precise than the amplitude method. Real mass changes were measured successfully and the sensitivity was found to be higher than expected and theoretically predicted for a cantilever sensor device of the given size.

It must be stressed out that optical detection is means to characterize devices, rather than means for detection in the field or for a market product, given our research motivation; it does require non integratable external equipment (laser and optics), a vacuum chamber and and bulky electronics (a Gain-Phase analyzer).

It could, however be used in conjunction with rupture detection devices, to characterize individual devices in a non-destructive way, prior to using them for field detection.

2.4 Contact detection

2.4.1 Concept overview

Contact detection was attempted by fabricating devices with two electrodes next to the tip of the cantilever, so that the tip touches the electrodes at resonance and makes an electrical connection.

2.4.2 Experimentation

Figure .2.27 shows the cantilever device approaching resonance, as the input frequency is being scanned towards the device's resonant frequency.
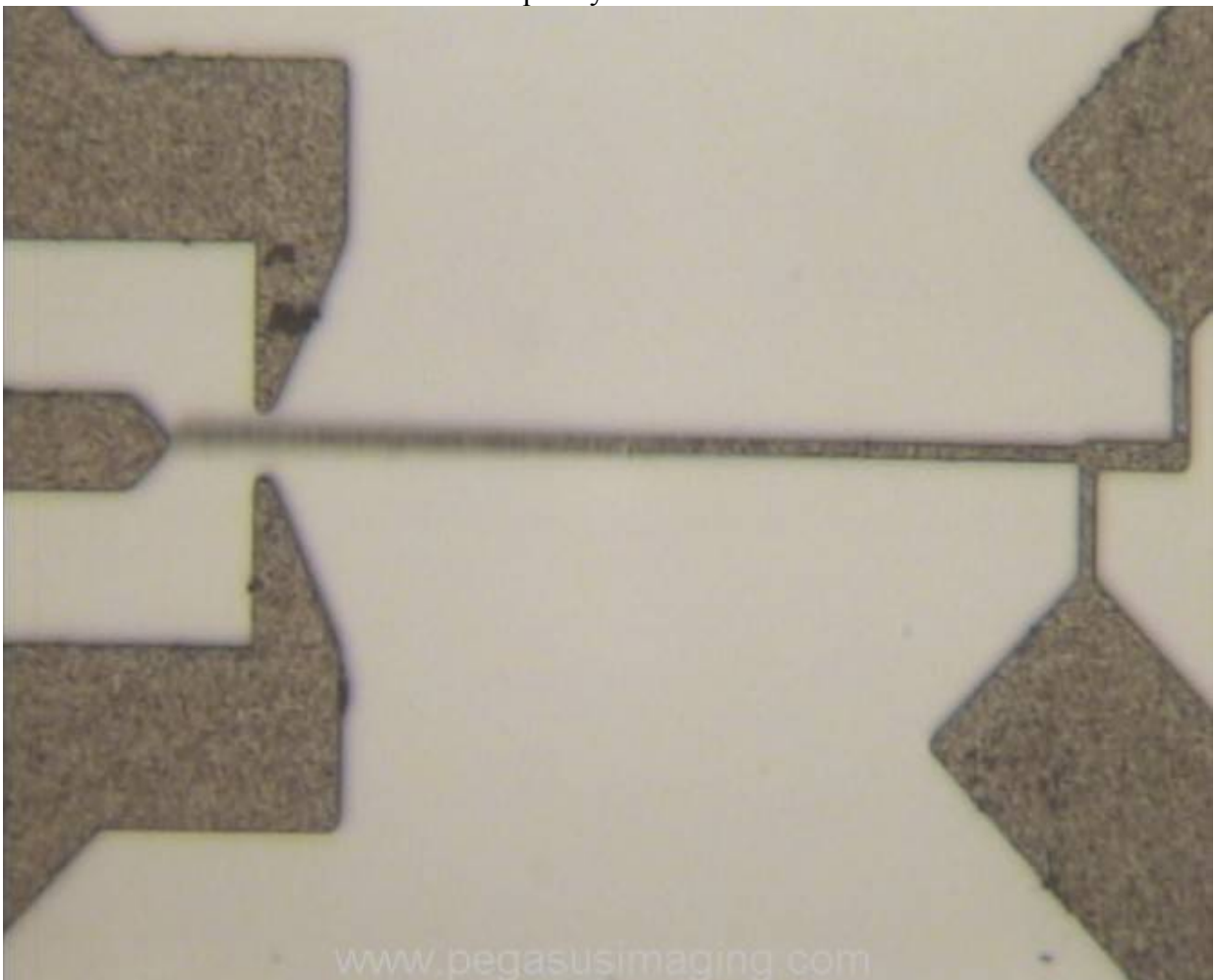

Figure 2.27: Cantilever approaching maximum resonance between two electrodes

When the resonant amplitude increases to the point where it is equal the cantilever-electrode gap distance the tip touches and adheres to the electrode (Figure 2.28).
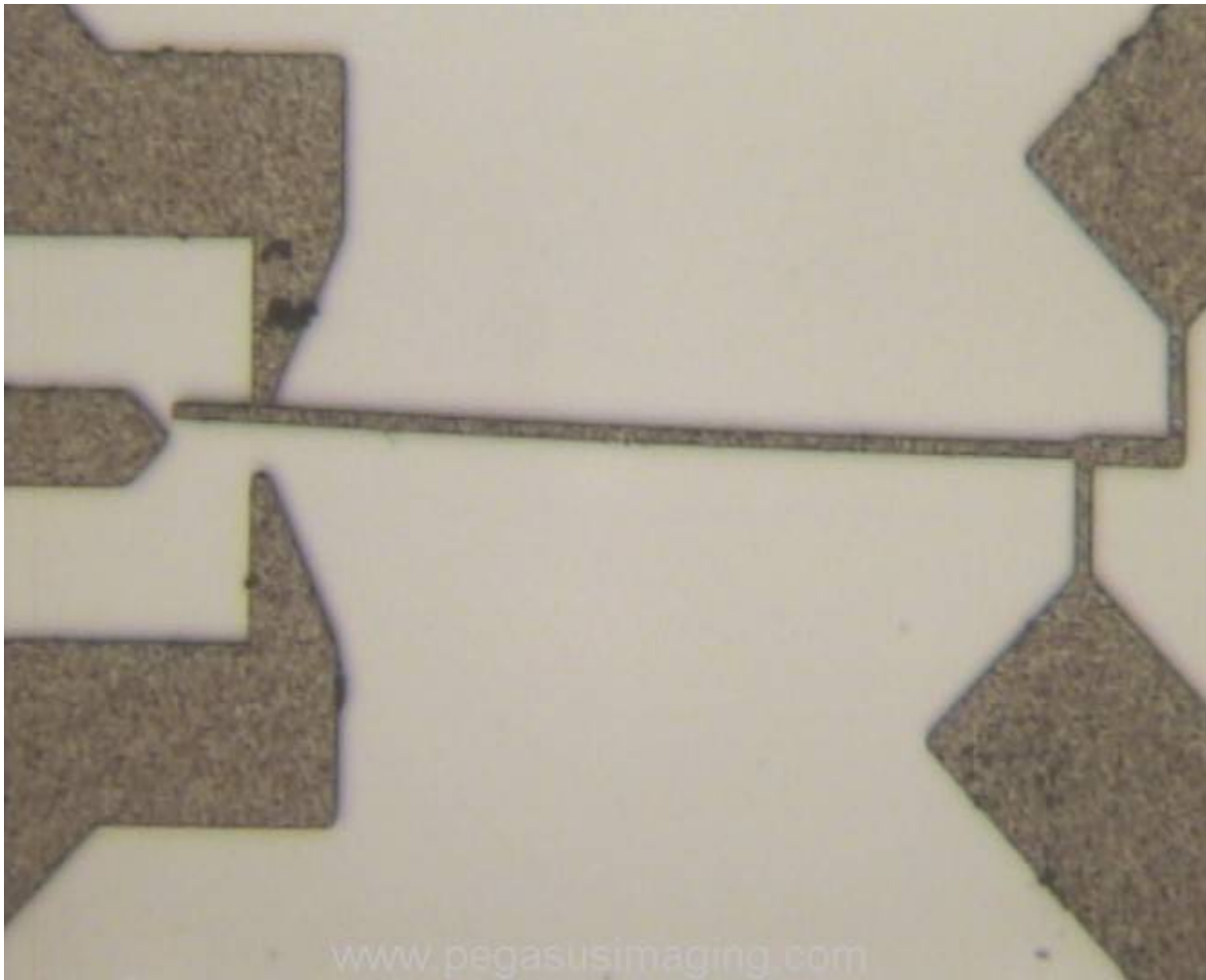
Figure 2.28: Cantilever tip touches and adheres to electrode when resonant amplitude equals the tip-electrode separation gap

Switching-off the input signal at that point was found to result in cantilever tip release; the tip detaches from the electrode at that point.

However, we were unable to measure any current between cantilever and electrode, while the tip is adhering to the electrode, a plain polysilicon cantilever device and electrode is not sufficient for electrical contact to be made.

2.4.3 Applications and summary

A possible reason for the poor electrical conductivity between cantilever tip and electrode could be the presence of native oxide covering the polysilicon device. One way to solve this problem would be to cover the sidewalls of the cantilever and electrode with a material that has a low contact resistance such as gold, or tungsten.

However, we felt that contact detection for resonant cantilevers is not an option that is worth persuing; repeated mechanical contact (at high frequencies/rates) is likely to lead to fast cantilever tip and electrode erosion, which might change the cantilever mass and pose an ultimate limit to such a device mass sensitivity, defeating its purpose.

Chapter 3

General research into resonant devices

3.1 Research approach

Dynamic electro-thermal actuation of a cantilever sensor may work in air, we have failed to observe actuation in a fluid medium or design a feasible detection mechanism for liquid sensing. A plain cantilever device is subject to enormous viscous damping at small scale, and a serious reduction in Q-factor; viscous effects dominate at small scale and pose an insurmountable detection problems. While the theoretical mass detection sensitivity of a cantilevers sensor is improved at lower scales, reducing the scale of devices lowers the sensitivity in a liquid medium. To avoid this contradiction in scaling laws we have decided to investigate resonant structures that are not plain cantilevers and displace as little of their surrounding medium as possible.

To do this, we postulated actuation/detection principles that are feasible, fabricated as many different device concepts as possible using those postulated principles, and tested all for resonance using 20V zero-to-peak square input driving signal and optical inspection. All device "shapes" were also varied parametrically (lengths, widths, repetition of composing elements etc.), i.e. device families were fabricated on one and the same wafers using the same process we had been using so far, as for the electro-thermally actuation research. Figure 3.1 shows some of those devices.
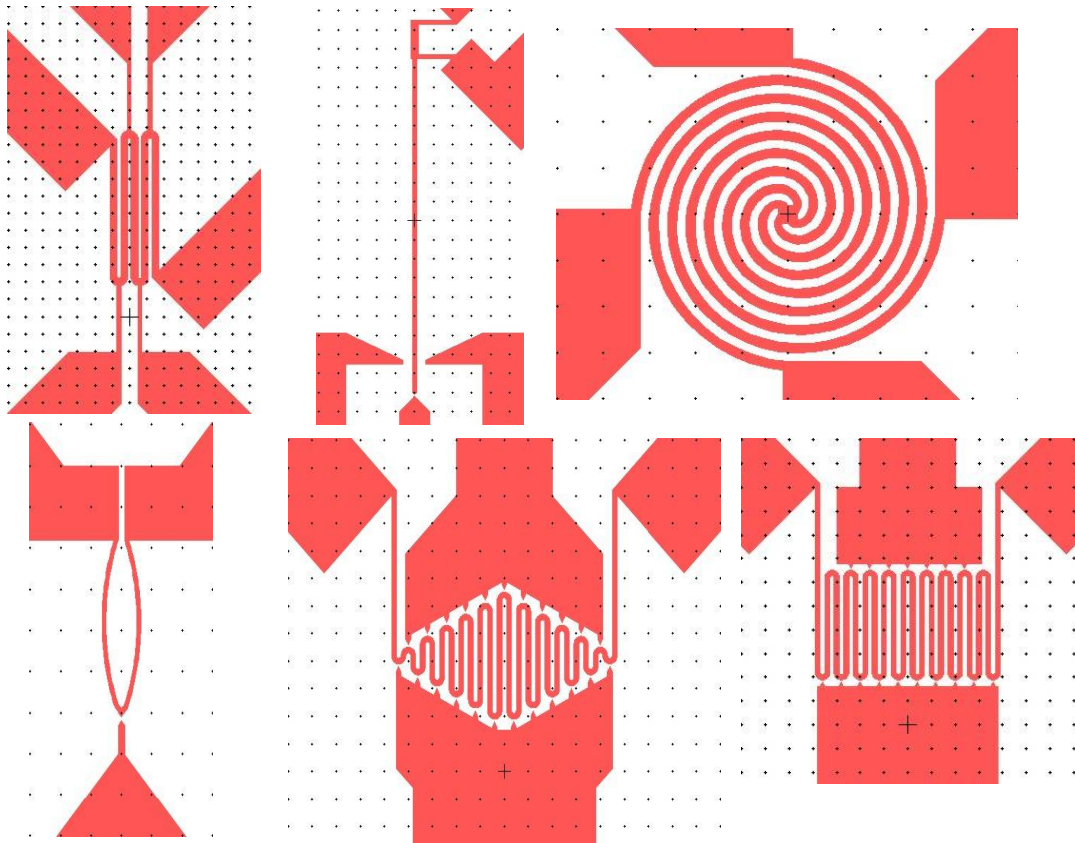

Figure 3.1: Some general research device examples, grid pattern is set to 10 µm, device linewidth is 2 µm

3.2 Self-magnetic actuation

One member of a device family were visibly actuating to resonance, so we chose those for further investigation.

3.2.1 Concept overview

Parallel conductors carrying opposing currents experience a mutual repulsive force as they both create electromagnetic fields around them and are repelled by each others fields. We used the same process as for the electro-thermally actuated devices, i.e. using a 2.5 μm thick LPCVD polysilicon layer on top of a 2 μm thick oxide layer on a Si substrate. The structures were defined by dry plasma etching of the polysilicon layer and subsequently the oxide was under-etched in HF to release the cantilever and the grill-shaped device. The width of the device is also the same, i.e. 2 μm, and the gaps between the parallel conductors are also 2 μm.

Several device permutations were fabricated, where we confined ourselves to using parallel conductors that are 80 μm long and varied the number of parallel conductors form 2 to 12 (Fig 3.2).
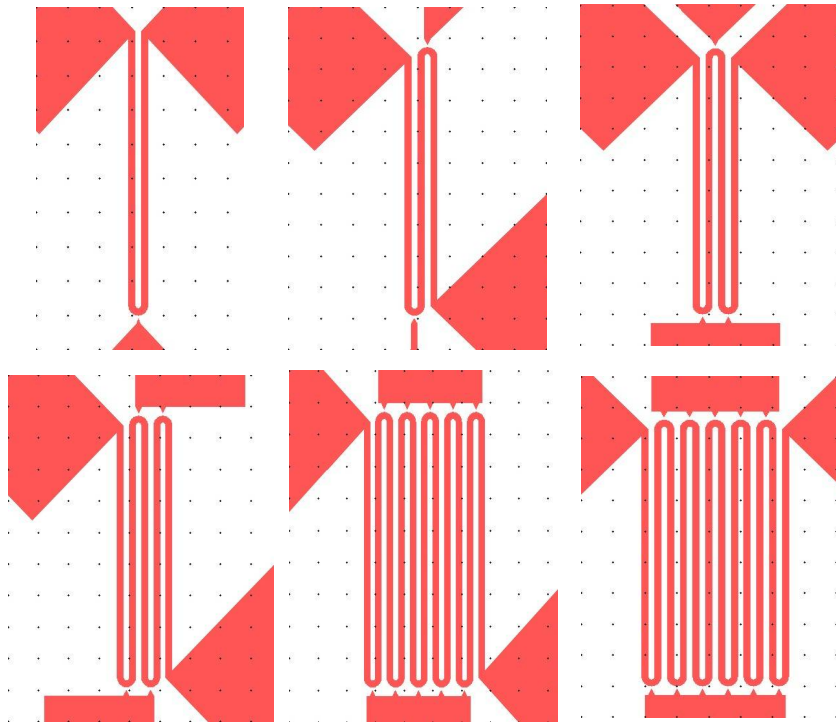

Figure 3.2: Self-magnetic device family, grid is set to 10 μm, device linewidth is 2 μm

3.2.3 Experimentation
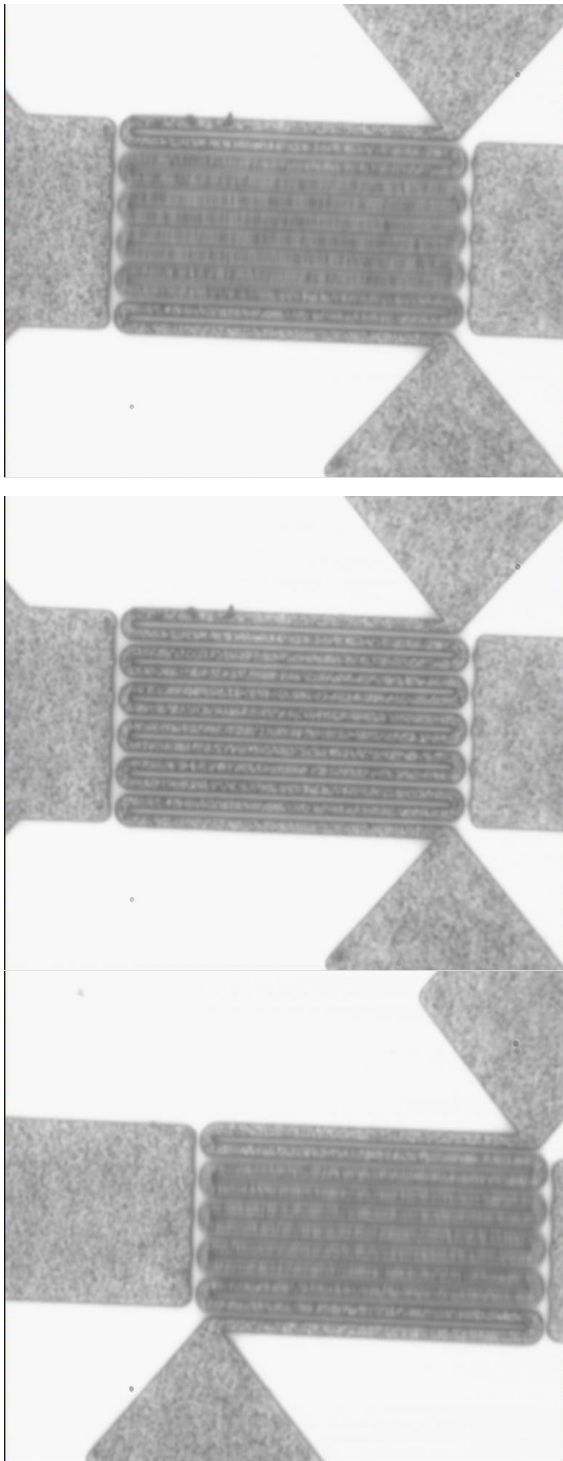
Figure 3.3: Self-magnetic devices
a) Still 12-conductor device
b) Resonating 12-conductor device
c) Resonating 11-conductor device

Resonance was observed by optical inspection in the case of 11 and 12 parallel conductor devices (Fig 3.3), at 87 and 112 kHz respectively. While the shorter device might also be actuating their resonance was not observable using a standard microscope. We suppose that this is due to their lower overall length and higher stiffness, which raises their resonant frequency, but lowers the resonant amplitude.

A conductor moving in a magnetic field experiences an induced EMF. We attempted to measure a change in those devices' impedance at resonance using a gain-phase analyzer (HP 4194A), where one of the device anchors was directly connected to the VH and CH, and the other anchor to the VL and CL inputs of the machine.

3.2.4 Applications and summary

The devices resistance, however is quite high (approx. 100-150 kOhms). The driving signal used was 20 V zero-to-peak. This means, as pointed out by Soren Dohn, MIC, that there is a considerable potential difference between individual parallel conductors; in essence, the devices consist of resistors in series that act as voltage dividers. This potential difference also creates electrostatic potentials between individual parallel conductors, i.e. the devices under test may well be electrostaticly actuated, rather than electromagnetically, as intended.

Electrostatic actuation falls outside the goals of our research as it does not perform well in polar liquids such as water, due to such mediums' extremely low dielectric constant, which results in very low filed densities in such mediums.

To make electromagnetic actuation dominant in parallel conductor devices we decided to fabricate such devices out of a highly conductive material (metal) which would raise the current densities, increase the electromagnetic fields, and lower the potential difference between individual device segments. To increase the EMF and detection signal we also decided to attempt to reduce the conductors gaps to bellow 2 μm, thus placing the conductors deeper in each other fields.

Chapter 4

Electron-beam lithography devices

Research into electro-thermally actuated rupture detection devices and self-magnetic actuation devices was continued using electron beam lithography. Rupture detection devices require precise linewidth control over the meniscus connection, and parallel conductor devices resonant signal would be increased by lowering the gap spacing between individual segments. High power electron beam lithography offers the possibility of defining linewidths as low as 10nm, which is ideal for both lines of research.

We have used 500nm thick layers of ZEP-520A resist throughout the e-beam fabricating research; those were spun on 2 inch wafers at 2000 RPM, 100 rpm/s acceleration and 30 seconds spin time. Baking was done at 160 deg. C, for 5 minutes.

We used 6 nA current, 280 $\mu c/cm^2$ dose, 100 keV acceleration voltage and 10nm step for electron beam writing of all patterns.

ZED-N50 was used to develop the written patterns, for 50 sec.

4.1 Polysilicon fabrication

In order to be true to our stated motivation and goals we strove to use a fabrication process that uses as little e-beam writing time and keep the fabrication cost as low as possible.

Writing cantilever devices that have linewidths in the order of 2 μm, and large flat anchors using negative resist process would have been extremely wasting on e-beam writing time given the large areas that needed to be defined.

We could have combined UV lithography with E-beam lithography and use that instead for anchor definition. However, this would have been against our stated research values as well, as it would have increased the number of fabrication steps.

Hence, we decided to use positive resist (ZEP 520A) and only write the outlines of the intended devices.

We used 1.5 μm outlines and an array of 250 nm squares outside those outlines so that the polysilicon layer outside the device outlines could be underetched in HF. The squares array spacing was progressively increased from left to right at the mask level, so that the left side of the chips would be underetched earlier, with respect to right side.

1) Anisotropic etch of poly layer defining outlines and dot pattern

2) Wet HF etch of oxide layer beginning

3) Wet HF etch of oxide layer progress

Anchor

Dot pattern   Anchor outline

LPCVD Polysilicon

LPCVD Silicon oxide

Silicon substrate

4) Wet HF etch of oxide layer releases poly layer partially

5) Wet HF etch of oxide layer releases poly layer completely

Figure 4.1: Dot pattern positive process sequence and release mechanism

Chips we fabricated using 2 inch wafers with a 2.5 μm thick LPCVD polysilicon layer on top of a 2 μm thick oxide layer on a Si substrate. The structures were defined by dry plasma etching of the polysilicon layer and subsequently the oxide was under-etched in HF to release the dotted array portions of the polysilicon layer and the suspended devices.

The reason for the differential array spacing was a design attempt to make the released portions of the polysilicon layer "open" in a "sardine-can-like" fashion under the influence of a out-of-plane stress within the polysilicon layer that would make it curl upwards and from left to right, during the HF etching step (Figure 4.1)

Figure 4.2 shows a chip overview. Figure 4.3 shows an electro-thermal actuator defined using the above means; one can also see the dot array outside the device outline. Figure 4.4 demonstrates the meniscus mask level definition for a resonant rupture detection device.
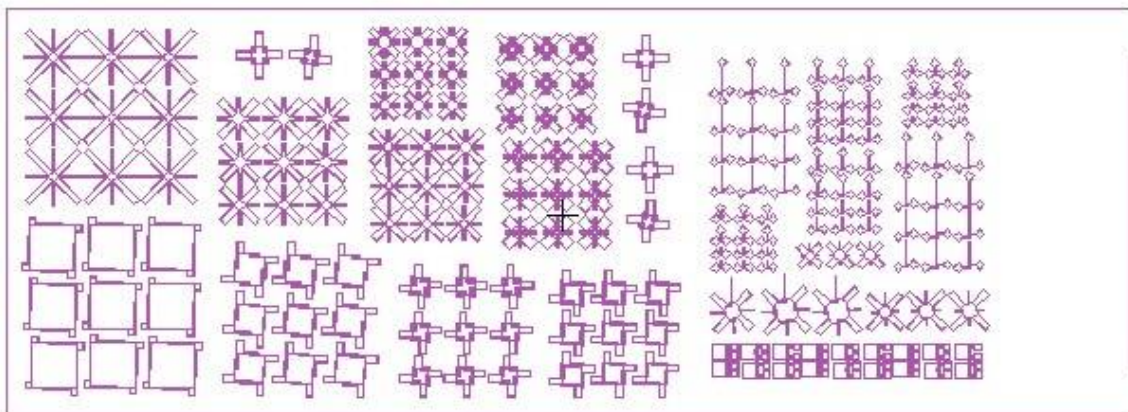

*Figure 4.2: Positive resist/dot array processing chip mask overview*
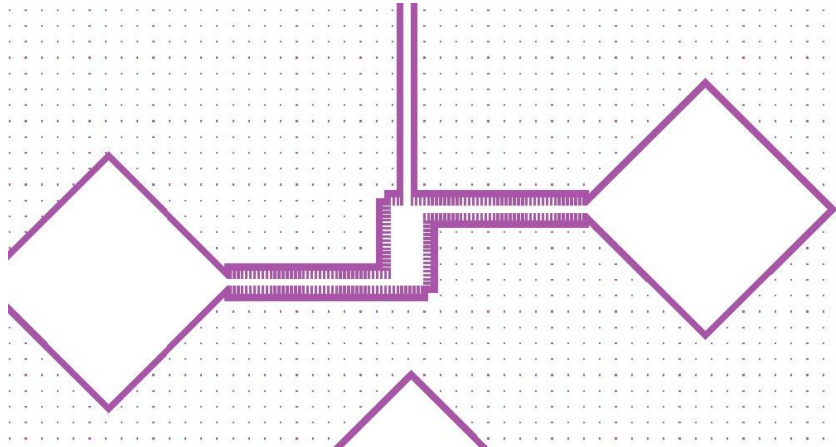
Figure 4.3: Dynamic electro-thermal actuator mask overview and top layer underetch dot pattern
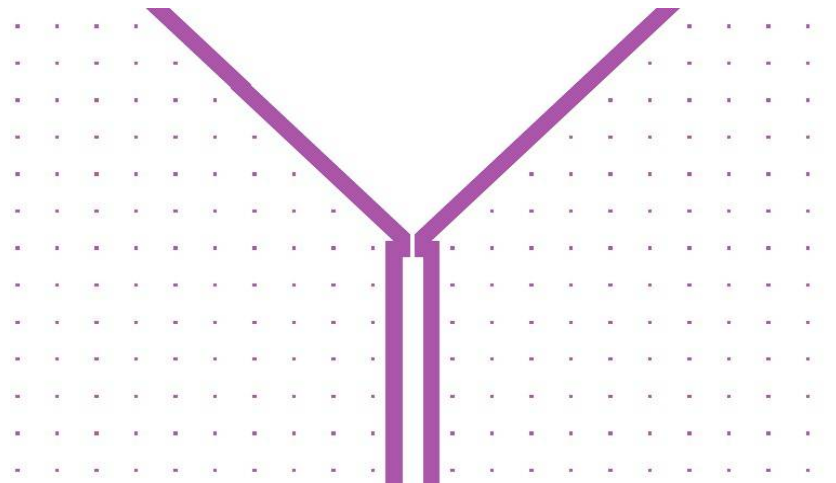
Figure 4.4: Rupture detection meniscus mask overview

We were unable to obtain a thick LPCVD polysilicon layer with the required stress gradient and realize the goal of making the top polysilicon layer curling upwards during release.

We were, however, successful in fabricating devices using a thinner 500 nm LPCVD polysilicon layer (Figure 4.5, 4.6)
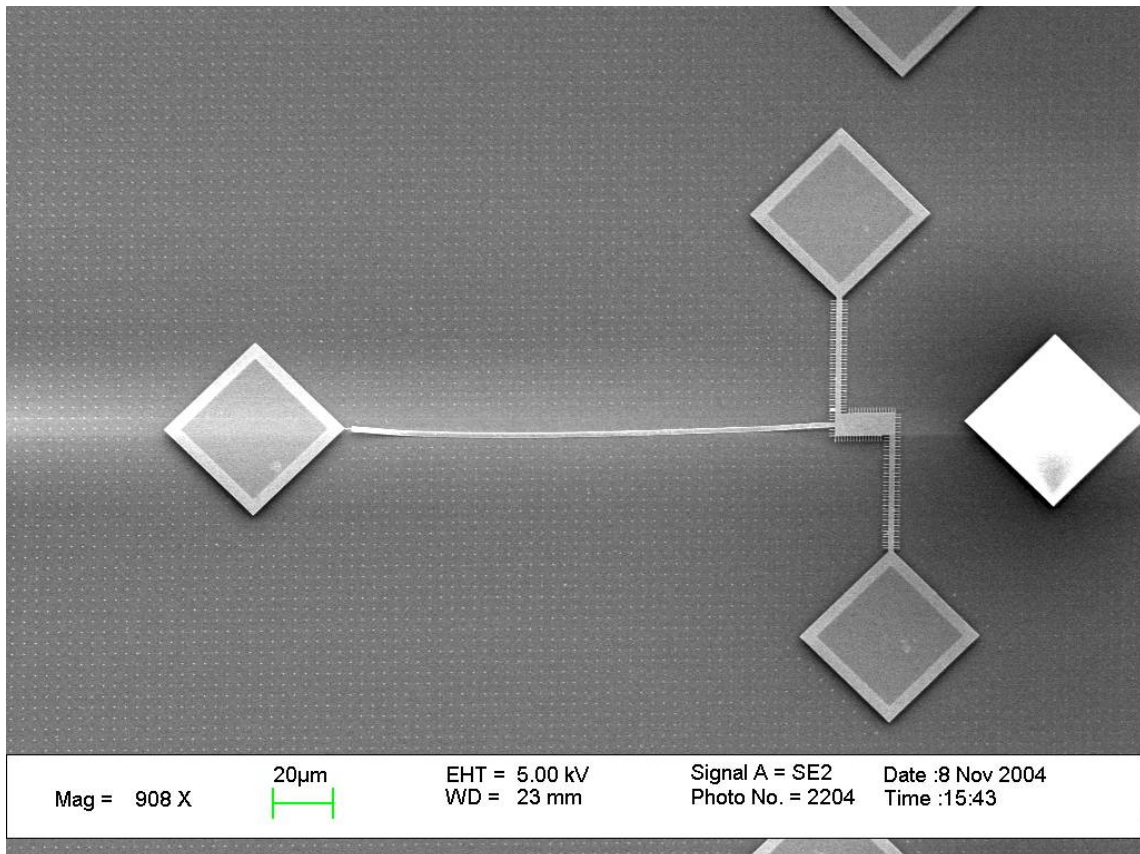
Figure 4.5: Dynamic electro-thermal actuation rupture detection device
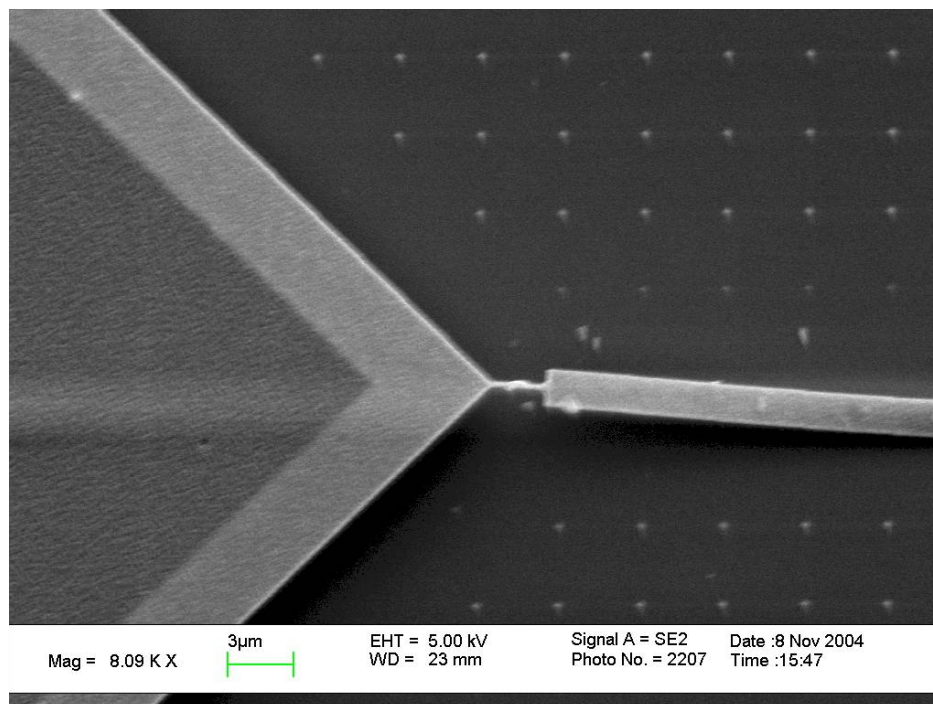
Figure 4.6: Rupture detection meniscus close-up

Flat structures are, unfortunately, impossible to be used for electro-thermal actuation or detection, at least given the specific devices configuration and outlines.

4.2 Metal Fabrication

Research into fabricating the self-magnetic devices that we described in Chapter 3 was undertaken using aluminum as a first choice; it is a high conductivity material which serves to maximize the magnetic fields around the device's parallel segments. E-beam lithography was used to reduce the segment/parallel conductor gaps to below what was achievable with UV lithography.

Dry processes are preferable for nano-fabrication for two reasons; liquid fabrication steps are difficult to control, and suspended structures are usually destroyed during such steps, especially if ultrasound is used for lift-off. Some solutions to this problem have been successfully implemented such as freeze-drying [42] and thin resist spin and plasma ashing [23]. Yields for those solutions, however, are not particularly high.

4.2.1 Peel-off processing

We invented a simple solution to this problem; we used a conventional lift-off process where the wet processing step of removing a top metal layer using ultrasound in a liquid environment is replaced by applying blue lab tape (Scotch TM) and peeling the top layer off. The resist layer can then be removed by plasma ashing, and the metal structures released by reactive ion etching of the silicon substrate. Figure 4.7 demonstrates the process. Resist is spun on a silicon wafer, the mask pattern is written using e-beam lithography and the resist layer is then developed. A thin aluminum layer (100-200nm) is then sputtered as for conventional lift-off processing. Lab tape (that is normally stuck to the backside of silicon wafers to hold pieces together as the wafers are being cut into chips) is then digitally applied to the top side of the chips. The tape is then peeled-off taking the top metal layer with it; we have found that aluminum adheres much better to the tape than to the resist underneath. We also experimented with chromium metal layers with similar results. The metal remaining on the substrate is then under etched using reactive ion etching to release the suspended metal structures.
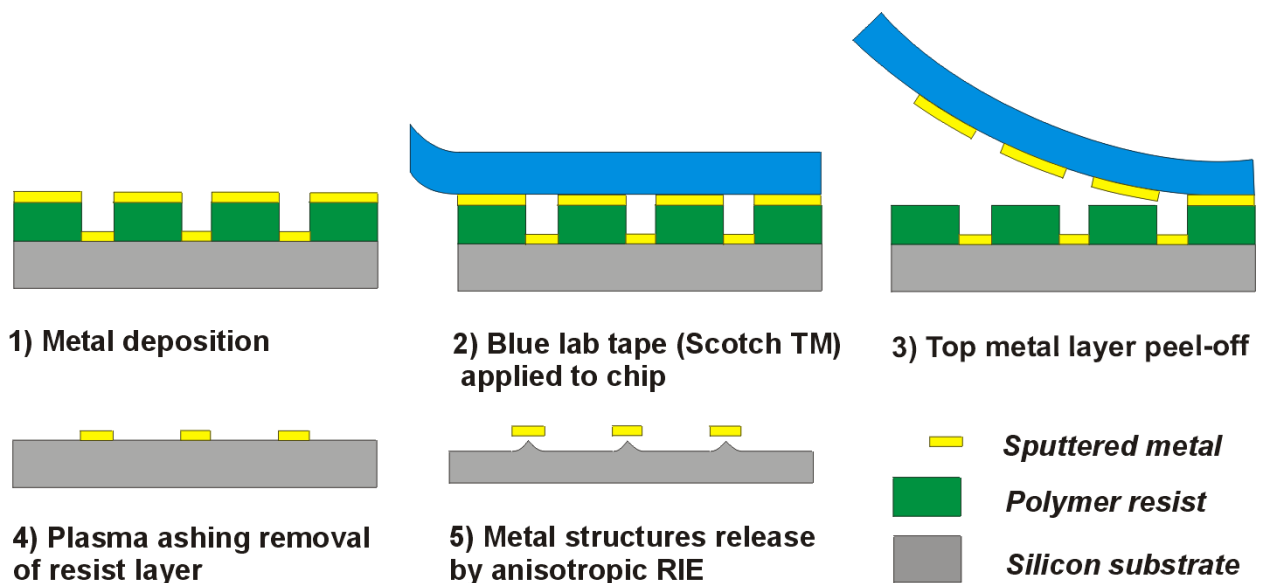

Figure 4.7: Peel-off dry processing and fabrication of suspended metal structures

Most metals have a thermal expansion coefficient that is higher than that of silicon; this thermal

coefficient mismatch and the elevated temperatures of deposition lead to the build up of internal stress gradient across the thickness of the deposited metal layer (Figure 4.8). After release this stress manifests itself by expanding the structures sideways towards their anchoring points and curving them towards the substrate. Daniel Hafliger, MIC, pointed out during discussions on the matter that metal deposition rates affect the in-built deposition stress; low deposition rates result in high stresses and vice versa. With that in mind we used as high deposition rates as possible, i.e. 3.0 nm/s.
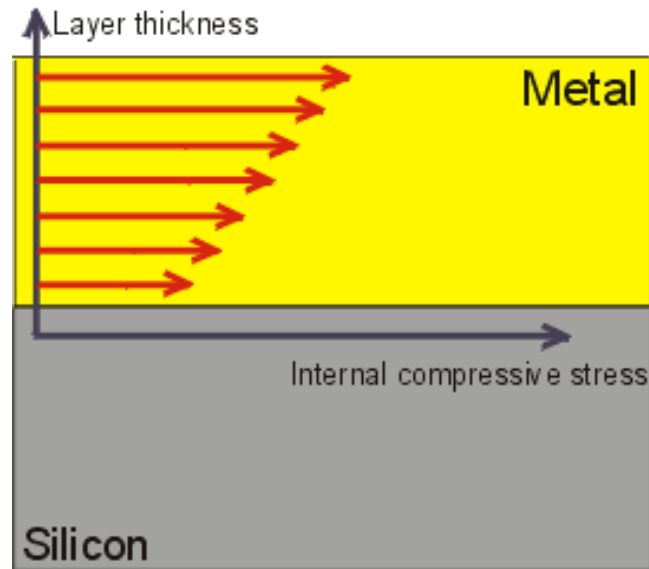
Figure 4.8: Internal stress build-up and gradients in a sputtered metal layer

Several shapes' reaction to the in-built deposition stress was explored. While some maintained their shape better than others (Figure 4.9), all were bent to a small or larger extent.
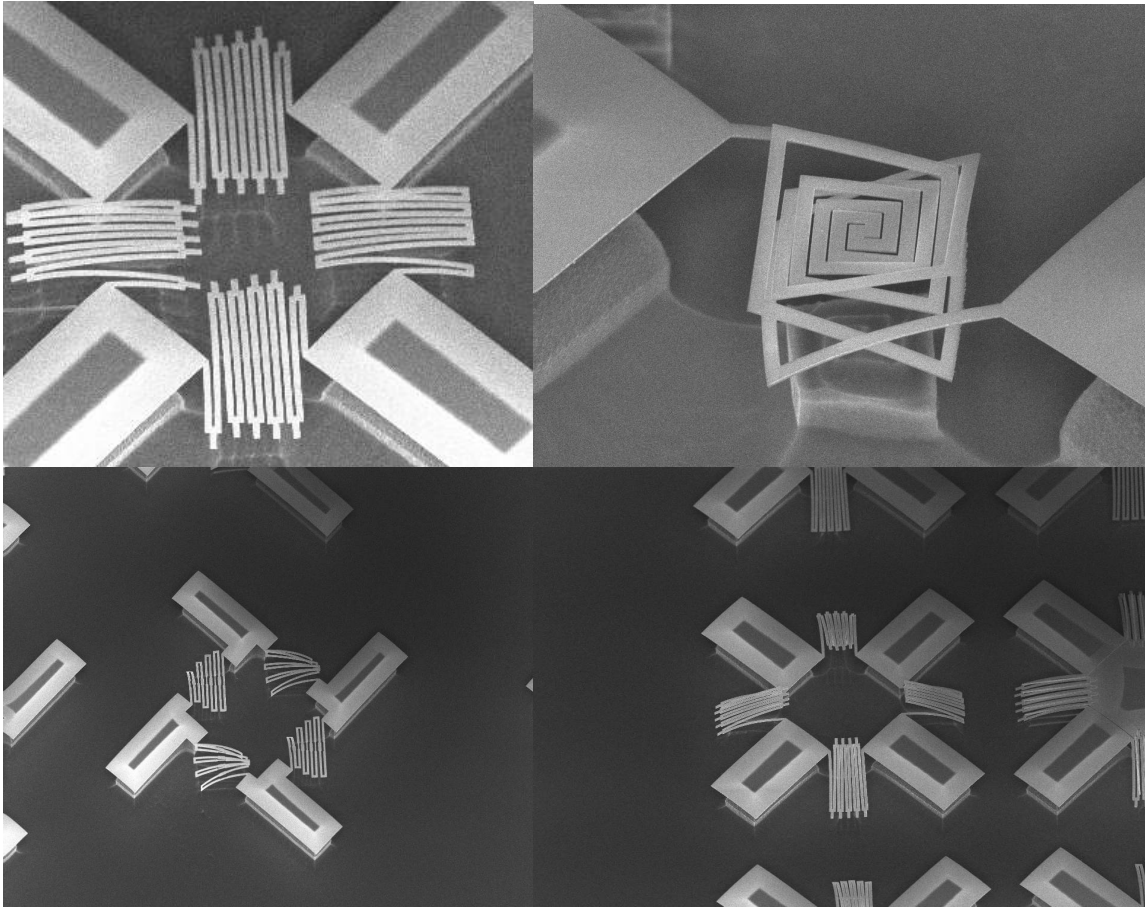
Figure 4.9: Parallel conductor/"grill" devices behavior after release

Figure 4.9 shows two types of parallel conductor devices – a meandering/grill arrangement, and double spiral device. Three kinds of grill device anchoring can be seen with respect to the imaginary axis that connects the two anchoring points.

– the anchor axis line lays midway across the devices,

– the anchor axis line lays diagonally across the device

– the anchor axis line lays along one of the sides of the device

We found that meandering/grill/ parallel conductor structures that are symmetric with respect to their two anchoring points are better at preserving their shape. In other words, if an imaginary axis is drawn between the two anchoring points, the structure that would preserve its shape best is the one which is as close to a mirror image of itself as possible with respect to that axis. Double spiral structures that can also be used to fabricate two parallel conductors were found to be most susceptible to the in-built stress and preserved their shape worst.

An attempt was made to increase the stiffness of the structures by increasing their thickness and reintroducing a wet-etching fabrication step (Figure 4.10).

1) Metal deposition

2) Timed HF wet etch of Aluminum metal layer

3) Blue lab tape (Scotch TM) applied to chip

4) Top metal layer peel-off

5) Plasma ashing removal of resist layer

6) Metal structures release by anisotropic RIE

☐ *Sputtered metal*
■ *Polymer resist*
■ *Silicon substrate*
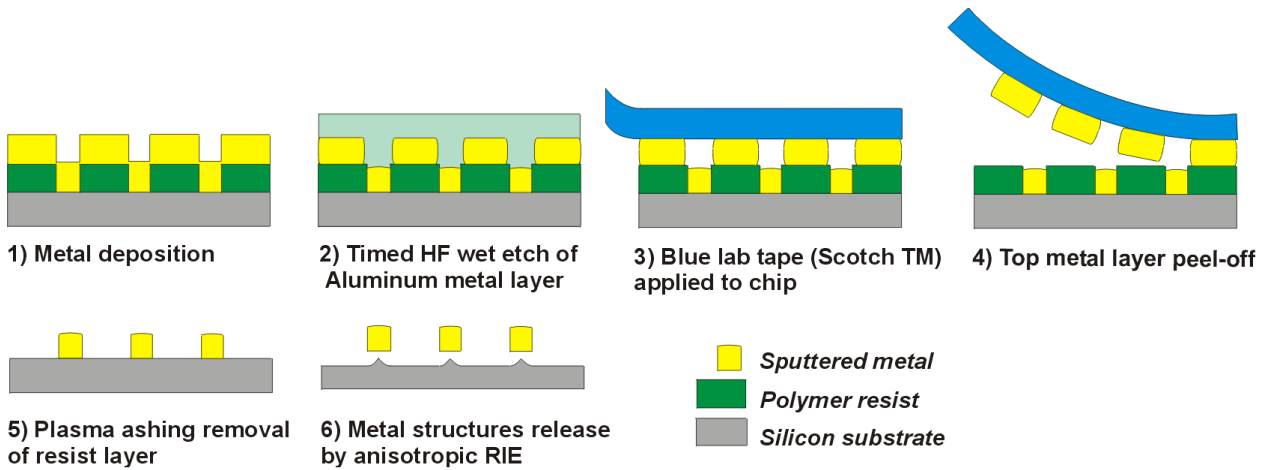
Figure 4.10: Peel-off processing with an added HF etch step

This is the same process as the peel-off process previously described, except that the deposited metal layer is 550 nm thick, i.e. thicker than the resist layer which is 500nm. To disconnect the metal layer into two layers – one in the resist patterned "trenches" and one on top of the resist layer, a timed 40% BHF fabrication step was introduced; the aluminum layer was etched for 40 sec which reduced its thickness and all exposed sides by approximately 100nm, severing the narrow connection between top and bottom metal layers, and allowing peel-off.

While this worked to some extent, it resulted in structures that seem to have considerable surface roughness and non-uniform behavior after release (Figure 4.11).
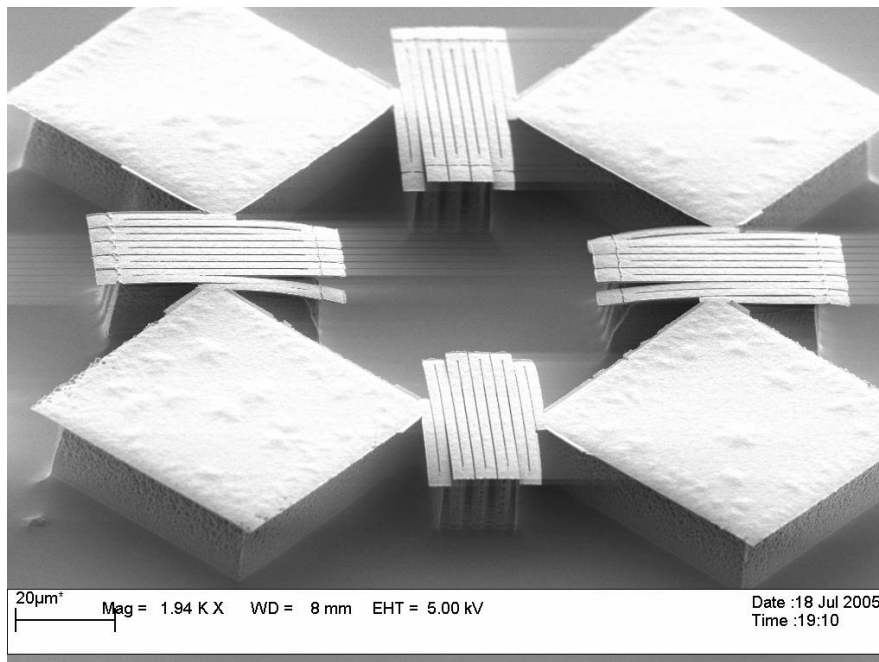
Figure 4.11: HF peel-off fabricated balanced "grill" structures

4.2.2 Pattern transfer

The metal layer that was peeled-off by the tape, and remains on the tape was also investigated, using 200 nm thick aluminum layers. The metal pattern was transferred to the tape fairly well in some places with an overall yield of approximately 20%. Figure 4.12 shows successful transfer of the top metal layer obtained after peel-off fabrication of grill and double-spiral suspended structures.
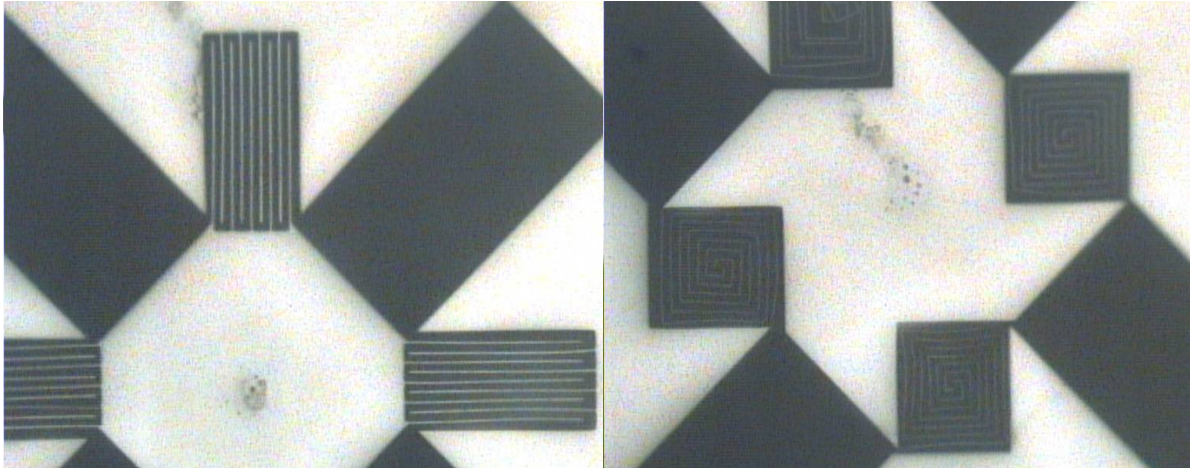

Figure 4.12: Metal pattern transfer on blue tape, white areas are metal, dark areas are holes in the metal layer through witch the underlaying tape is visible

An attempt was made to fabricate micro channels by applying another piece of tape on the other side of the metal layer, i.e. sandwiching the peel-off metal pattern between two sheets of tape. In essence this would have produced 2 μm wide channels separated by 400 nm channel walls.

This was unsuccessful, possibly due to the low metal layer thickness and large channel widths; air bubbles trapped across the intended channels indicated that the channel are not full of air, i.e. there is no free channel (Figure 4.13).
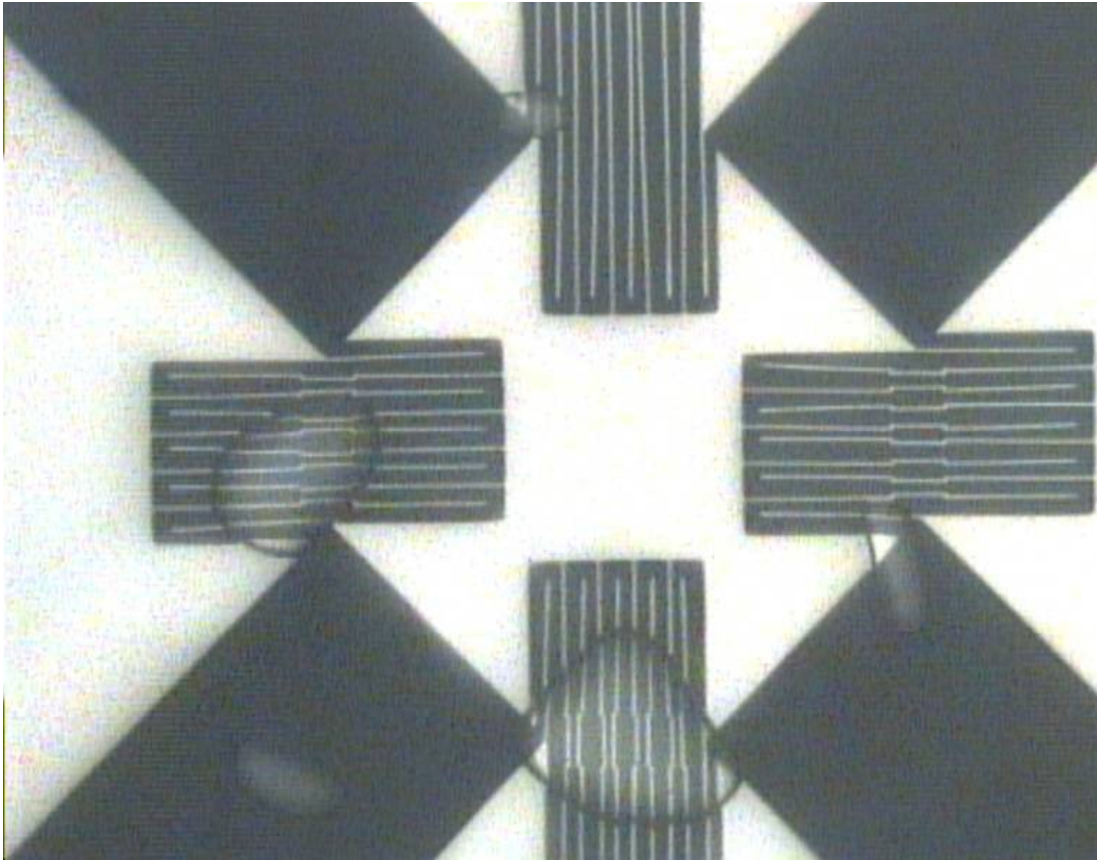
Figure 4.13: Metal layer sandwiched between two sheets of tape. Air bubbles trapped between the layers indicate the absence of true channels.

An attempt was made to rectify this by spotting a drop of DI water on top of the metal layer prior to applying the second tape sheet, i.e. fill the intended channels with fluid prior to encapsulating them.

This was only partially successful due to bad adhesion; we could not obtain a solid composite.

While water was trapped between the layer and within the channels its was found that the polymer-metal-polymer sandwich delaminates easily when pressure is locally applied using a probe station needle tip, i.e. the encapsulated fluid was migrating from the channels to interface between the metal and polymer layers under pressure.

A possible solution to this would be to use plain polymer sheets that are bonded to the metal layer using pressure and heat, rather than glue.

4.2.3 Angled deposition

Increasing the structures' thickness does increase the second moment of area, making them more rigid, but extra thickness also introduces more internal stress, within the additional deposited metal.

One way to solve this problem is a structure that has a large second moment of area, but as little cross-sectional area as possible, i.e. a beam.

A solution to this problem is the fabrication of structures that have a Z-cross-section or U-cross-section. These beam cross-section shapes increase the second moment of area in all axis which means that structures composed of such beams would be much stiffer and resistant to bending than beams made of thin flat strips of metal.

A structure defined by a line on the mask level translates into a grove developed into a resist layer on a substrate. This grove already does have one of the desired shapes – it is U-shaped in cross-section. Therefore, uniform deposition of metal that covers the sidewalls of the resist as well as the exposed parts of the substrate would produce the desired cross-sectional shape, as long as the metal layer on top of the resist and around the structures can be cut away and removed.

One way to do so is to do multiple metal depositions at an angle to the substrate (i.e. angle the substrate with respect to the electron beam) until all the sidewalls are covered in consecutive depositions. We have solved the problem of lifting the unnecessary metal off, by drawing narrow trenches around and parallel to the lines defining the structures. If the angle of deposition is lower than the angle between the trench diagonal and substrate, then a geometrical self-shadowing effect takes place; the deposited metal is shadowed by one of the sides of the trench and covers the opposite sidewall only partially. The bottom of such trenches remains uncovered by metal.

This separates the metal layer along the lines of the narrow trenches and allows lift-off processing and fabrication, described in more detail in the next sections of the chapter.

A holder was made to facilitate subsequent angled depositions in conventional e-beam metal deposition equipment. It consists of a aluminum metal plate bent at 45 deg. to the horizontal, to which a chip with the drawn lithography pattern is attached. The pattern is angled at 45 deg to the chip sides. Rotating the chip by 90 deg. between depositions was used to change the deposition angle (Figure 4.14).
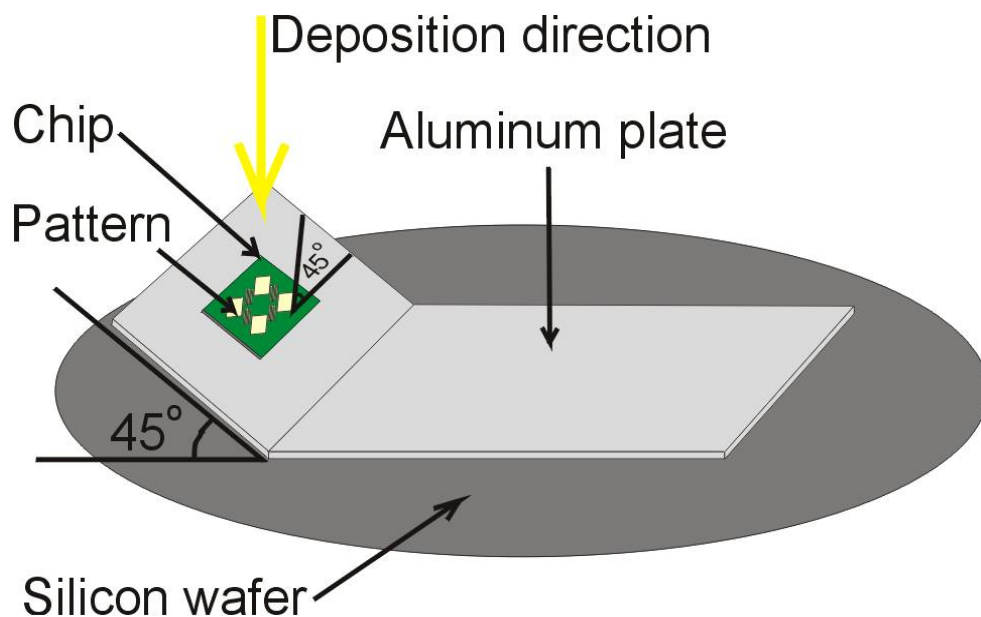

Figure 4.14: Angled deposition mechanism

An L-edit macro file was written to automate mask making and facilitate parametric optimization (Appendix C).

Z-cross-section beams, U-cross-section beams, hexagonal and rectangular patterned anchors were all researched using this software, by drawing arrays of devices and "picking" the ones that worked for subsequent investigation. Trench linewidths were varied between 125 nm and 300 nm, and device linewidths were varied between 1 μm and 2 μm. The process was standardized

after completion the research on the optimal anchoring.

4.2.4 Z-cross-section beam structures

Z-shape cross-sectional beams were fabricated by two subsequent depositions at 45 deg. vertical to the plane of the substrate, 45 deg. to the direction of intended structures and 90 deg. to each other in the plane of the substrate, i.e. by rotating the chip once at 90 deg. Between the two depositions. Figure 4.15 shows the process sequence.


1) Angled metal deposition

2) Timed plasma ashing of resist layer

3) Top metal layer peel-off

4) Plasma ashing removal of resist layer

5) Metal structures release by anisotropic RIE

Sputtered metal

Polymer resist

Silicon substrate
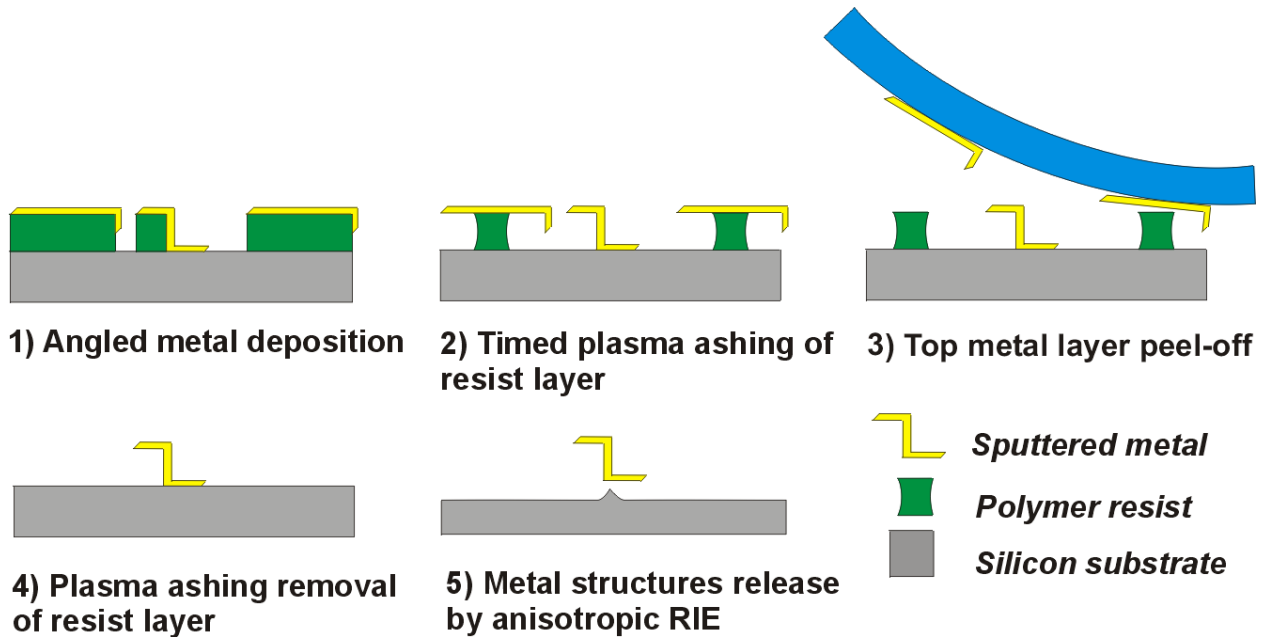
Figure 4.15: Z-cross-section structures peel-off fabrication process

A metal layer is deposited at an angle by sputtering. The resist layer is then dry etched using oxygen plasma to facilitate peel-off. The top metal layer is then peeled-off and the remaining exposed resist layer removed by further oxygen plasma ashing. The metal structures are then suspended/underetched using reactive ion etching of the silicon substrate.
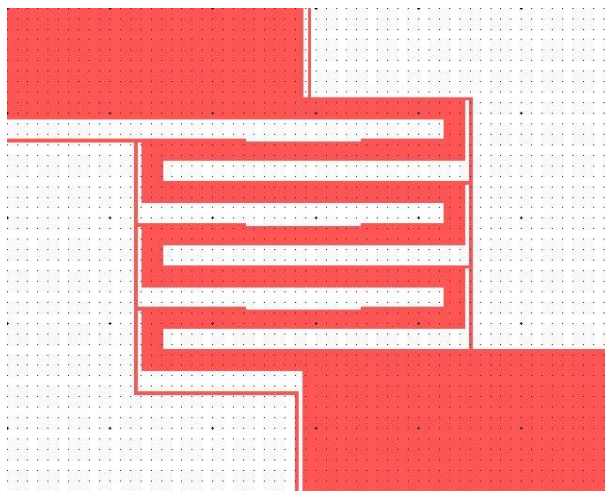
Figure 4.16: Z-cross-section structure mask example. Grid pattern is set to 1 μm

Figure 4.16 shows a device mask used for fabrication. The structures we found to be well aligned and shaped after processing (Figure 4.17, 4.18), but the anchoring (attachment to the substrate), was bending some of the suspended elements downwards (Figure 4.19). The anchors fabricated using this process are flat metal plates surrounded by a vertical "fence" on three sides. While this "vertical" fencing was preventing the bending of the corners down on two sides, the corners/points of attachment of the side lacking a "fence" were twisting downwards, bringing the suspended structure attached to them downwards as well. To rectify this problem a triangular pattern was added to the anchor side lacking fencing (Figure 4.20, 4.21, 4.22) – this provided the necessary support in the form of the "back" side of the triangles. The triangles' angle was smaller than 90 deg. which ensured that their back side would also be covered with metal, thus providing vertical fencing.
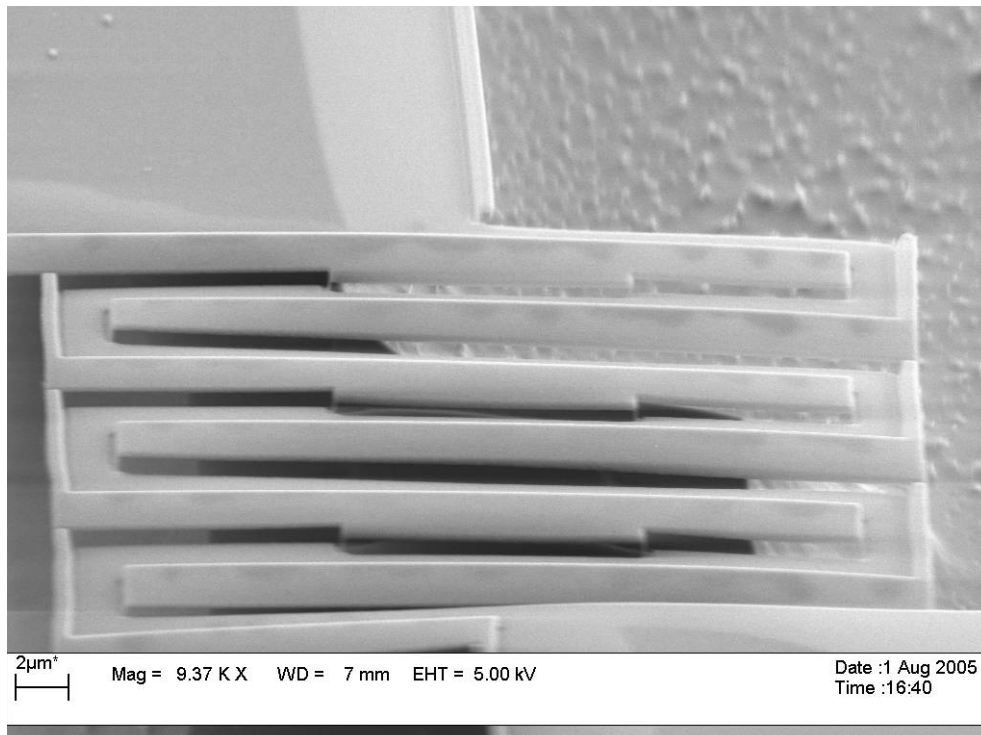
Figure 4.17: Z-cross-section structure
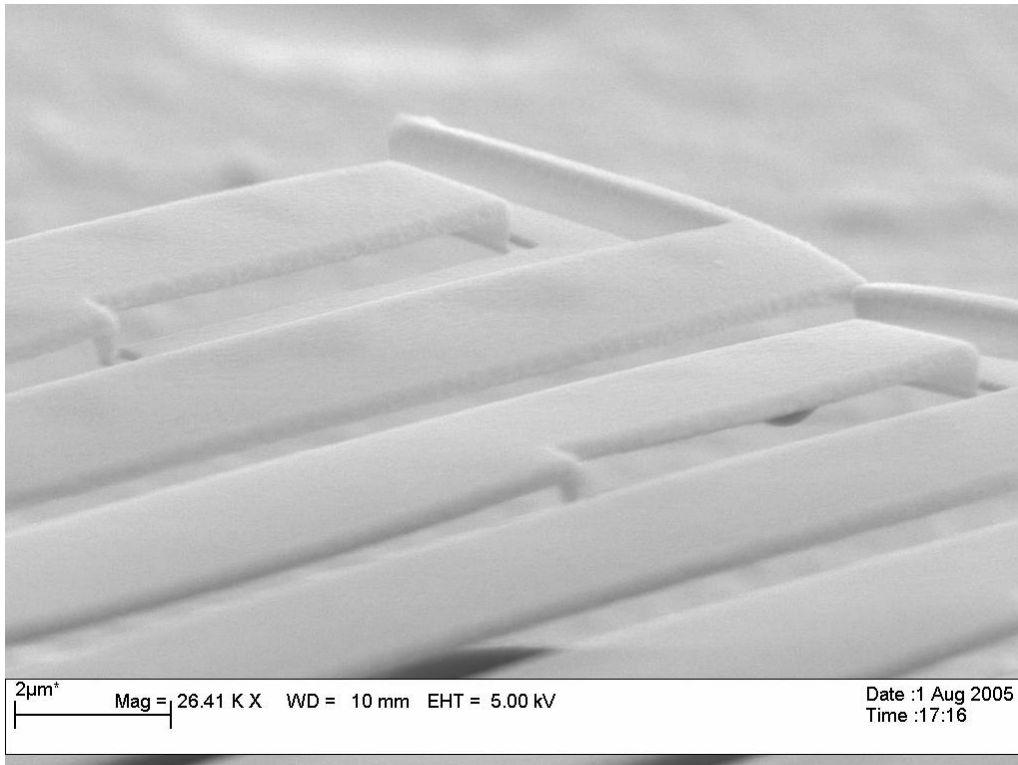
Figure 4.18: Z-cross-section structure close-up view
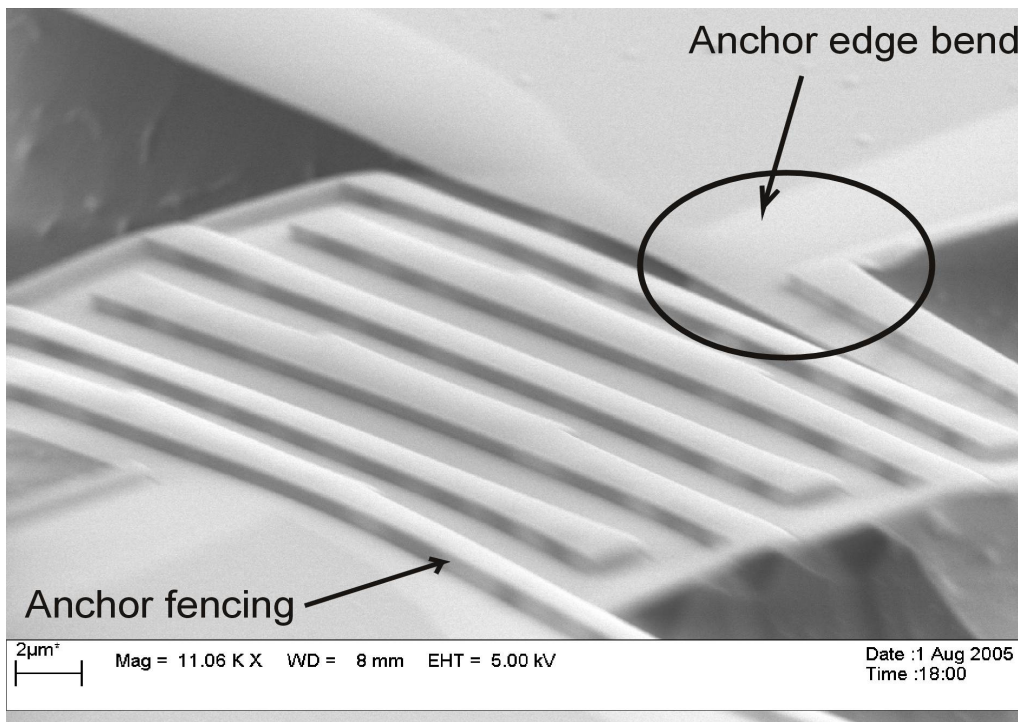
Figure 4.19: Z-cross-section structures anchor edge bend and fencing.
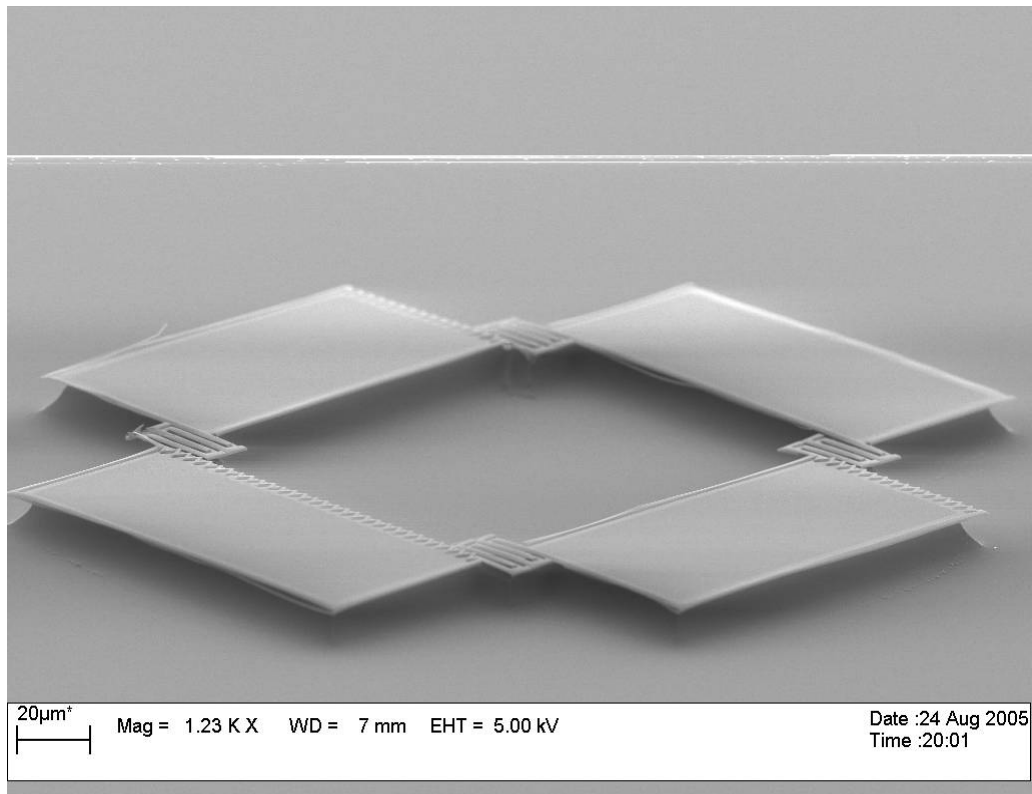
Figure 4.20: Triangular anchor fencing pattern
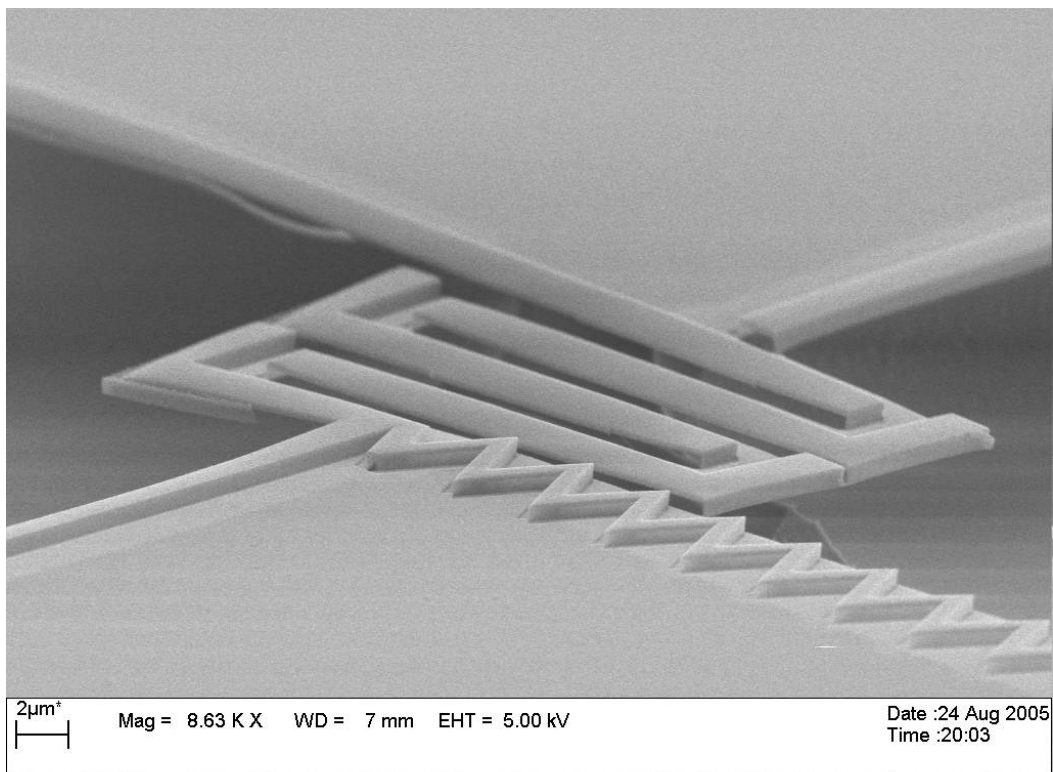
Figure 4.21: Triangular anchor fencing close-up. Device segment connected to triangular pattern is relatively straight; pattern prevents anchor edge from bending.
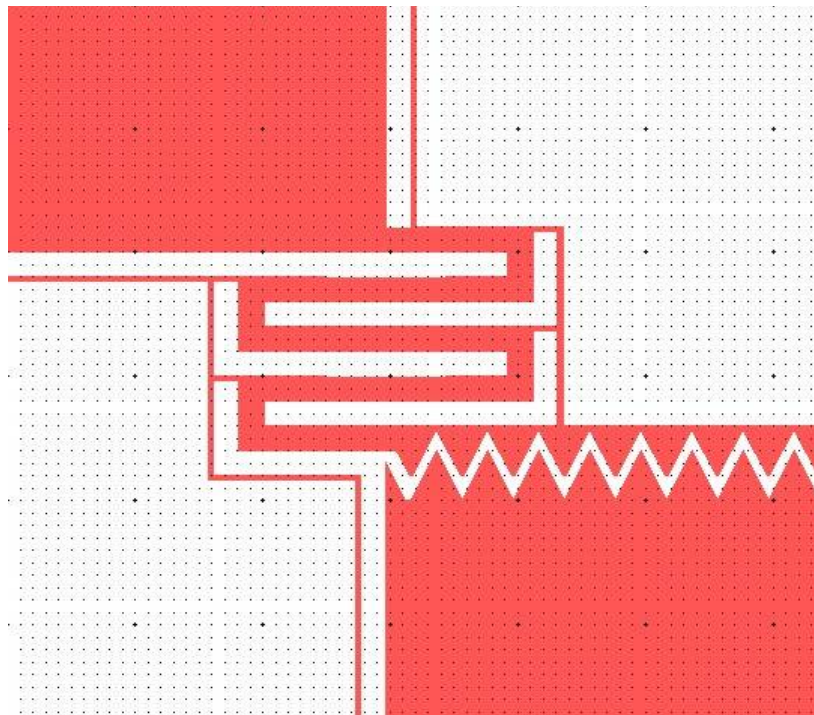
Figure 4.22: Triangular anchor fencing Z-cross-section structure mask. Grid pattern is set to 1 μm

4.2.5 U-cross-section beams

U-shape cross-sectional beams were fabricated using four subsequent depositions at 90 deg. to each other, 45 deg. to the plane of the chip, and 45 deg. to the direction of the pattern, i.e. rotating the chip four times by 90 deg. between subsequent depositions. Figure 4.23 demonstrates the process sequence

1) Angled metal deposition

2) Timed plasma ashing of resist layer

3) Top metal layer peel-off

4) Plasma ashing removal of resist layer

5) Metal structures release by anisotropic RIE

Sputtered metal

Polymer resist

Silicon substrate
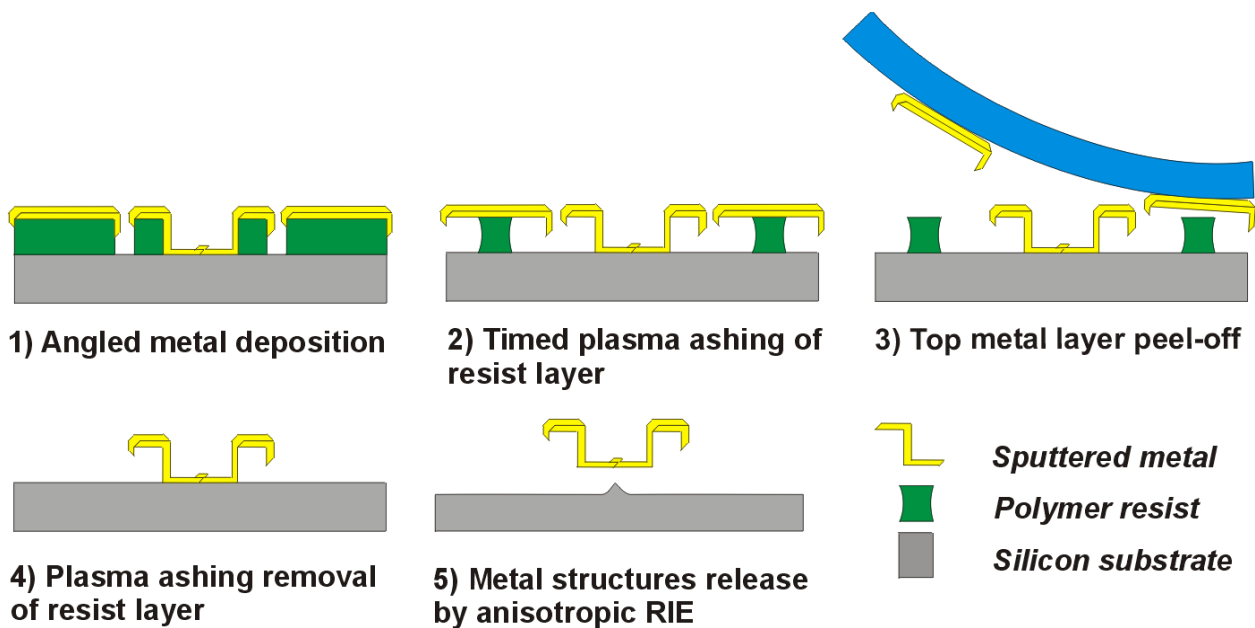
Figure 4.23: U-cross-section structures peel-off fabrication process sequence

The process is exactly the same as for the Z-cross-section devices, except for the difference in mask designs. The chips were rotated four times at 90 deg on the deposition folder between subsequent metal depositions. Figure 4.24 shows a device mask example.
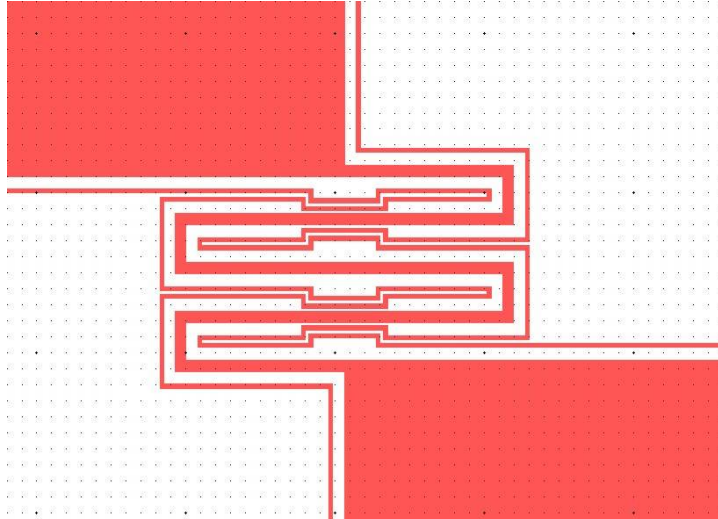
Figure 4.24: U-cross-section structure mask example. Grid pattern is set to 1 μm

This process sequence also has the added benefit of easy fabrication of anchors that are fenced on all four sides. Relatively well aligned structures were fabricated at low under-etch anchor distances (Figure 4.25), but at large under-etch distance the anchors' fencing was found to be too week to prevent the attachment points form curving and distorting the structures' shape (Figure 4.26).
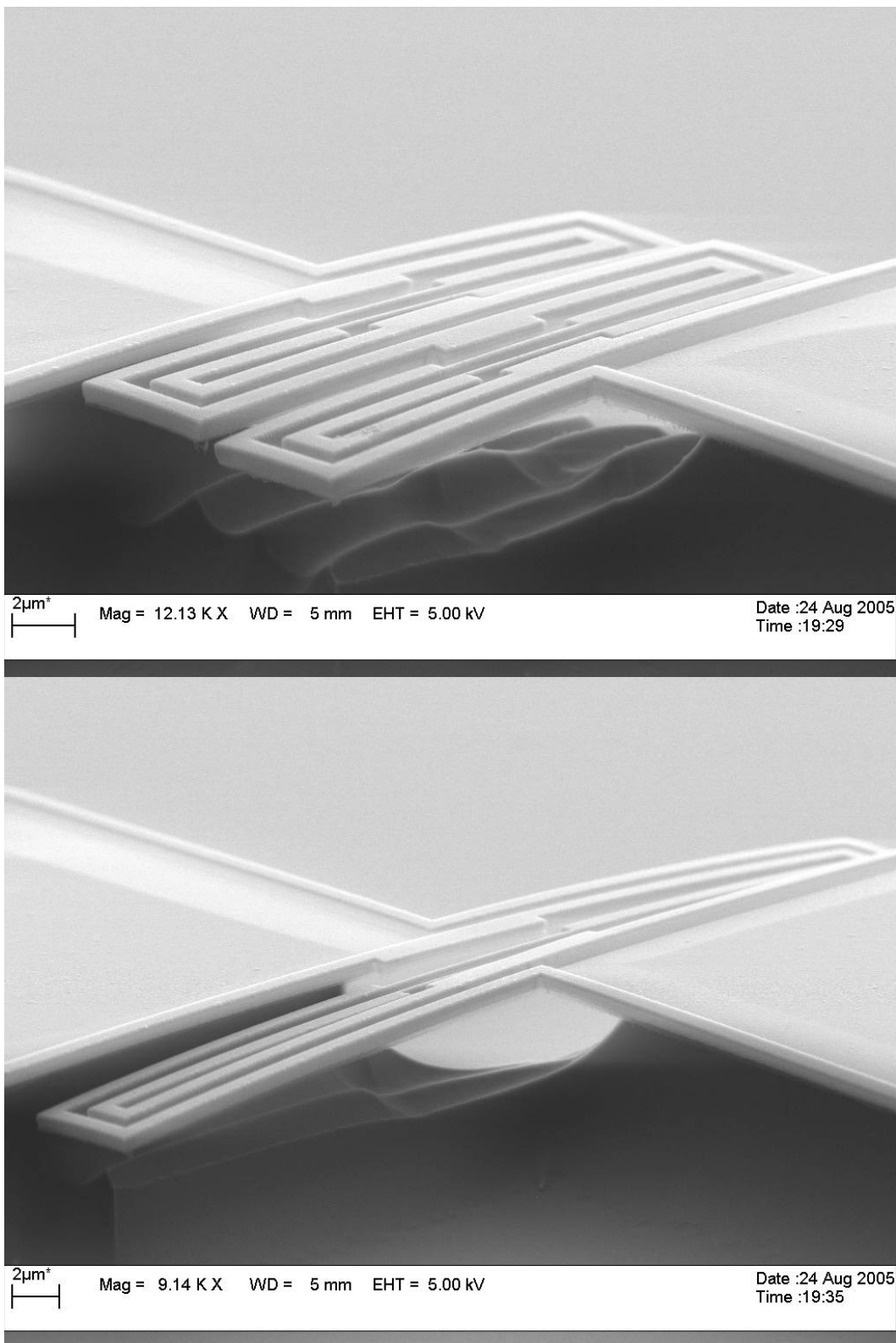
Figure 4.25: U-cross-sectional devices close-up, small anchor under-etch
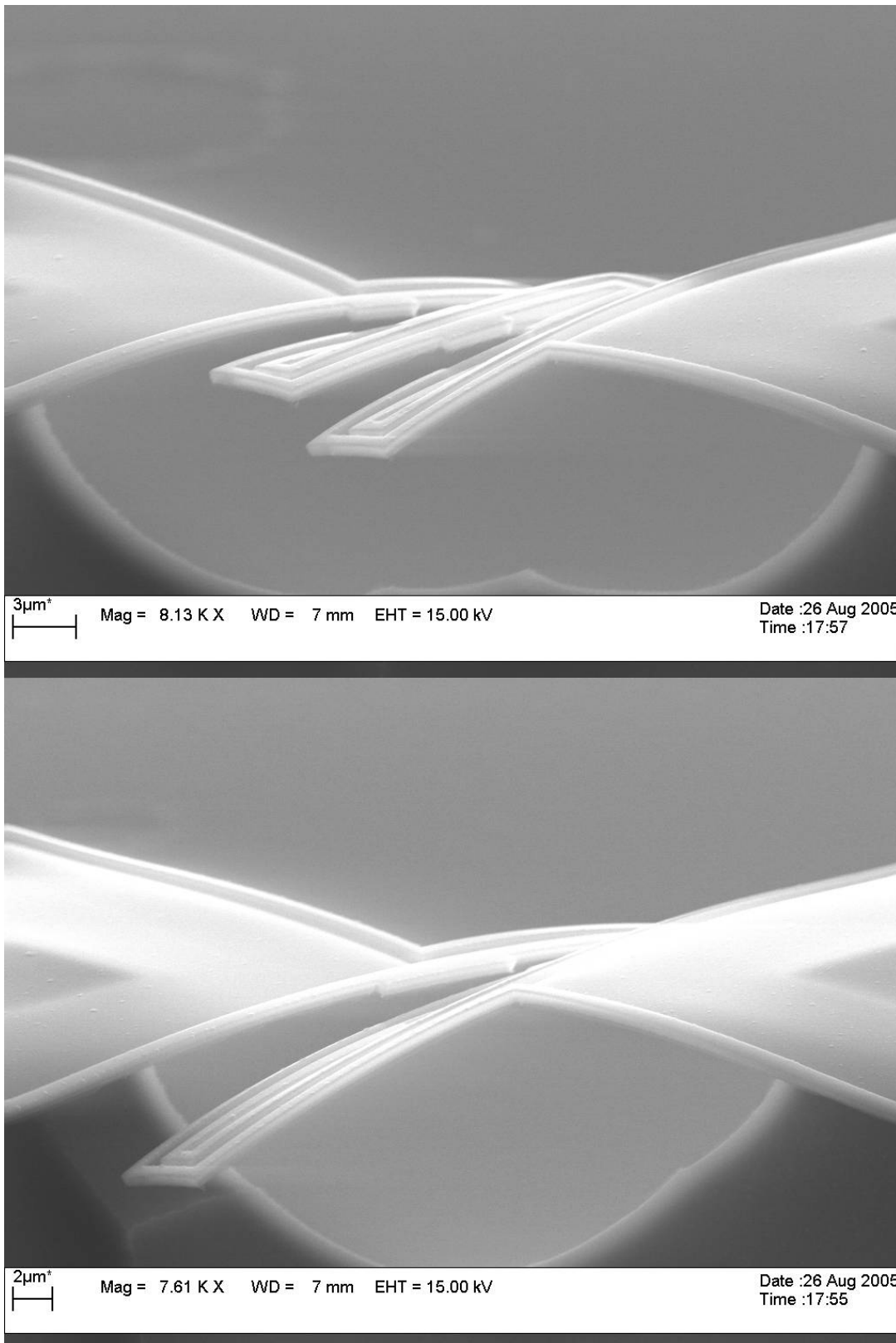
Figure 4.26: U-cross-sectional devices close-up, large anchor under-etch

4.2.6 Anchoring

Different "patterned" anchors were fabricated in order to determine the best anchoring; hexagonal and rectangular patterns were introduced on the anchoring plates in order to stiffen them in an attempt to prevent twisting at the edges. Short and long anchor under-etch distances were experimented with (Figure 4.27, 4.28, 4.29, 4.30). Both long and short devices were found to bend downwards at larger under-etch distances, regardless of the anchoring pattern, suggesting that a further investigation in the influence of anchoring on suspended structures was needed.

Figures 4.31 and 4.32 demonstrate the mask file level implementation of the two different patterns.
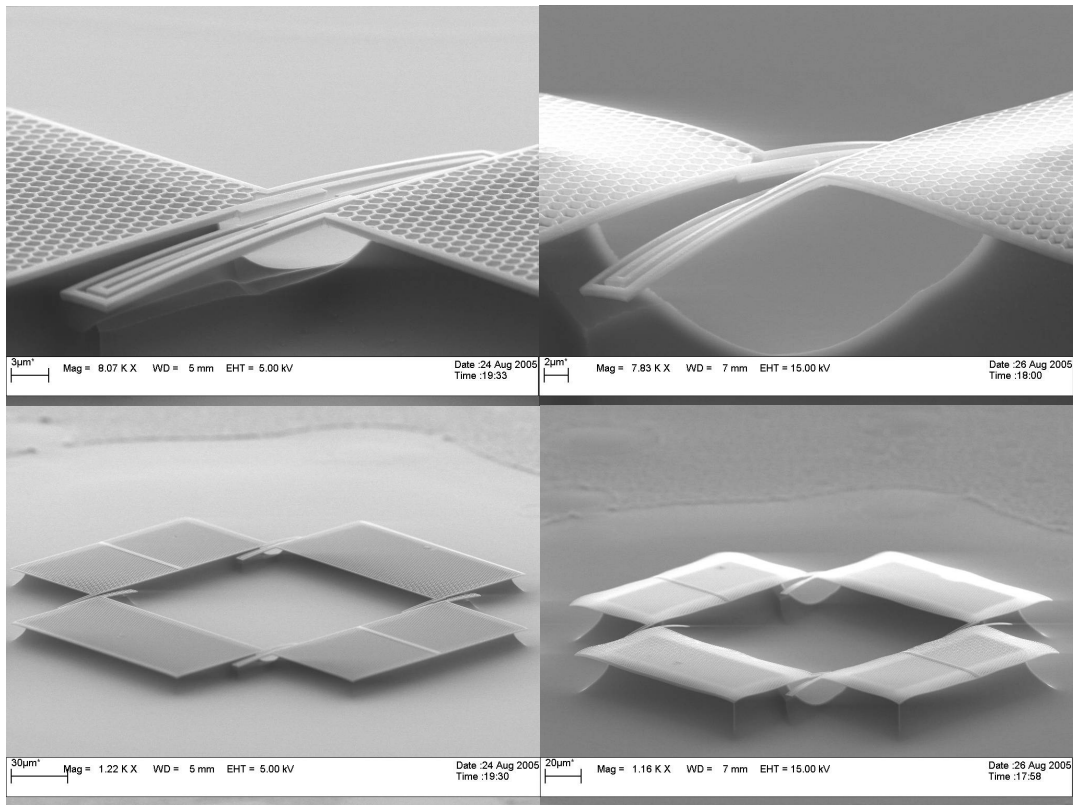
Figure 4.27: Hexagonal patterned anchoring long structures behavior at small (left) and large (right) under-etch distances
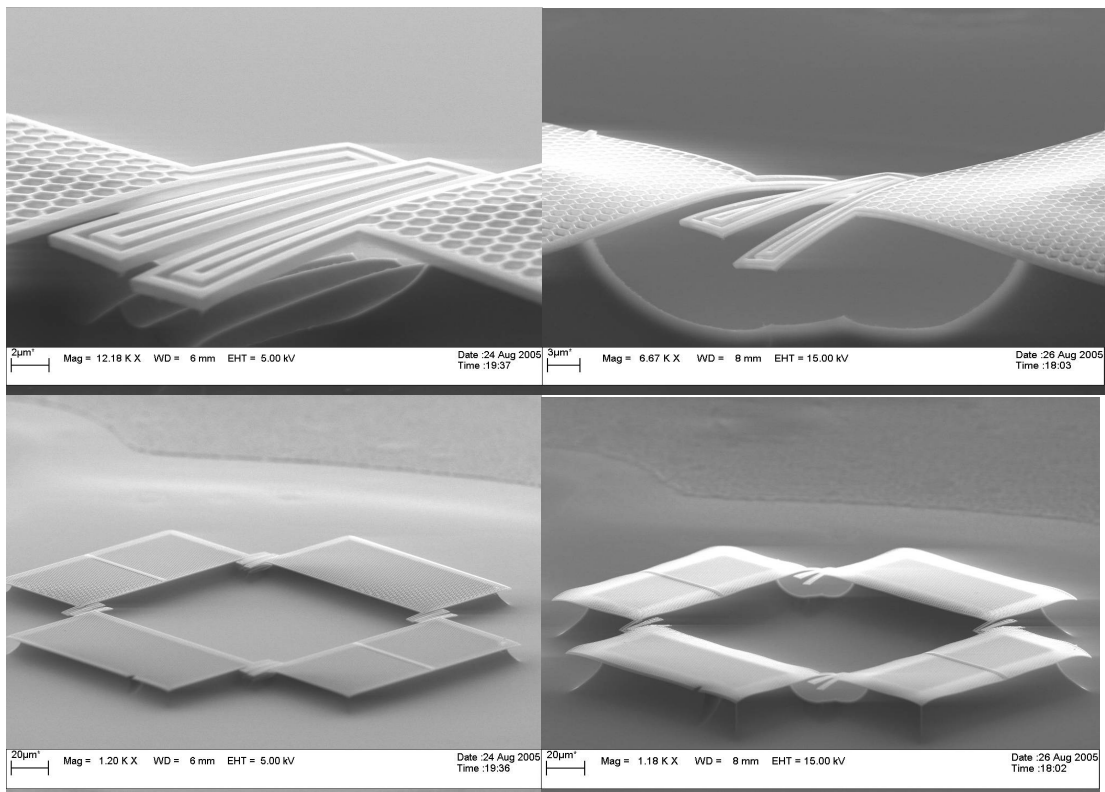
Figure 4.28: Hexagonal patterned anchoring short structures behavior at small (left) and large (right) under-etch distances
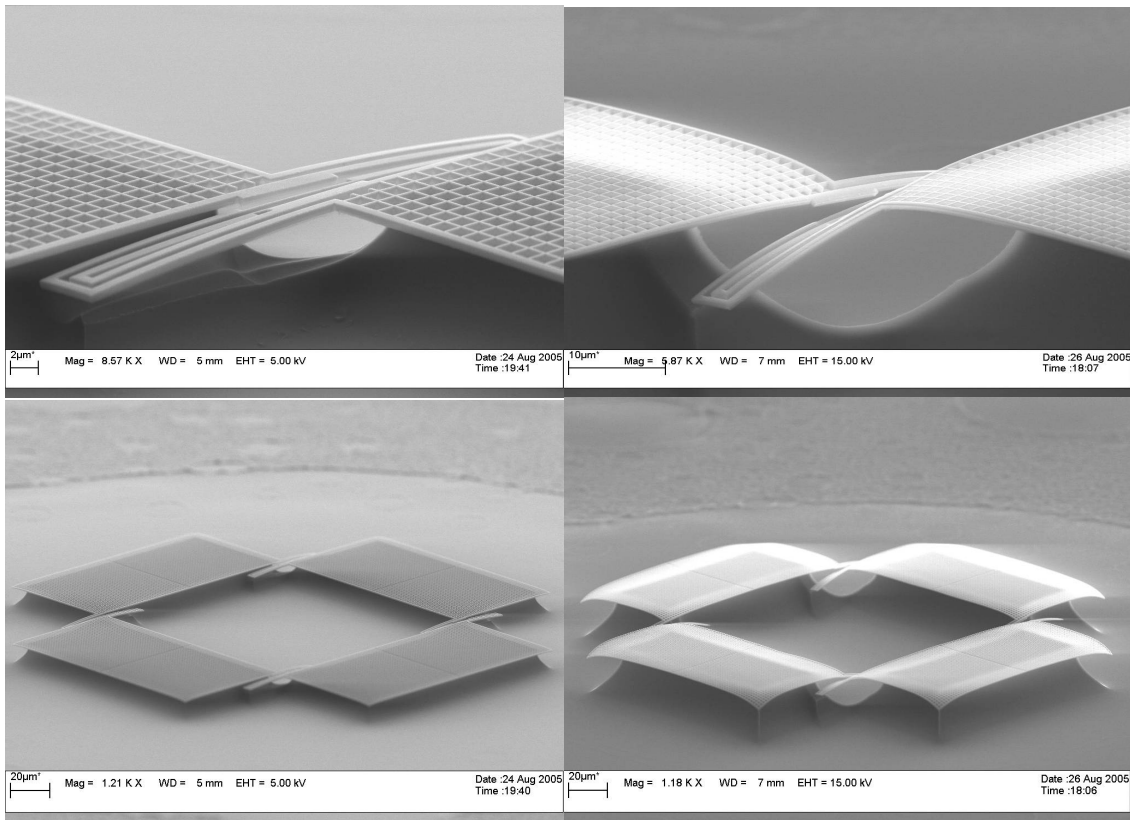
Figure 4.29: Rectangular patterned anchoring long structures behavior at small (left) and large (right) under-etch distances
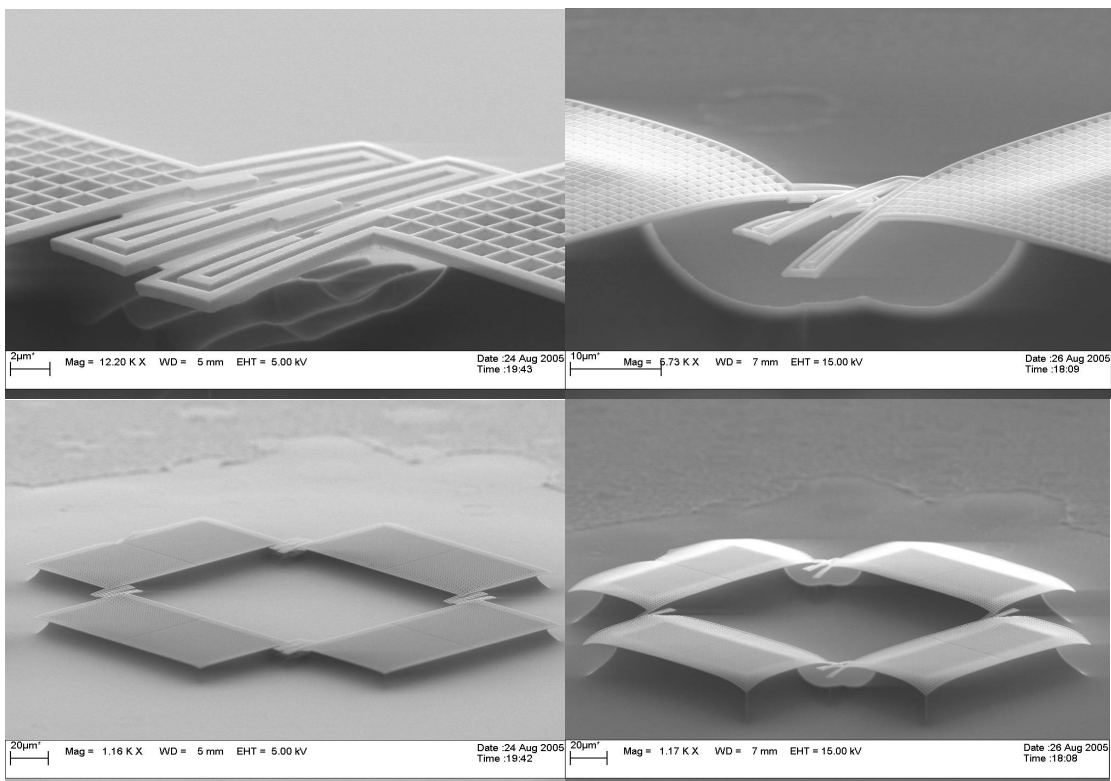

Figure 4.30: Rectangular patterned anchoring short structures behavior at small (left) and large (right) under-etch distances
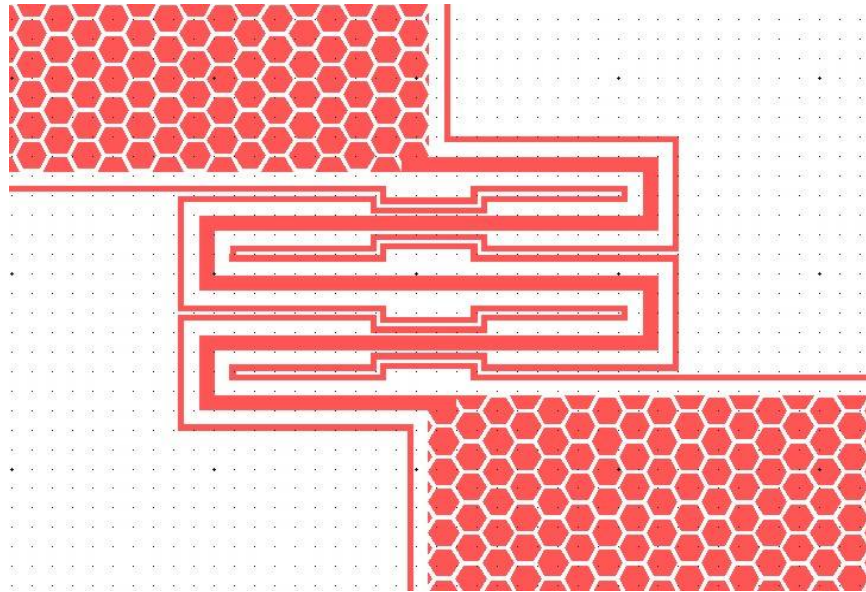
Figure 4.31: Hexagonal anchor pattern mask. Grid pattern is set to 1 μm
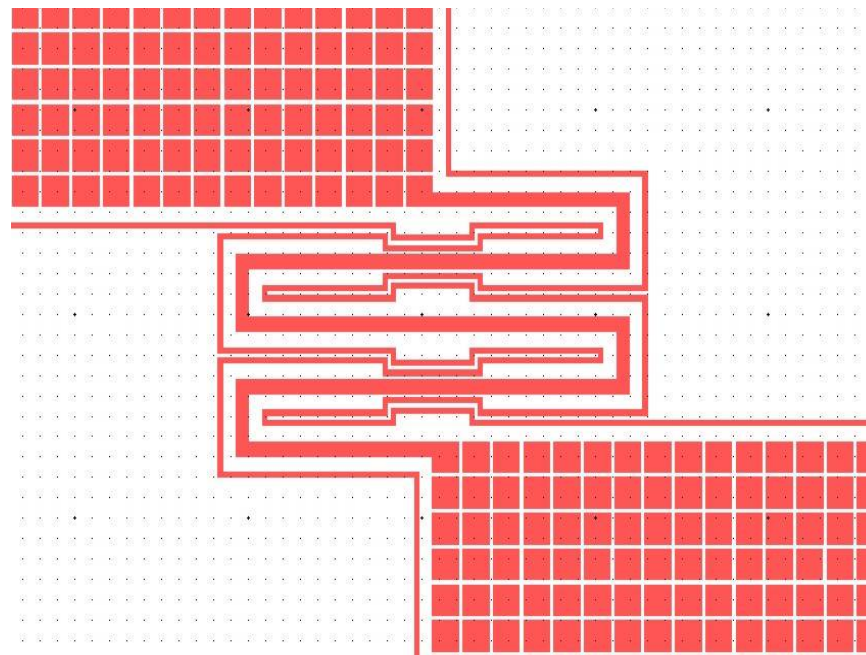
Figure 4.32: Rectangular anchor pattern mask. Grid pattern is set to 1 μm

The different anchoring plates behavior (no pattern, hexagonal pattern, rectangular pattern) was investigated by observation at the anchoring edge shape at low angles (Figure 4.33).
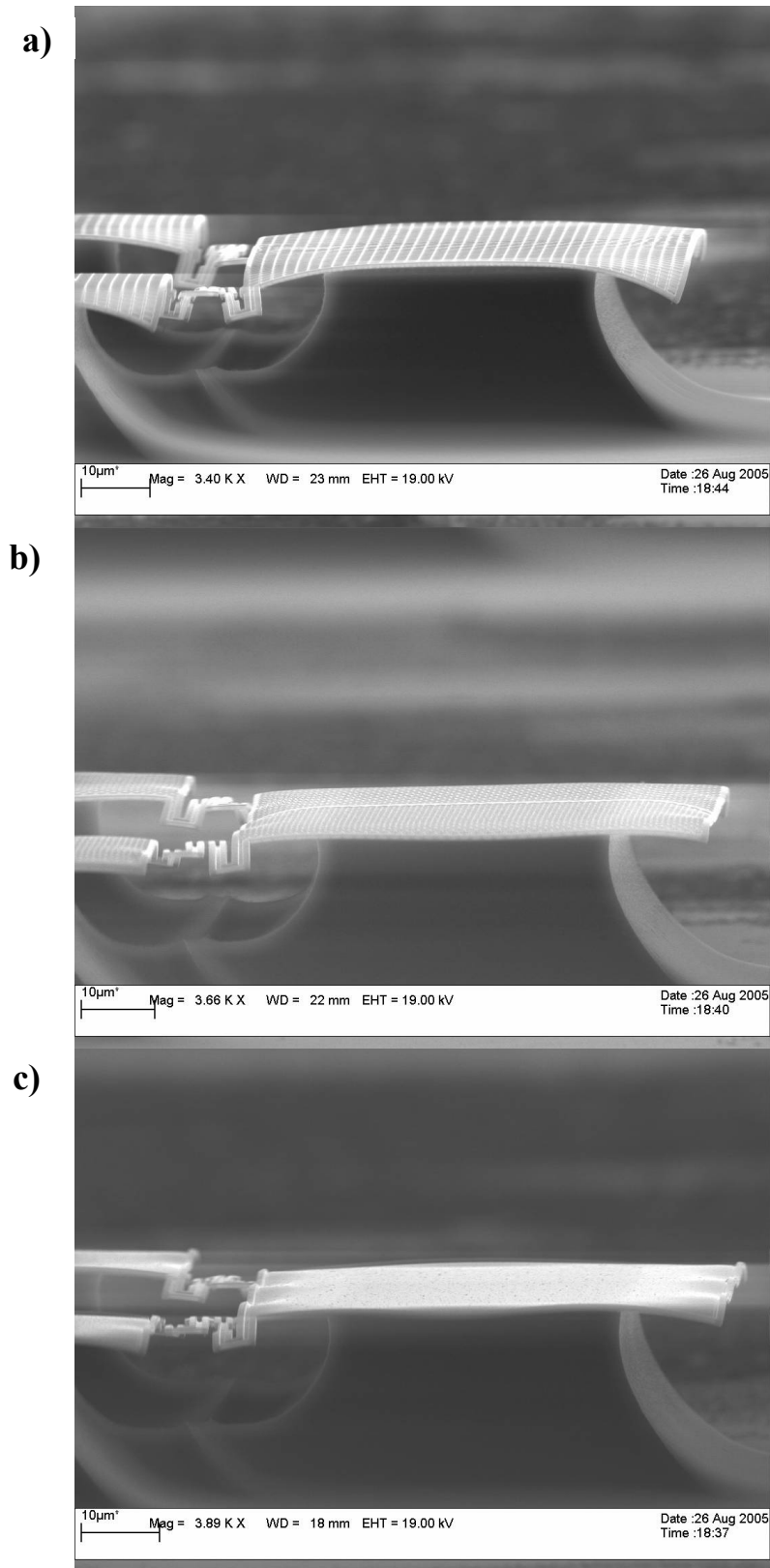

Figure 4.33: Rectangular (a), hexagonal (b), and flat pattern (c) anchors edge behavior at large under-etch

A hexagonal pattern was found to produce more horizontal anchor edges than a rectangular pattern, but at large under-etch the edge was found to be wrinkled when observed from a low-angle, and the corners - bent. The hexagonal pattern may prevent the layer from curving downwards after release, but the released portions of the layer expand sideways after release while the non-released portions of the anchor are still constrained. In other words, while the released portions of the anchor (the edge) assume their true "stress-free" length, the non-released center that is still attached to the silicon base is still compressively strained by the thermal mismatch at the deposition stage, which results in a curved anchor edge, and bent corners. No solid structural shape could possibly overcome this, so another anchoring mechanism was introduced.

4.2.7 Striped anchors and suspended coiled or meandering devices

The edge of the anchors was "striped"; narrow slits were introduced at regular distance along the edge. Anisotropic reactive ion etching of silicon was found to under-etch the anchors from the edge, but very little through the narrow slits, so the slits effectively relieved the strain mismatch at the anchor edge after under-etching, but the suspended structures' attachment points were not under-etched through them.

At this point we also standardized the process and mask parameters as follows:

-We used 1 μm wide beams and 250nm separation trenches throughout the subsequent research. On a mask level this translates to using just two line widths – 1 μm and 250 nm.

-We standardized the separation between the linewidths to 250 nm.

-The four subsequent metal depositions were plain aluminum sputtered layers each 50 nm thick in the direction of deposition. Up to 120 nm thick metal layers were found to produce equally good devices using the same mask patterns. This allows for finer control of gaps/parallel beams spacing.

-Timed plasma ashing was done using oxygen plasma at 300 scm flow rate and 400W power, for 15 minutes.

-Plasma ashing removal of the remaining resist after peel-off was performed using the same recipe for 60 mins.

Several suspended structural shapes were fabricated using this method of attachment, and were all found to be well aligned, and flat with respect to the substrate (Figure 4.34, 4.35, 4.36). Figure 4.37 gives a mask example used in the fabrication of the above structures.

Suspended structure are subject to the same expansion (due to internal stresses) after release as the expansion affecting the anchor edges after release. All of the above mentioned structures are meandering/twisted structures – flat coils and springs that are well capable of accommodating expansion after release, which aids shape preservation.
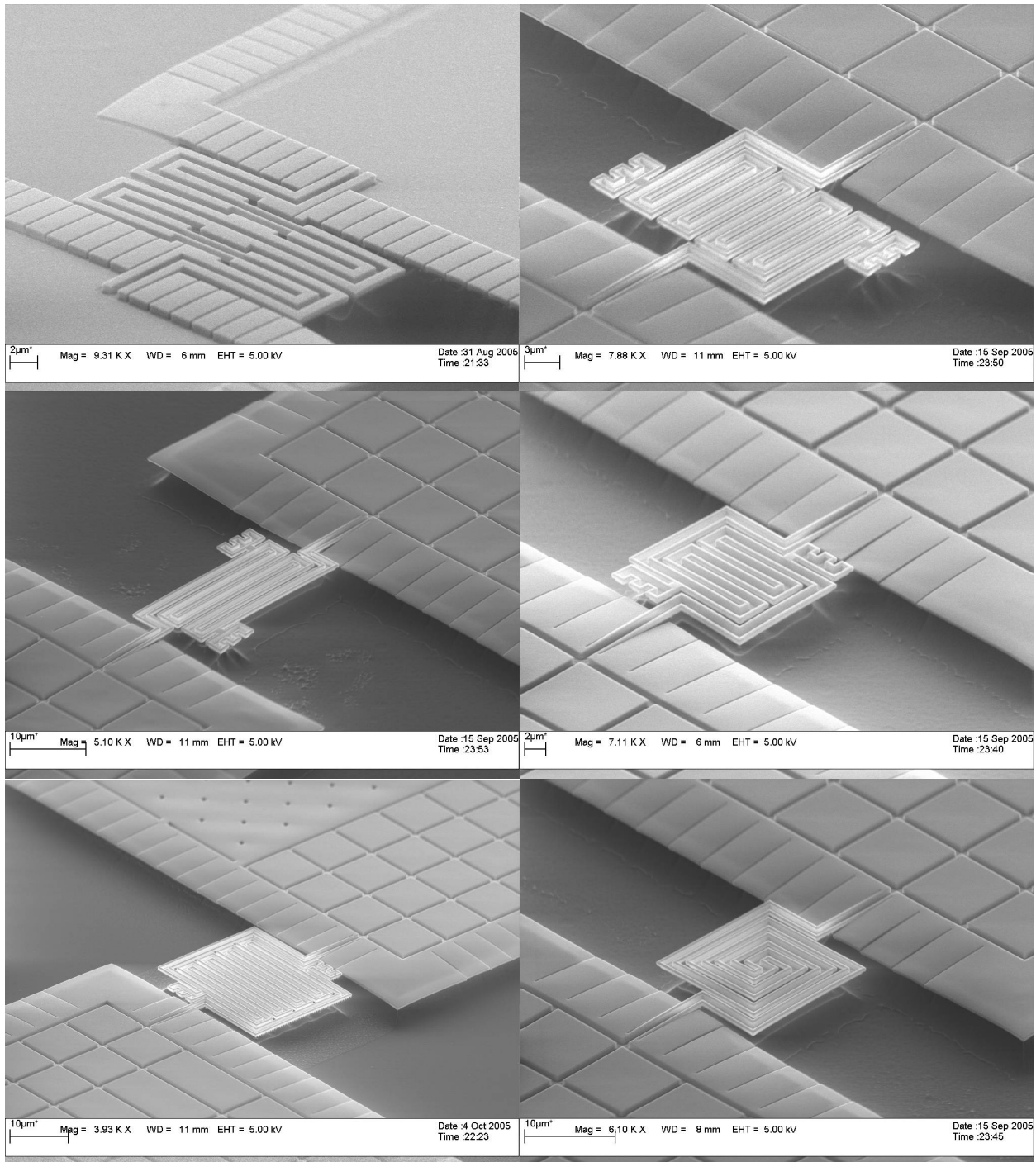
*Figure 4.34: Suspended structures with striped anchors*
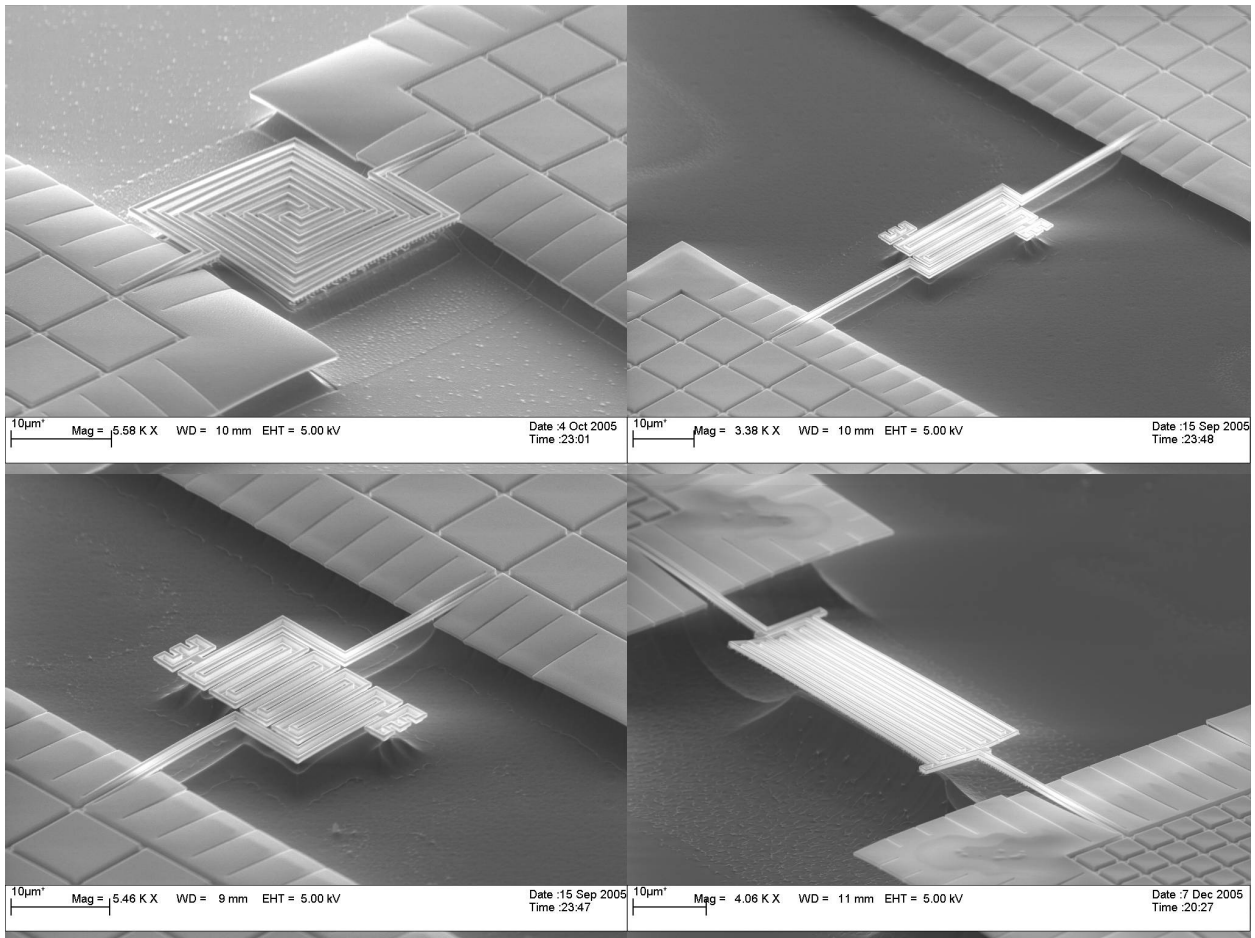
*Figure 4.35: Suspended structures with striped anchors*
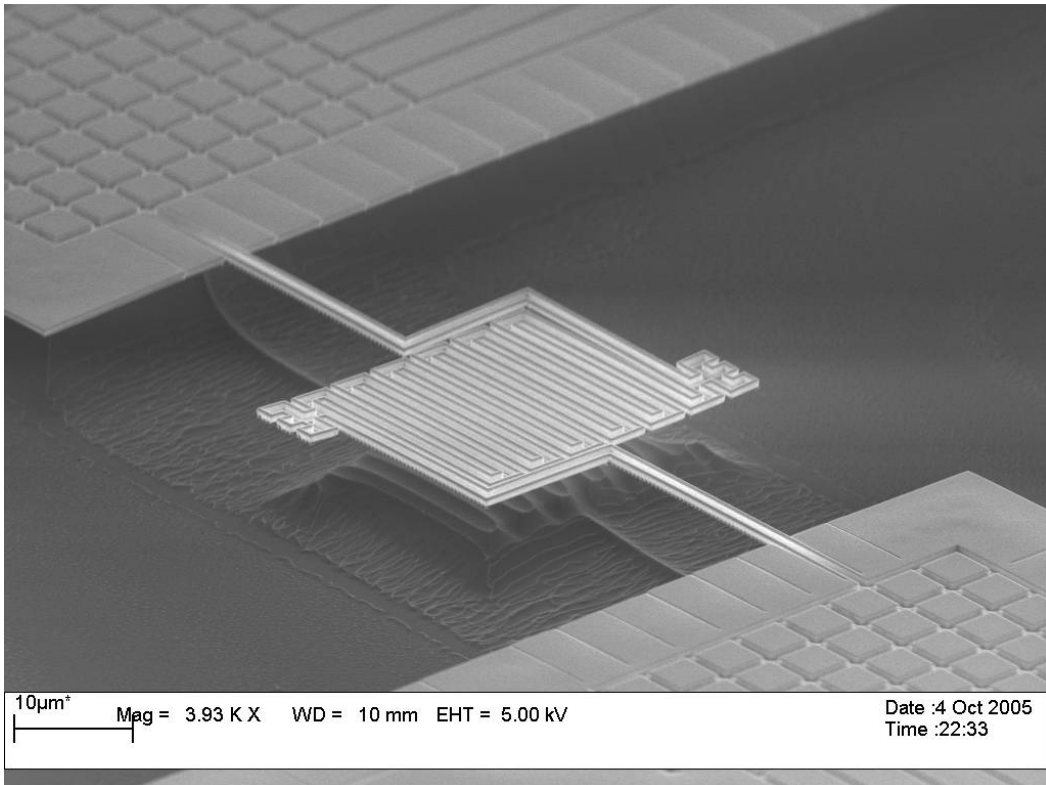
Figure 4.36: Large number of parallel segments suspended structure
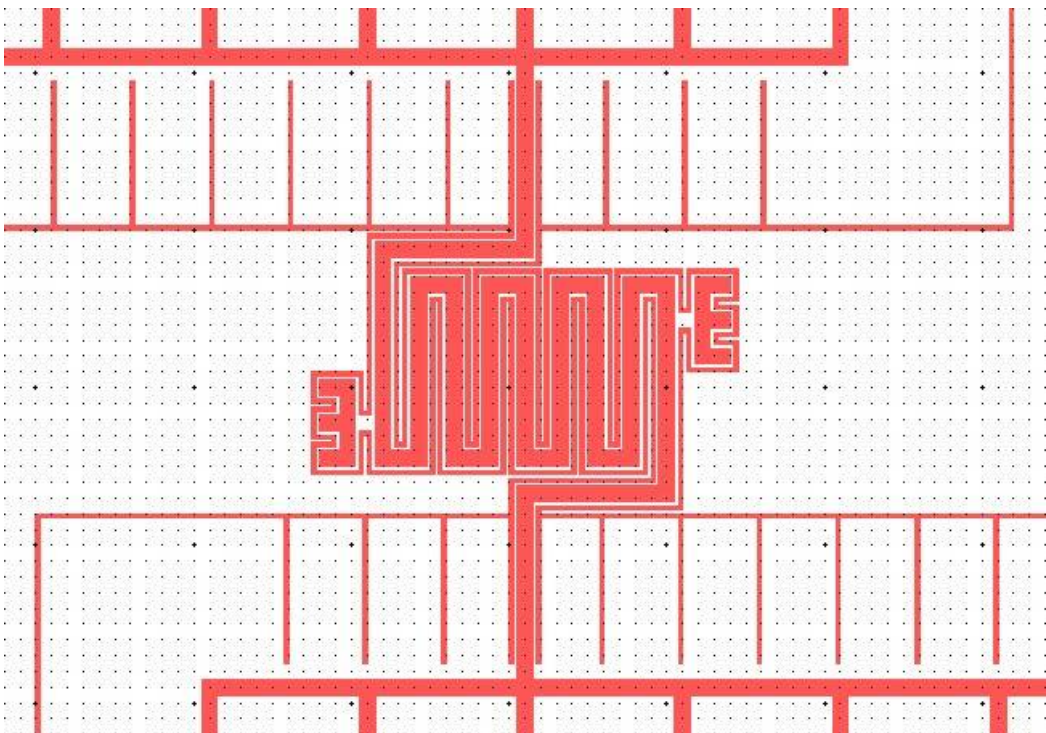
Figure 4.37: Striped anchoring grill structure mask example. Grid pattern is set to 1 μm

4.2.8 Bridge structures and stress inversion mechanism

Straight cantilever beam structures are important from a MEMS stand point of view as they are very useful for mass sensing by resonant actuation and detection, as well as RF MEMS filters. We fabricated two bridge structures parallel and next to each other – one straight conventional cantilever bridge and another inverted-"T" suspended bridge structure for reference (Figure 4.38). The reference structure has a twist at its center and a gap, which allows to accommodate compressive stress to some extent and remain relatively parallel to the substrate.

The two beams alignment was inspected and, the straight bridge cantilever beam were found to have buckled upwards after release, in relation to the inverted-T beam. (Figure 4.39).
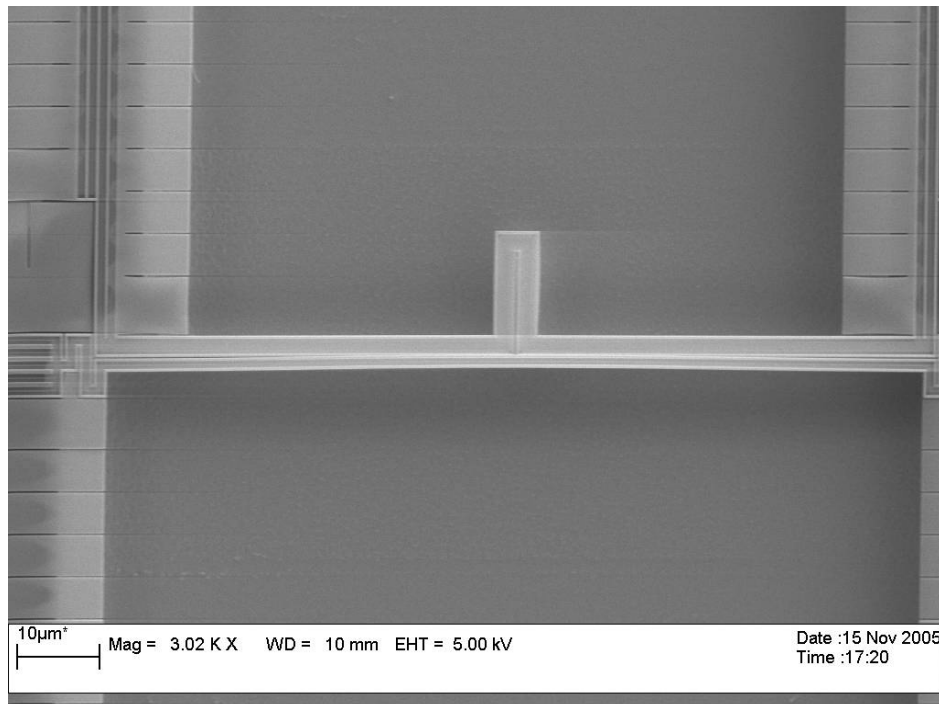

*Figure 4.38: Cantilever bridge parallel to a reference structure*
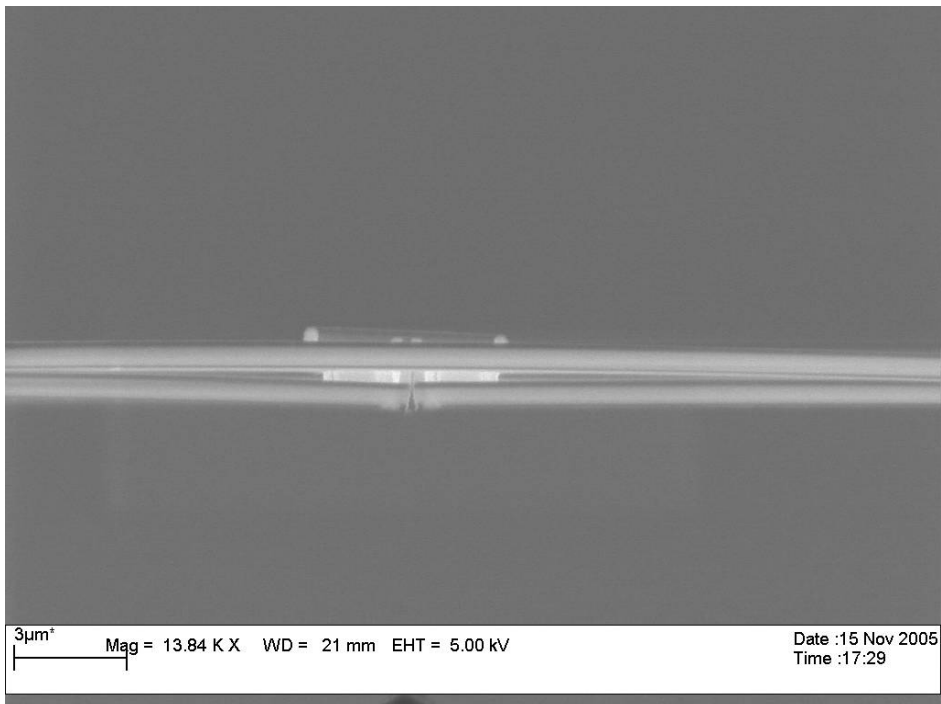
Figure 4.39: Center of the cantilever bridge and reference structures viewed at an angle parallel to the substrate. The bridge is buckling upwards

The buckling of straight bridge structures suggested the solution to the problem itself. If the center point of a beam buckles after release, than this displacement can be used to stretch a beam suspended between the center points of two beams buckling outwards, i.e. a structure that has an "H" shape observed from above. The direction of buckling can be controlled by using beams that are angled at their center, in the direction of intended buckling [43]

Figure 4.40 illustrates this novel stress-inversion mechanism. When compressive stress inside the structures is translated into elongation after release, a beam that is suspended between the center points of two outwards moving buckle-beams, elongates less sideways than the center point displacements of the buckle beams. This stretches the center beam sideways, and converts compressive stress into tensile stress.
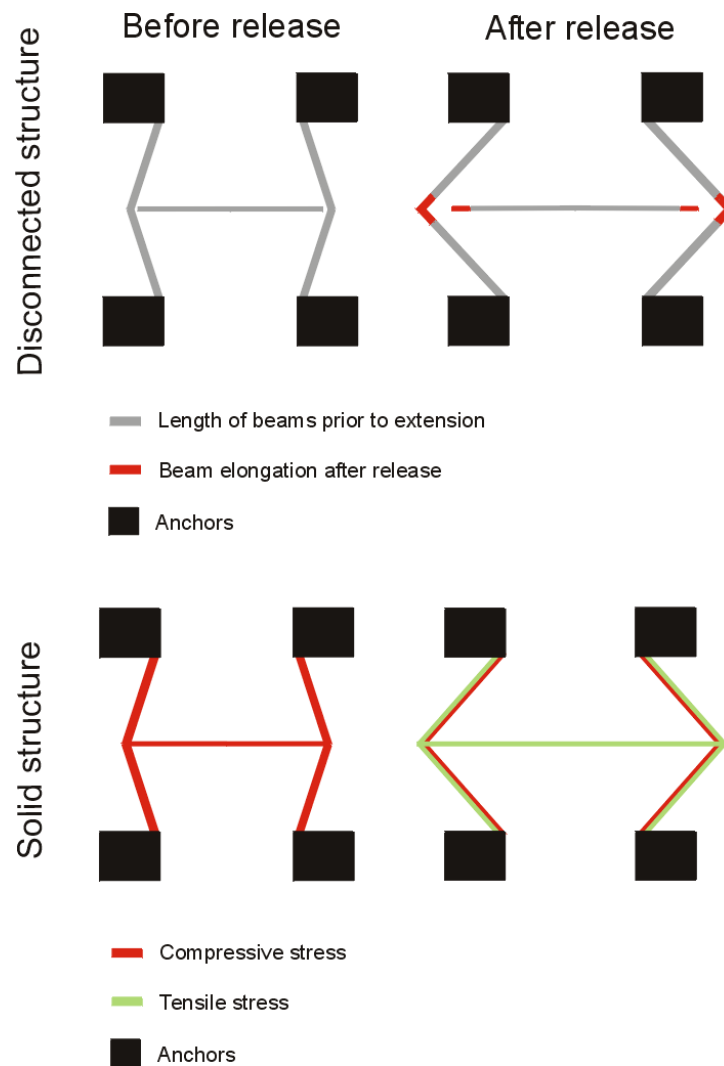
Figure 4.40: Stress inversion mechanism

This mechanism was investigated parametrically by fabricating several variations of such outwards stretching buckle-beam structures. Different buckle angles, buckle beam lengths, number of beams and beam grouping/spacing were tried. Figure 4.41 gives examples of the structures that were tried, and Figure 4.42 illustrates the parameters that were varied (h and L), and the parameters kept constant. Three horizontal offsets (h) were tried – 2, 4, and 6 μm, and segments lengths were 20, 30 and 40 μm, i.e. we fabricated nine permutations of each suspension mechanism type (4-beam, 8-beam and Double 4-beam)

The parametric investigation showed that small angle (α) buckle beam groups, that are tightly packed together were not successful.

One structure type was found to perform its intended task best. In consists of two groups of four parallel buckle-beams that have a large buckle-beam angle and are connected by a straight beam at their central axis. This structure is different than the rest as it is more resilient to twisting in the vertical plane, having four attachment points to the anchors (Figure 4.43).

The beam suspended between two such devices was found to be perfectly straight and aligned with the the reference area parallel to it (Figure 4.44, 4.45)
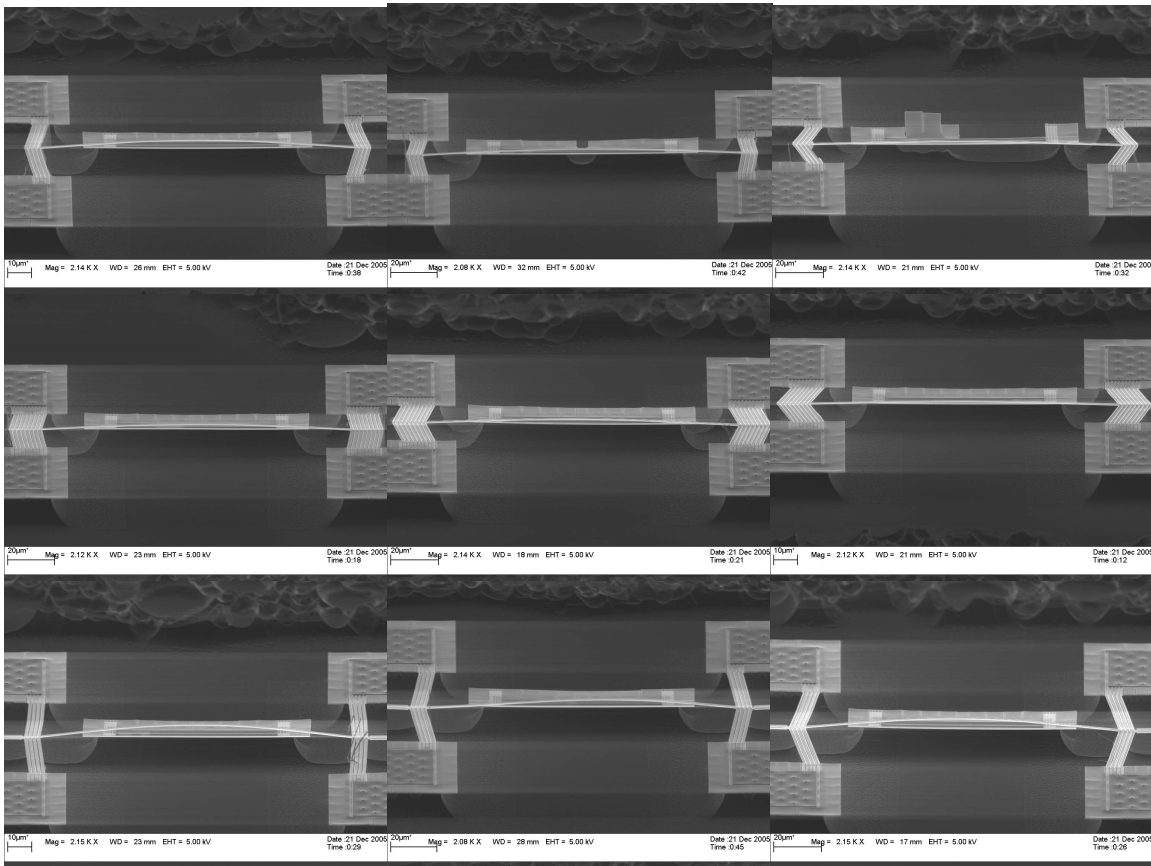
*Figure 4.41: Buckle beam structures examples, from parametric study*
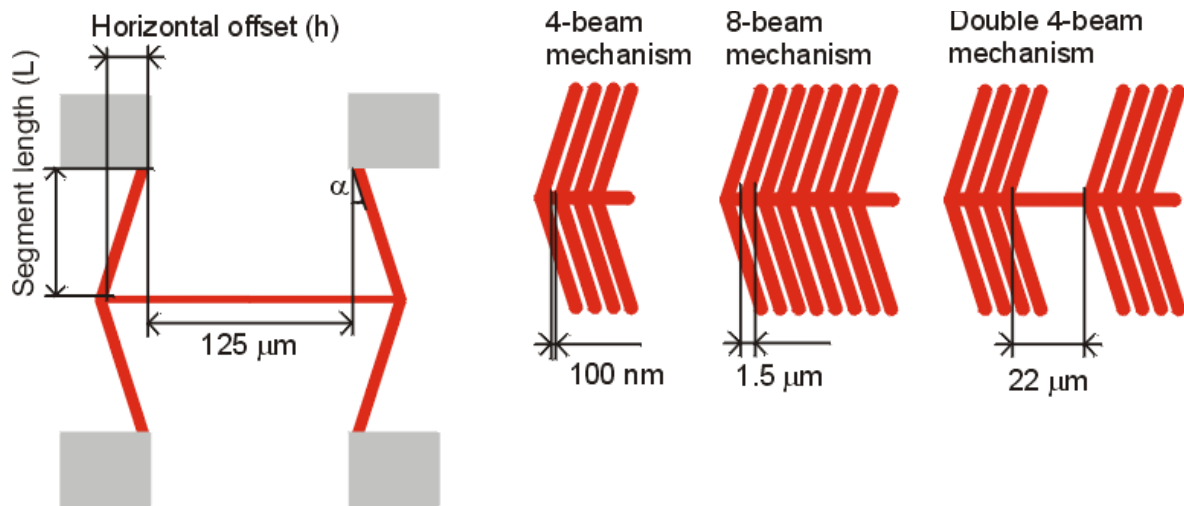
Figure 4.42: Buckle-beam suspension mechanism parameters and definitions
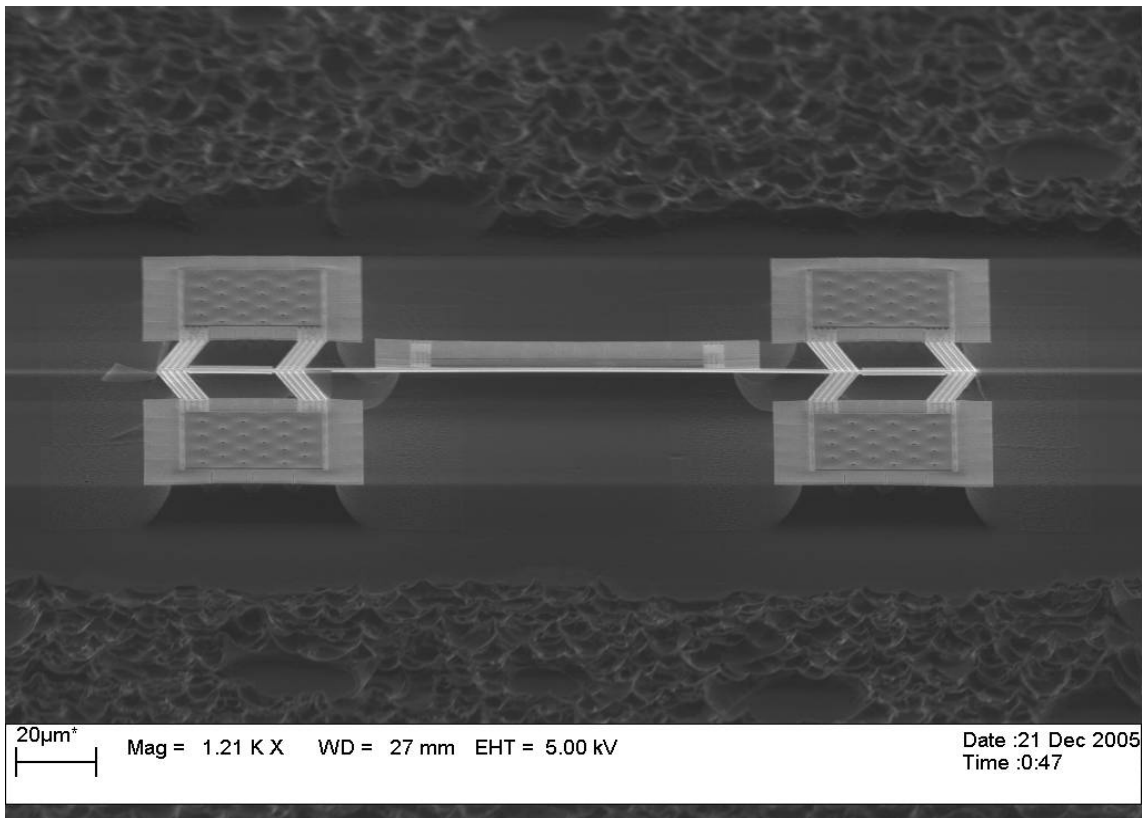
*Figure 4.43: Successful buckle beam devices stress-inversion*
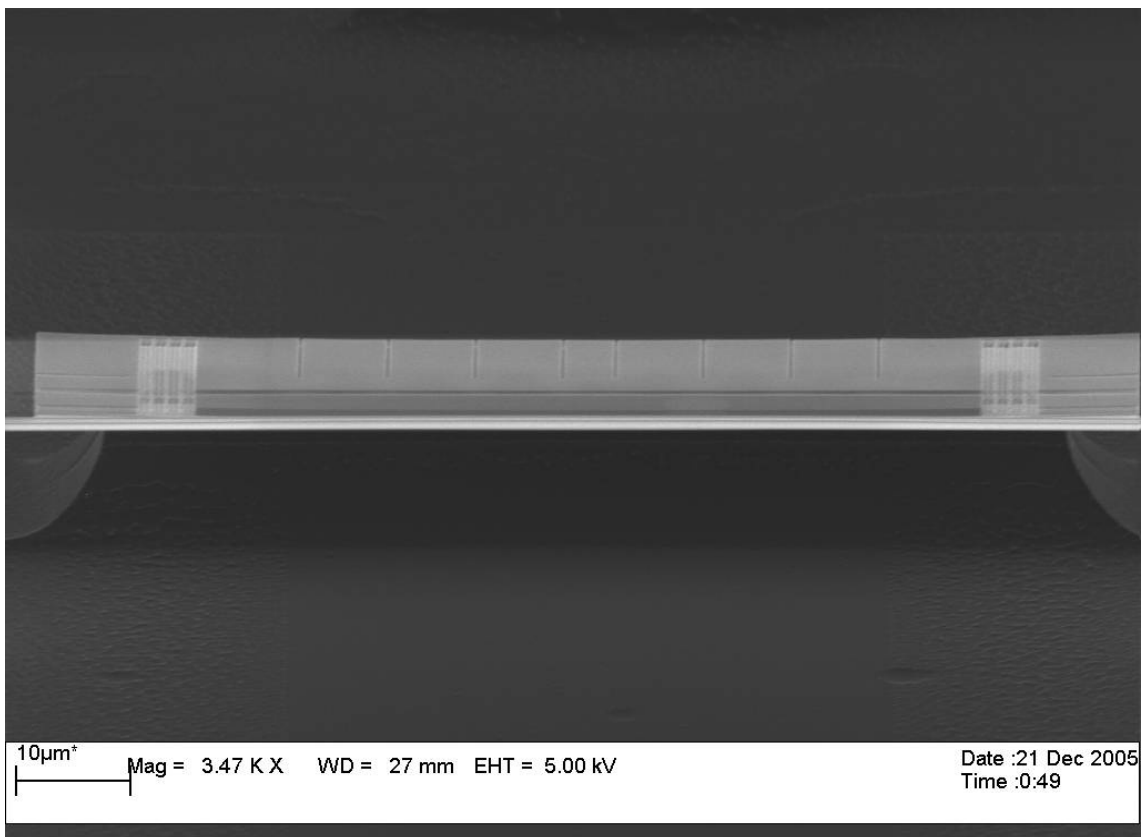
Figure 4.44: Close-up view of suspended straight bridge and reference area, showing perfect alignment and no buckling in the vertical plane
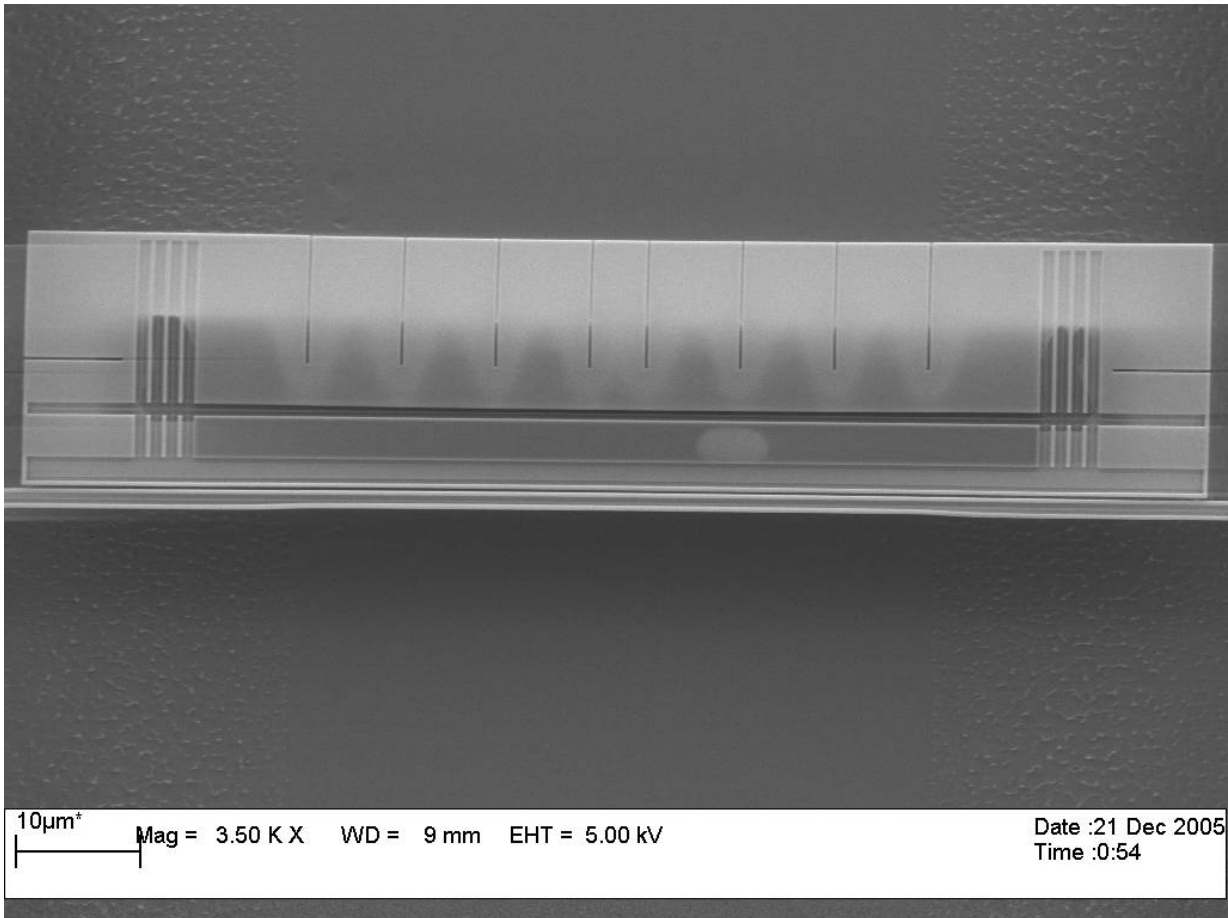
Figure 4.45: Top view of reference and cantilever bridge showing perfect alignment and no buckling in the horizontal plane

The parameters for this structure are 20 μm segment length, 6 μm horizontal offset, double 4-beam type. Buckle-beam angle (α) is 17 deg. We used this structure in all subsequent research into bridge cantilevers beams, either as is, or by scaling it. Scaling was done by maintaining α and beam widths, and proportionately increasing beam lengths (bridge, buckle-beam segments and beam connecting buckle-beam groups).

We believe that this is not necessarily the only possible mechanism; any grouping or number of buckle beams along a central connecting beam that is long enough would probably work; we chose to group the buckle-beams at both ends of the connecting beam for ease of fabrication and high yield – this arrangement results in just two top metal layer rectangles in between the device segments, that need to be peeled-off.
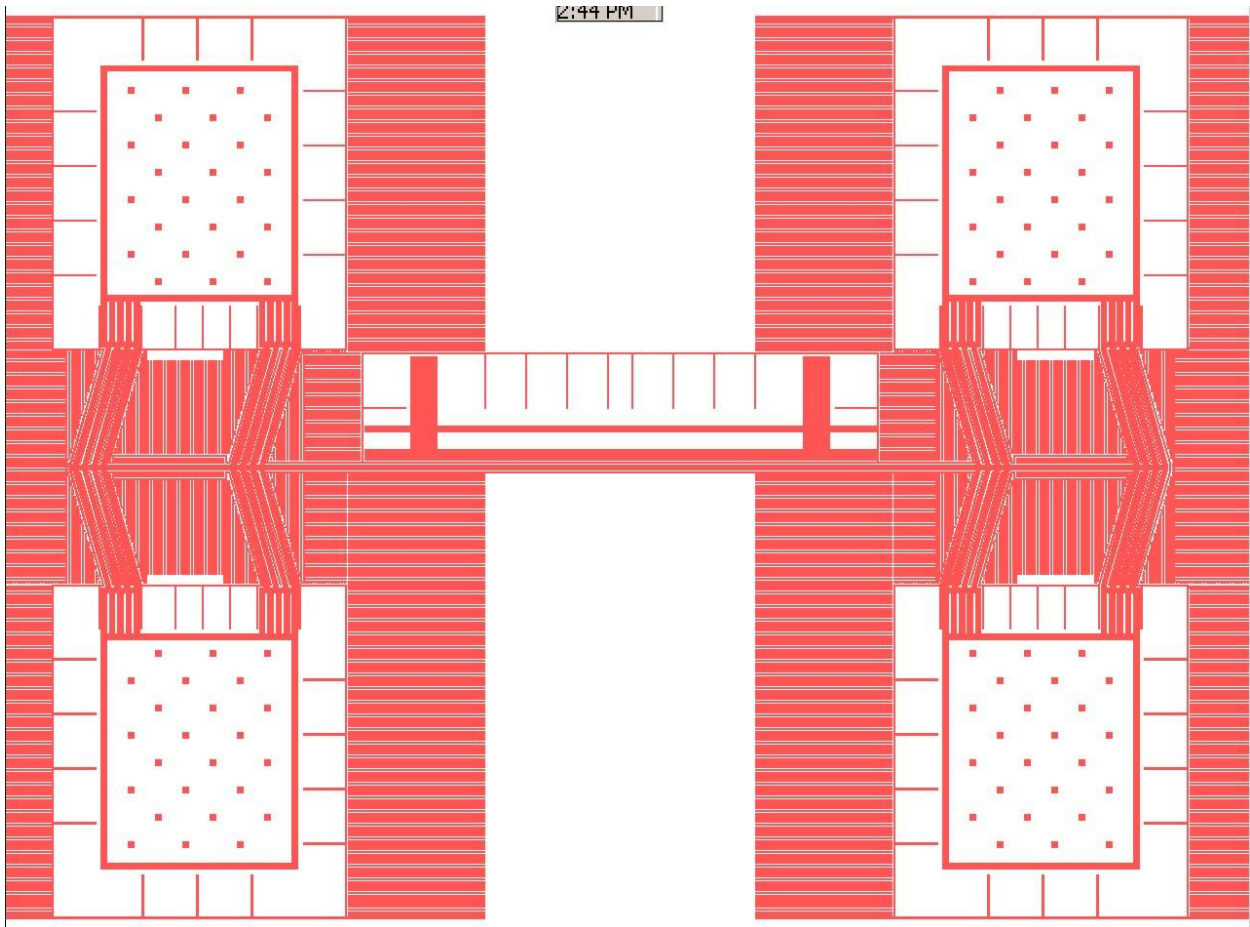
Figure 4.46: Successful buckle-beam anchoring arrangement mask

4.2.9 Yield and E-beam writing time

Yield for the new peel-off fabrication method was in the order of 20-50%. Peeling a top metal layer is by definition an isotropic process, as it has directionality with respect to the pattern. This leads to ripping-off the layer at stress-points such as corners, the remainder still attached to the resist layer after the peel-off. To solve this, such areas were striped with an alternating pattern of narrow 250nm lines 250nm away from each other. This served to under-etch those areas during the plasma-ashing step, and release them prior to peel-off. This solution raised the yield to 100%.

Figures 4.56 and 4.57 provide a good illustration of this approach.

Writing solid patterns on the anchor plates was by far the greatest cause of high e-beam writing time. In order to drive the cost down a dot pattern was introduced on the anchoring plates. This reduced the cost and writing time ten fold, while still producing anchoring plates large enough for wire-bonding. This approach also eliminated the need for introducing a UV lithography step, in order to fabricate large flat areas (anchors and bonding pads).

Both of these cost-reduction approaches can be seen on Figure 4.46, and all subsequent mask examples.

4.2.10 Rectangular cross-section structures

Fabrication of rectangular cross-section structures were also attempted by the introduction of an

extra resist spinning, plasma-ashing and metal deposition steps. AZ resist was spun on top of the chips after metal deposition. This layer was then plasma-ashed in an attempt to reduce its thickness to below the level of the channels formed by the U-shaped cross-sectional structures (Figure 4.47). Controlling the uniformity and the thickness of the top resist layer proved to be difficult, and the yield extraordinarily low; the channels were filled with resist, as intended, but there was also a residual thin resist layer left between the primary and secondary metal layers which prevented successful peel-off. In other words, processing step 3 often failed to completely remove the secondary resist on top of the primary metal layer. Some structures were successfully fabricated, skipping the second metal layer deposition step (Figure 4.48, 4.49), which shows that the process is feasible and high yield obtainable, if more effort is invested into optimizing the process.


1) Angled deposition of metal layer
2) Secondary resist layer spin
3) Timed plasma ashing of secondary resist layer
4) Secondary metal layer angled deposition
5) Timed plasma ashing of primary resist layer

6) Top metal layer peel-off
7) Plasma ashing removal of primary resist layer
8) Secondary resist layer dissolved in acetone
9) Suspended structures release by anisotropic RIE

Sputtered metal
Polymer resist 1
Polymer resist 2
Silicon substrate

Figure 4.47: Rectangular cross-section hollow structures fabrication process sequence

10µm*   Mag = 5.10 K X   WD = 15 mm   EHT = 5.00 kV   Date :10 Oct 2005
                                                                                    Time :19:17
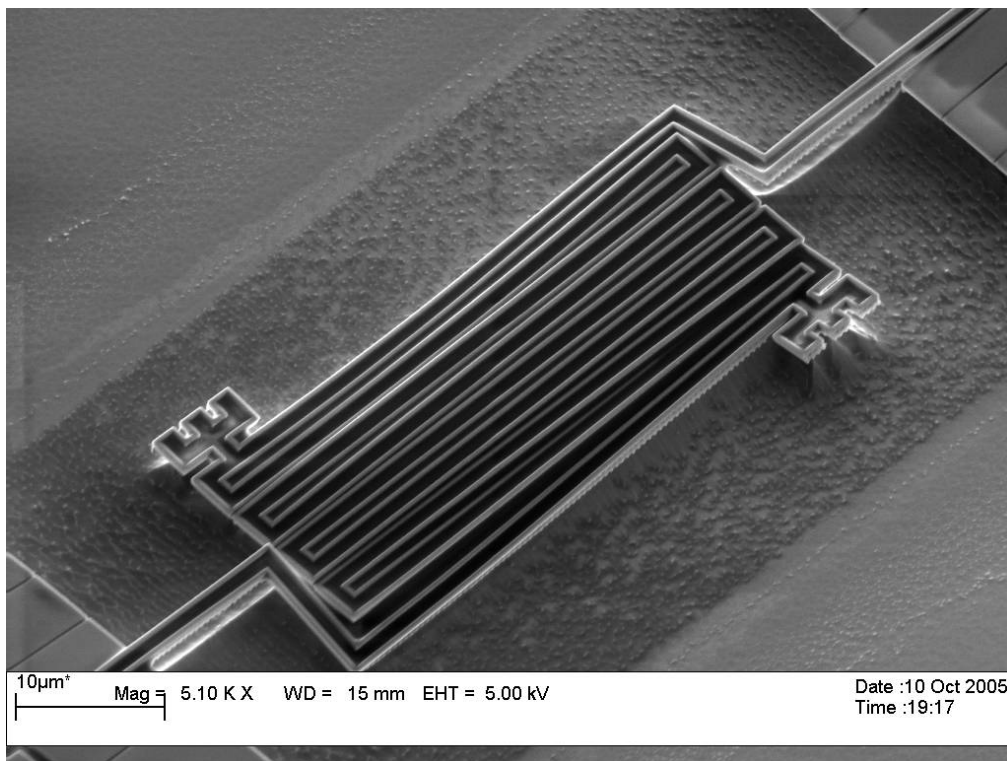
Figure 4.48: Suspended channel structures filled with polymer photo-resist

```
2µm*        Mag = 24.87 K X    WD = 15 mm  EHT = 5.00 kV              Date :10 Oct 2005
                                                                      Time :19:21
```
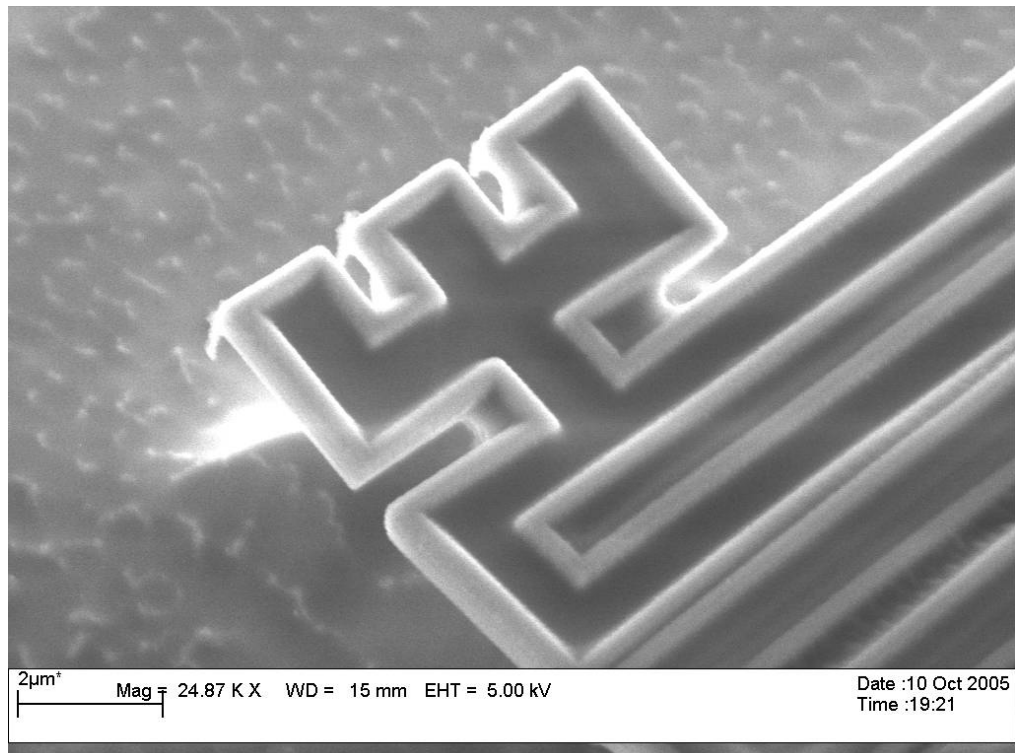
Figure 4.49: Suspended channel structures filled with polymer photo-resist close-up

4.2.11 Experimentation

Capillary action flow

Liquid flow along the channels formed by U-shaped cross-sectional structures was successfully performed using capillary action.

This was done by connecting the channels formed by the suspended structures to channels on the anchors. These were extended across and outside the anchors to a reservoir where a drop of liquid was spotted using a syringe.

Figures 4.50, 4.51 and 4.52 show the general anchors and reservoir arrangement that we designed and fabricated. One can also see the channels across the anchors and their starting points in the reservoir, on Figure 4.53.
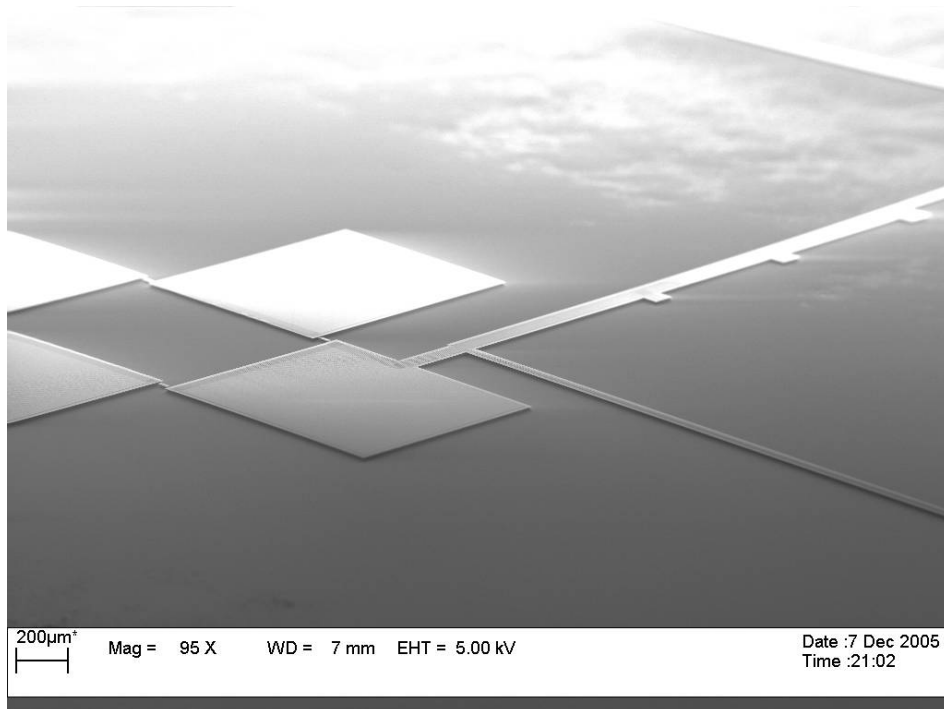
Figure 4.50: Anchors (large flat areas) and reservoir (large fenced area) overview. The suspended channel devices are barely visible between the anchors
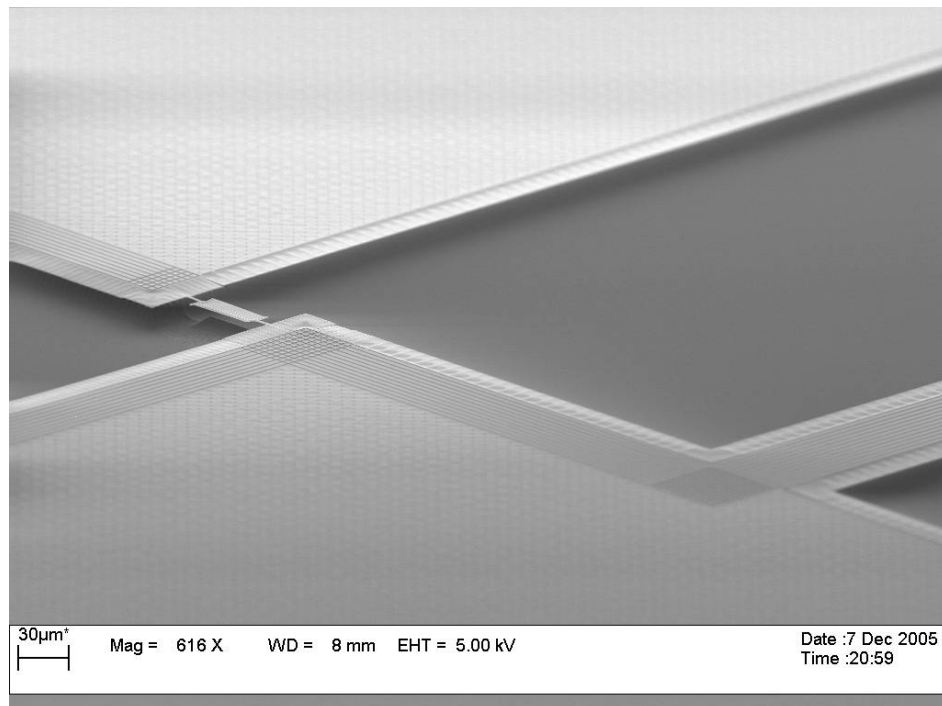

Figure 4.51: Suspended channel device and channels along the anchor edge. Dot pattern in anchors is also visible
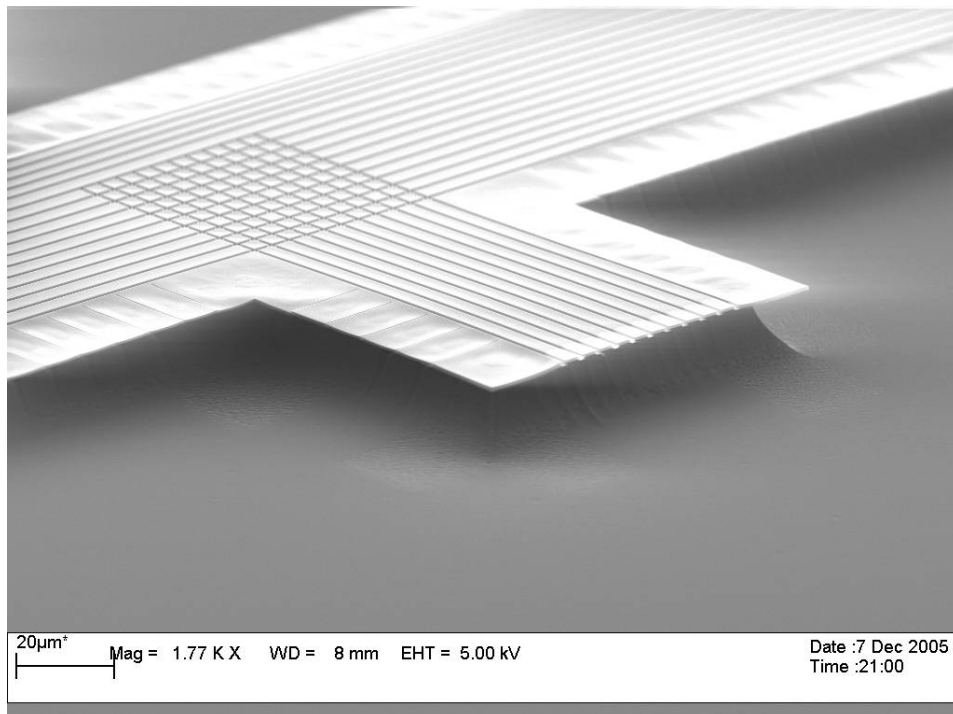
Figure 4.52: Channels starting point (in reservoir) close-up.

Acetone, Isopropanol, DI water and Glycerin were all experimented with; all were found to flow along the channels after spotting; Acetone, Isopropropanol and DI Water flow extremely fast along those channels and took approx 30-60 sec to fill all the channels and "circumnavigate" the whole device, glycerin flow speed was very slow in comparison, approx. 10 µm/s.

Figures 4.53, 4.54, 4.55, 4.56 and 4.57 show the mask (and important mask details close-ups) used to fabricate the described micro and nano structures.
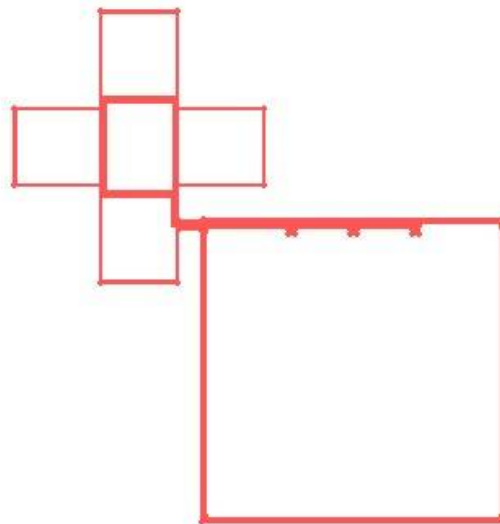
Figure 4.53: Reservoir, channels and anchors mask overview
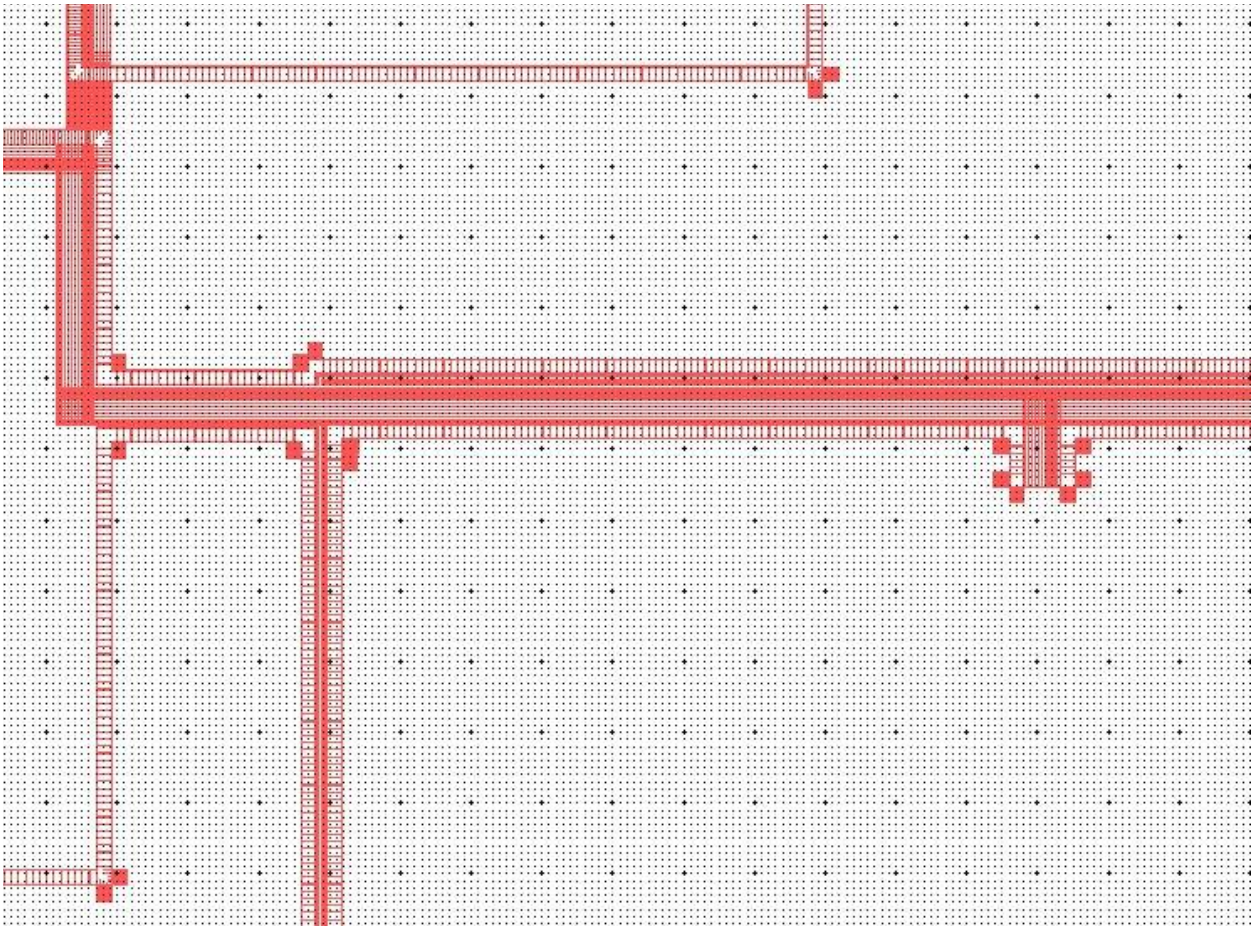
Figure 4.54: Reservoir to anchor connection and channels mask close-up. Grid pattern is set to 1 μm
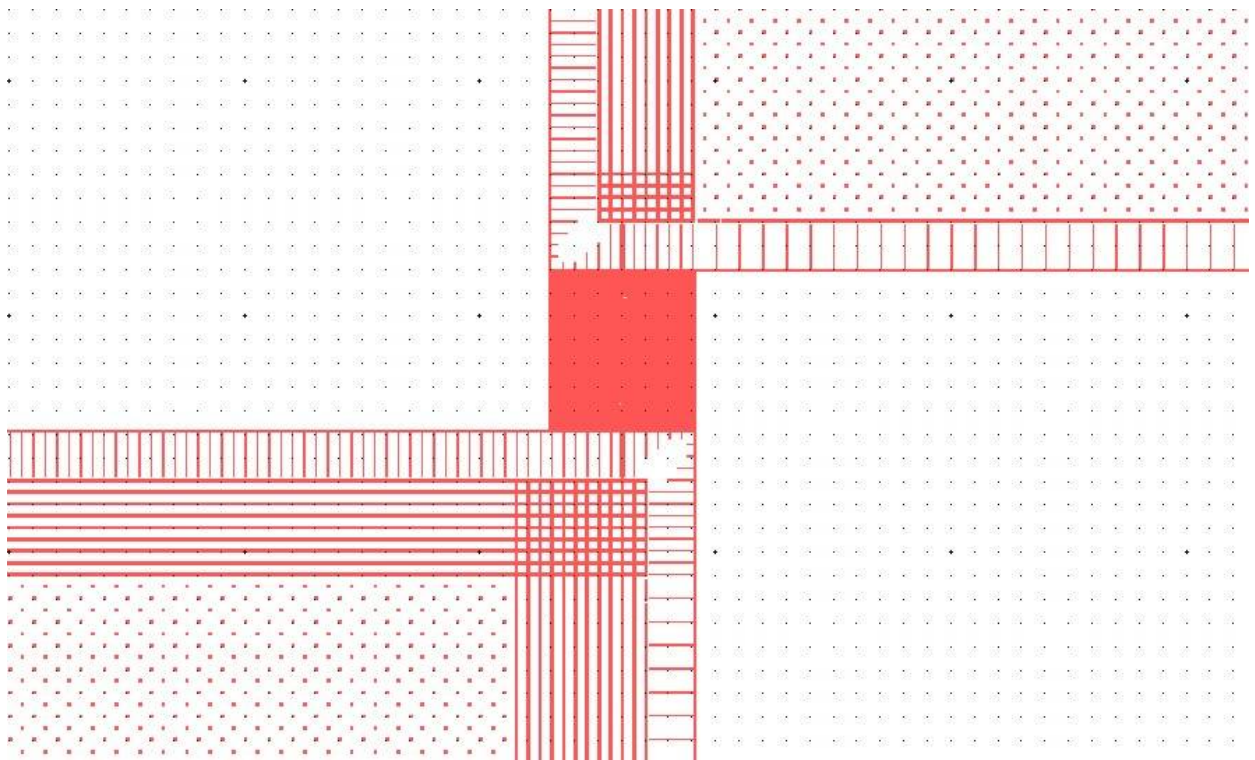

Figure 4.55: Channels to device connection mask close-up. Grid pattern is set to 1 μm
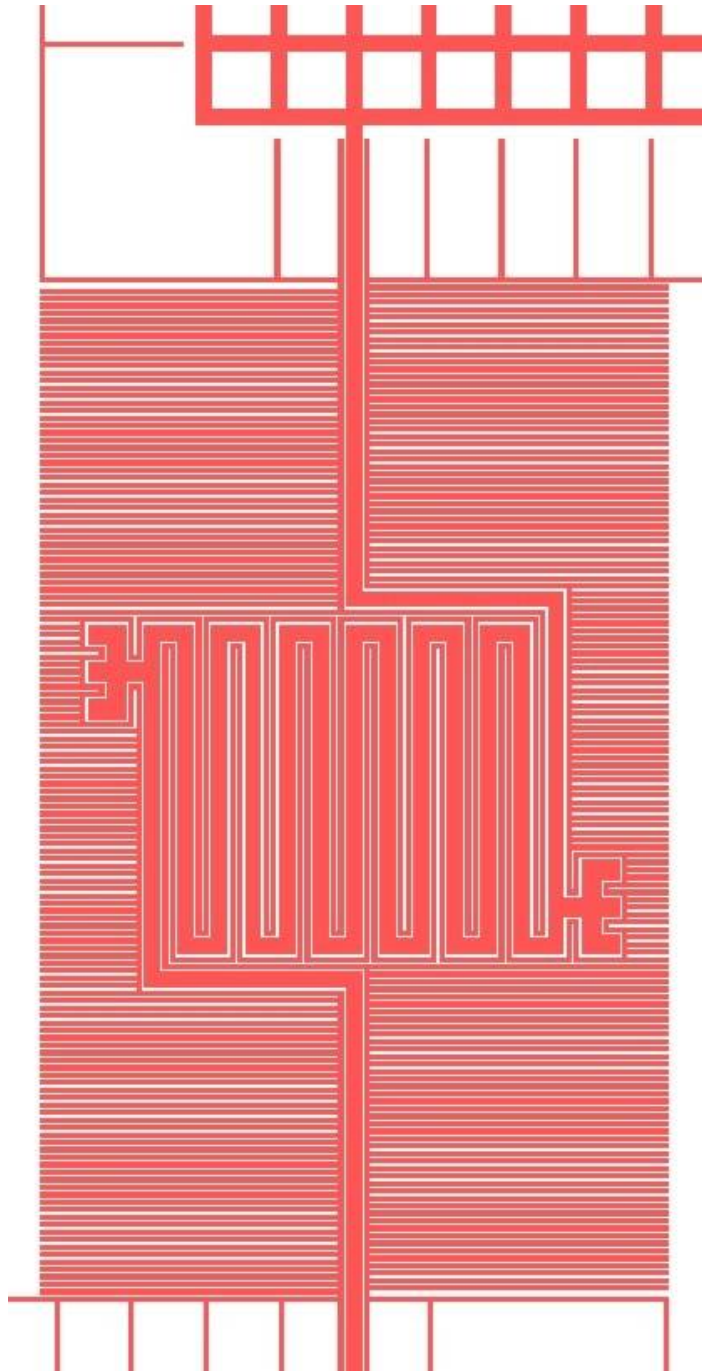
Figure 4.56: Suspended channel device mask close-up. Major linewidth is 1 µm (thick lines), minor linewidth is 250 nm (thin lines)
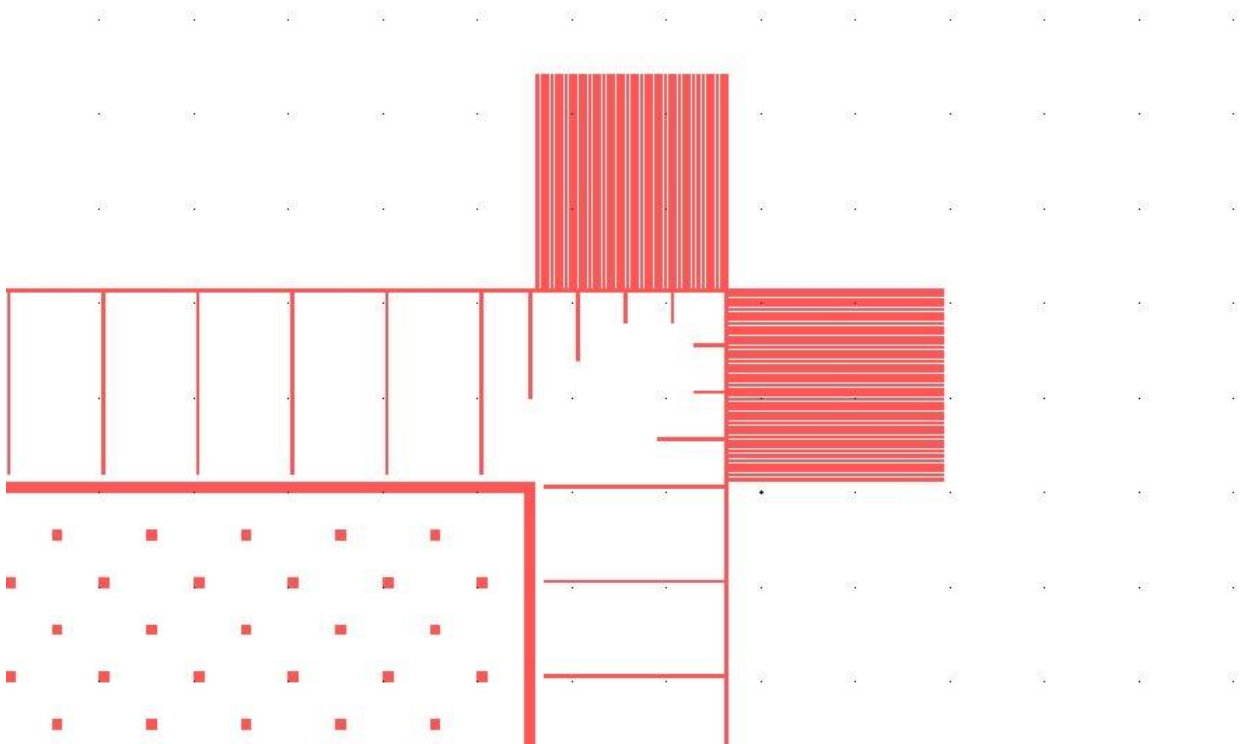
Figure 4.57: Anchor corners close-up at the mask level. Striped pattern serves to prevent top layer from ripping apart during peel-off and raise process yield

Electrical measurements

This opens the possibility for resonant cantilever mass sensing, where a resonant bridge device is used to measure the density of the liquid inside it, or the mass of a solid residue after liquid evaporation from an open channel.

The resonant frequency of a metallic U-cross-section shaped beam is also considerably higher than that of conventional solid micro-fabricated beams of the same size and mass, as it has a high second moment of area, and very low mass [44]. This increases its mass sensitivity by an order of magnitude compared to conventional beams of the same size. As an added bonus, aluminum has a high electrical conductivity and can support high current densities compared to silicon and polysilicon, which aids resonant actuation and detection by external magnetic fields. The electrical resistivity of aluminum (27 nΩm) is three orders of magnitude lower than the resistivity of the highly doped silicon (10000 nΩm), i.e. much larger fields can be generated by an aluminum conductor carrying current [45]. The buckle-beam suspension mechanism is also very useful for resonant mass sensing as it puts a straight bridge structure under tensile stress, thus raising its elasticity (k), and so also raising its resonant frequency and mass sensitivity (1.6), (1.9).

Figures 4.58 and 4.59 show the device that we fabricated for the purpose of resonant mass-detection, and Figures 4.60, 4.61, 4.62 and 4.63 show details of the mask design that was used.
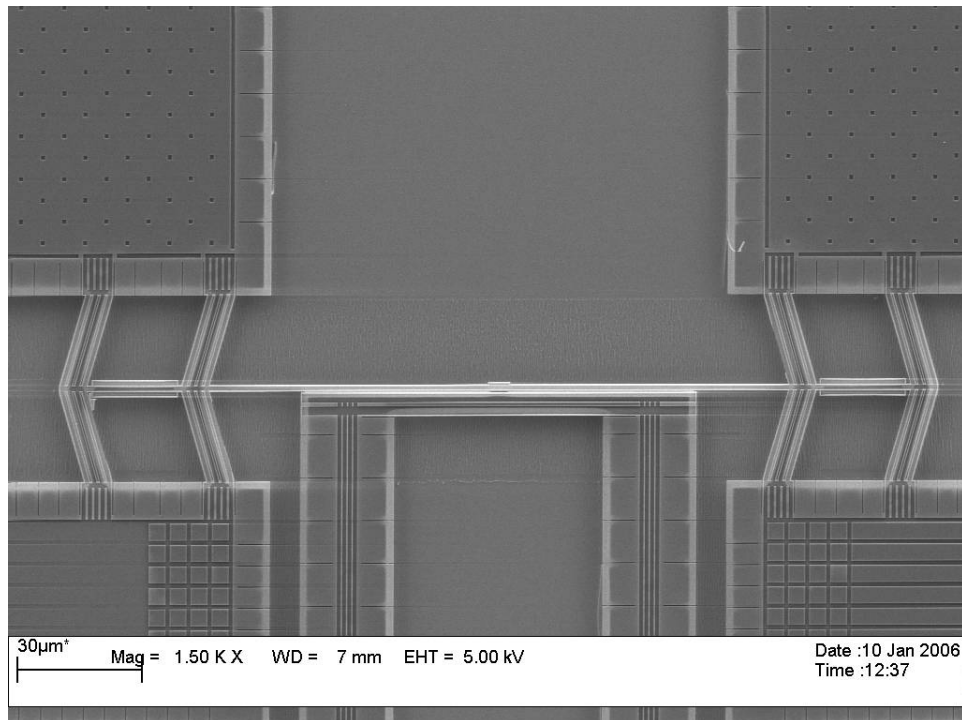
*Figure 4.58: Resonant bridge and electrode arrangement, top-view*
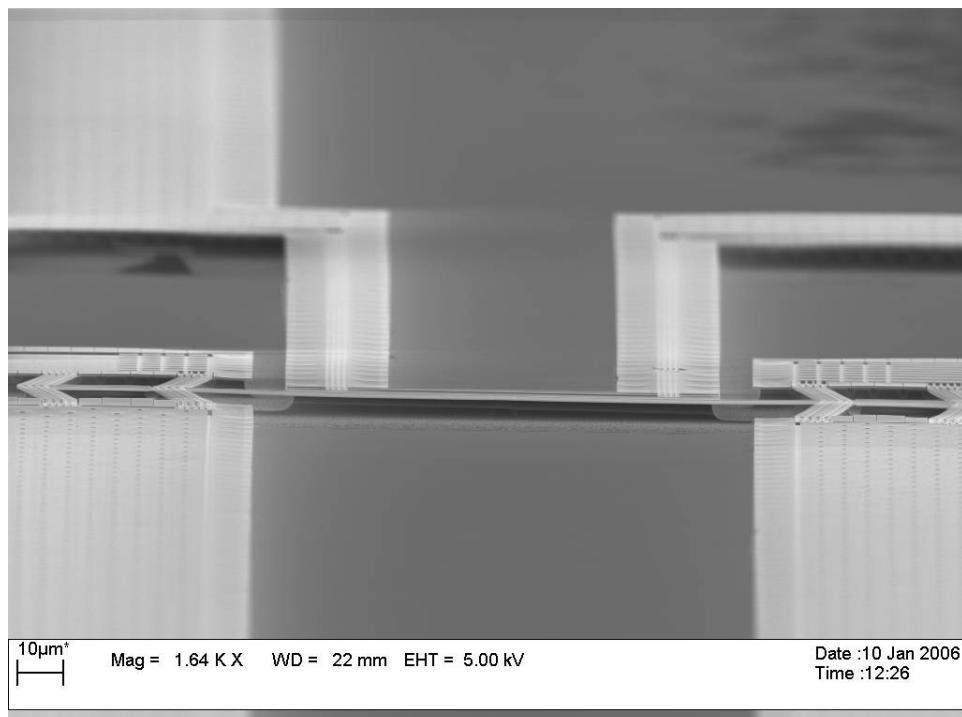
*Figure 4.59: Resonant bridge and electrode arrangement, low-angle view*
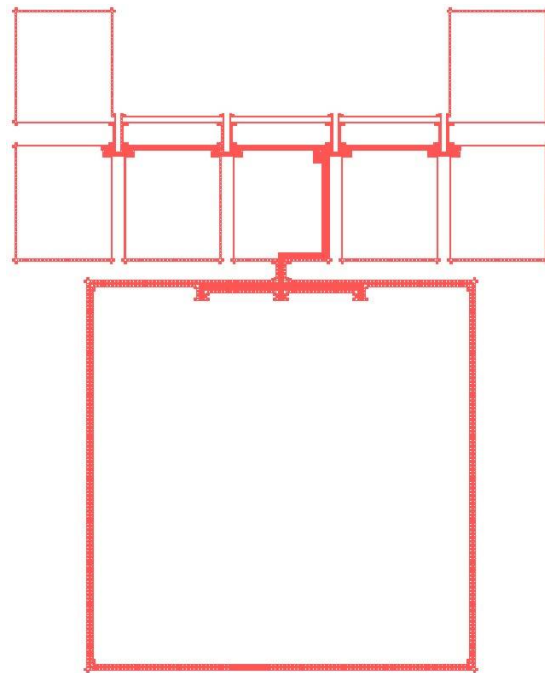
Figure 4.60: Resonant bridges and electrodes mask overview
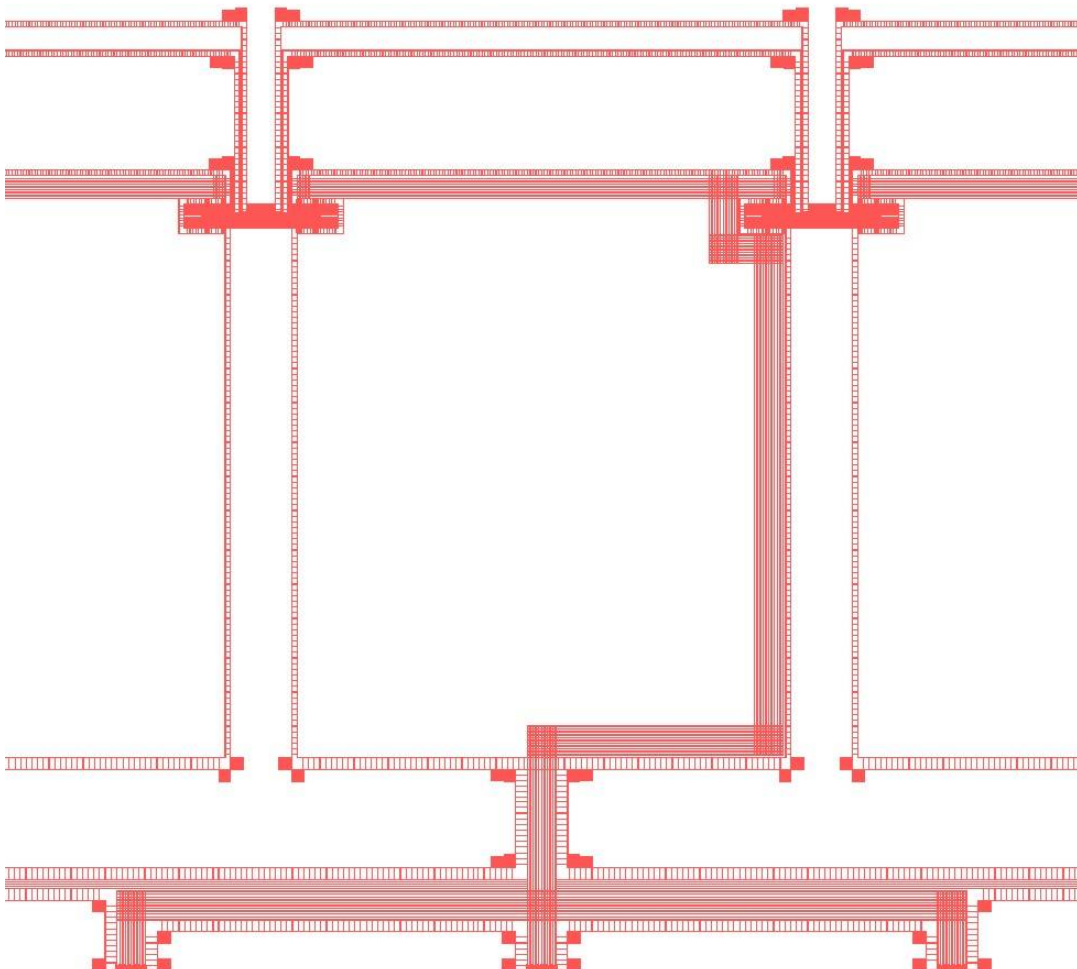
Figure 4.61: Resonant bridges and electrodes mask close-up; liquid channels overview
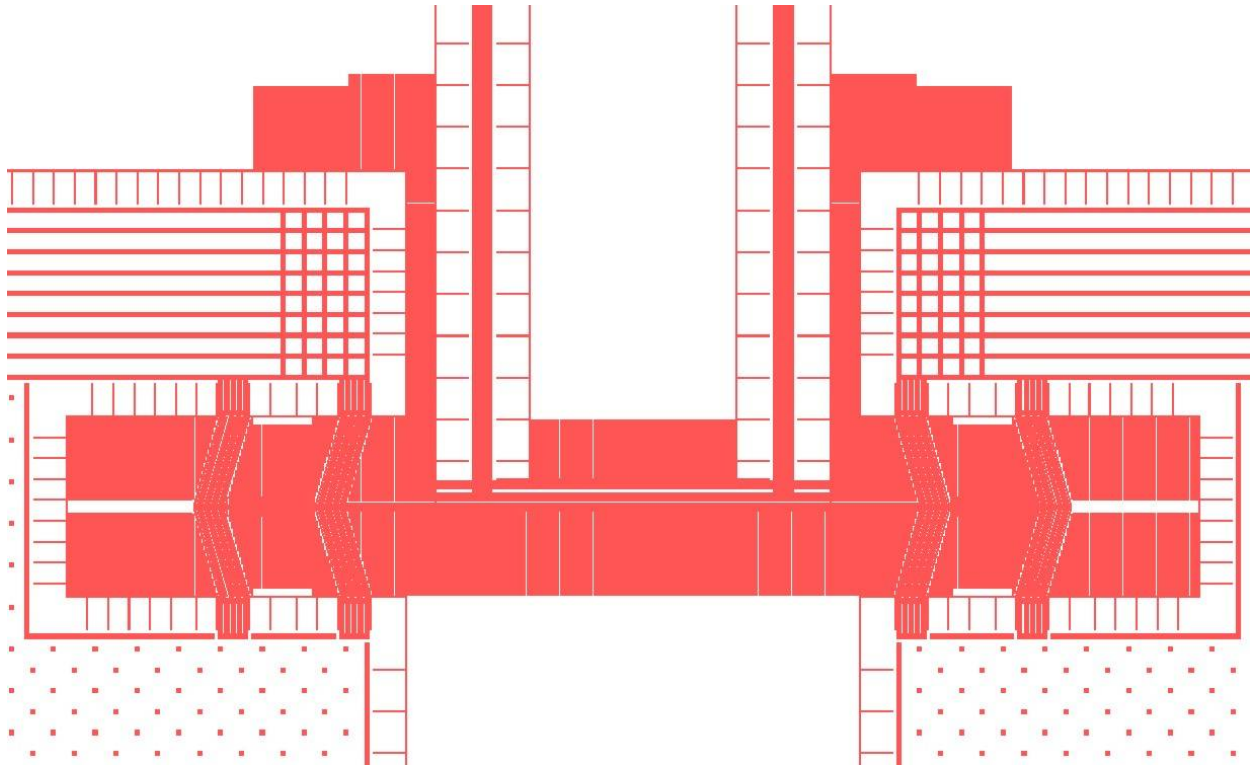
*Figure 4.62: Resonant bridge and electrode mask device close-up*
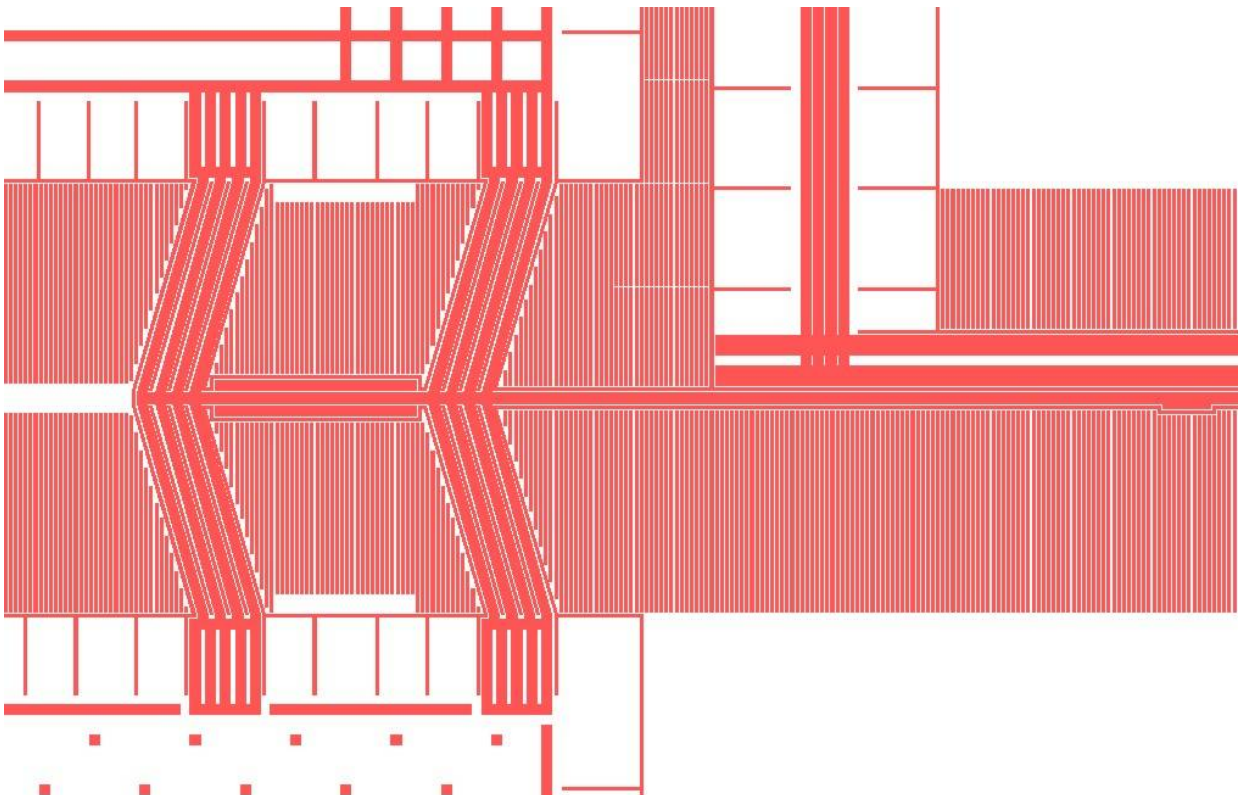
Figure 4.63: Buckle beam anchoring mask close-up

The resonant frequency (first harmonic) of a clamped-clamped bridge cantilever is [24]

$$f_{res} = \frac{1}{2\pi}\sqrt{\frac{k}{0.38m}} \qquad (4.1)$$

where m is the cantilever mass and k is the cantilever elastic constant (k=P/Δx) at its center point. The deflection Δx of a clamped-clamped cantilever beam's center point under a force P is PL^3/192EI [45], where L is the beam length, E is the beam material's Young's modulus and I is the second moment of area of the beam cross-section in the deflection axis. Therefore

$$f_{res} = \frac{1}{2\pi}\sqrt{\frac{192EI}{0.38\,A\rho L^4}} \qquad (4.2)$$

where A is the beam's cross-sectional area and ρ - the density of the beam material.

The second moment of area of the beam that we have fabricated can be calculated using the parallel-axis theorem and subdividing its cross-section into two angle section areas (A_1, A_2) and one rectangle area (A_3), on each side of the beam, symmetrically across the y-axis (Figure 4.64), each of which centroids lay a distance **d** from the center axis.
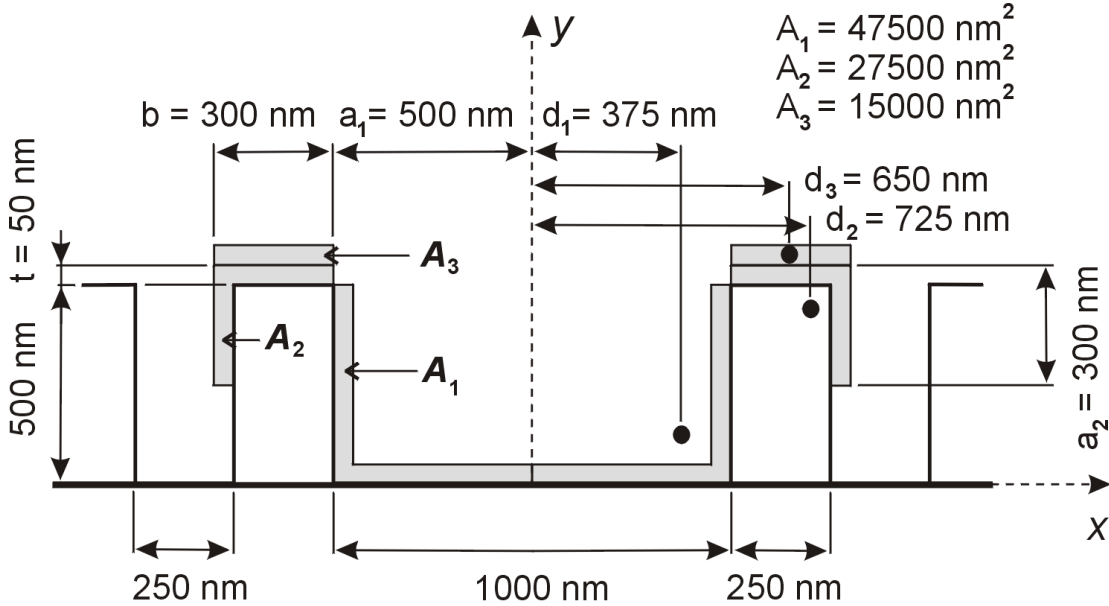

Figure 4.64: U-cross-section beam schematic drawing and segment division

It takes two 50 nm metal depositions at 45° to the plane of the substrate and 45° to the mask pattern lines direction to fabricate an area segment (four deposition in total for both sides), meaning that all segments have the same thickness $t = 50(\frac{1}{\sqrt{2}})(\frac{1}{\sqrt{2}}) + 50(\frac{1}{\sqrt{2}})(\frac{1}{\sqrt{2}}) = 50\,nm$

The second moment of area for an angle segment is I' = 5Aa^2/48, where the centroid is located at a distance a/4 from both sides, and for a rectangular area I' = Ab^2/12, with a centroid in the middle of the rectangle [45]. I_{yy} = I' + Ad^2 (parallel axis theorem), so the total second moment of area for our beam section is

$$I = 2\left(\frac{5A_1 a_1^2}{48} + \frac{5A_2 a_2^2}{48} + \frac{A_3 b^2}{12} + A_1 d_1^2 + A_2 d_2^2 + A_3 d_3^2\right) = 58,16.\,10^{-27}\,m^4$$

and A = 2(A_1+A_2+A_3).

L for the devices that we have fabricated is 140 μm, E of aluminum is 70GPa and the density of aluminum is 2700 kg/m^3 which gives (4.2)

f_{res} = 750 kHz.

By comparison, a conventional clamped-clamped beam of the same mass, cross-sectional area and length (300 nm thick and 300 nm wide rectangular cross-section) has a second moment of area I = Ab^2/12 = 0,68 .10^{-27} m^4 [45] and a resonant frequency of f_{res} = 80 kHz (4.2), i.e. we have achieved an order of magnitude improvement in theoretical mass sensitivity.

The true resonant frequency of our fabricated beam bridge structures is further raised by an unknown amount by to the tensile stress due to the buckle-beam mechanism suspension.

An attempt was made to actuate and detect resonance by using a parallel electrode/conductor providing the external field (electromagnetic actuation and detection), where the electrode acts as DC conductor providing the magnetic field, while an AC signal is applied to the bridge resonator, using a Gain-Phase analyzer, which was also used to detect an impedance/inductance change due to resonance. Different devices with electrode-resonator gap distances of 100nm, 250nm and 500nm were tried. No discernible resonant peaks were found within the expected resonant frequency range (0.5 to 5 MHz).

Electrostatic actuation and detection was also attempted, applying an AC signal between resonator and electrode using a Gain-Phase analyzer. We did not detect a meaningful signal in large gap distance devices (250nm, 500nm), and small gap distance devices (100nm) were destroyed by electrostatic discharge at potential differences as low as 0.1V (Figure 4.65, 4.67).


| 10μm* | Mag = 1.64 K X | WD = 14 mm | EHT = 5.00 kV | Date :18 Jan 2006 Time :16:32 |
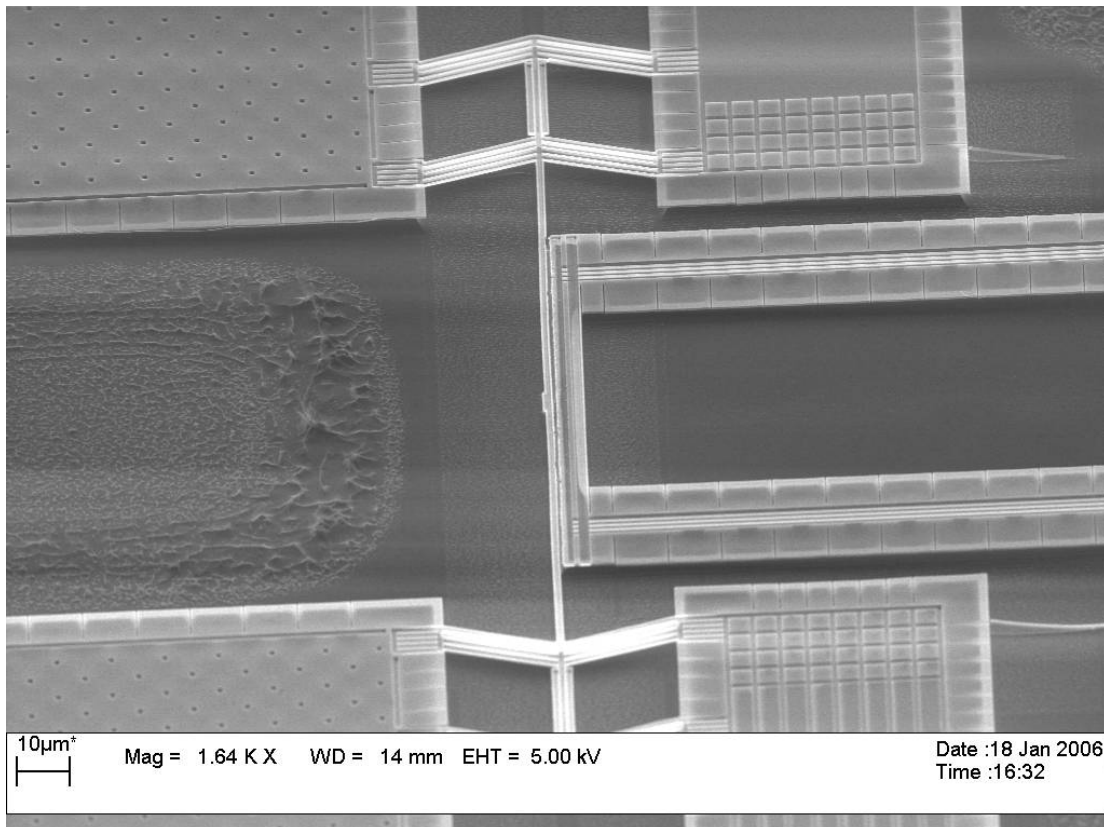
*Figure 4.65: Electrode and beam erosion due to electrostatic discharge*
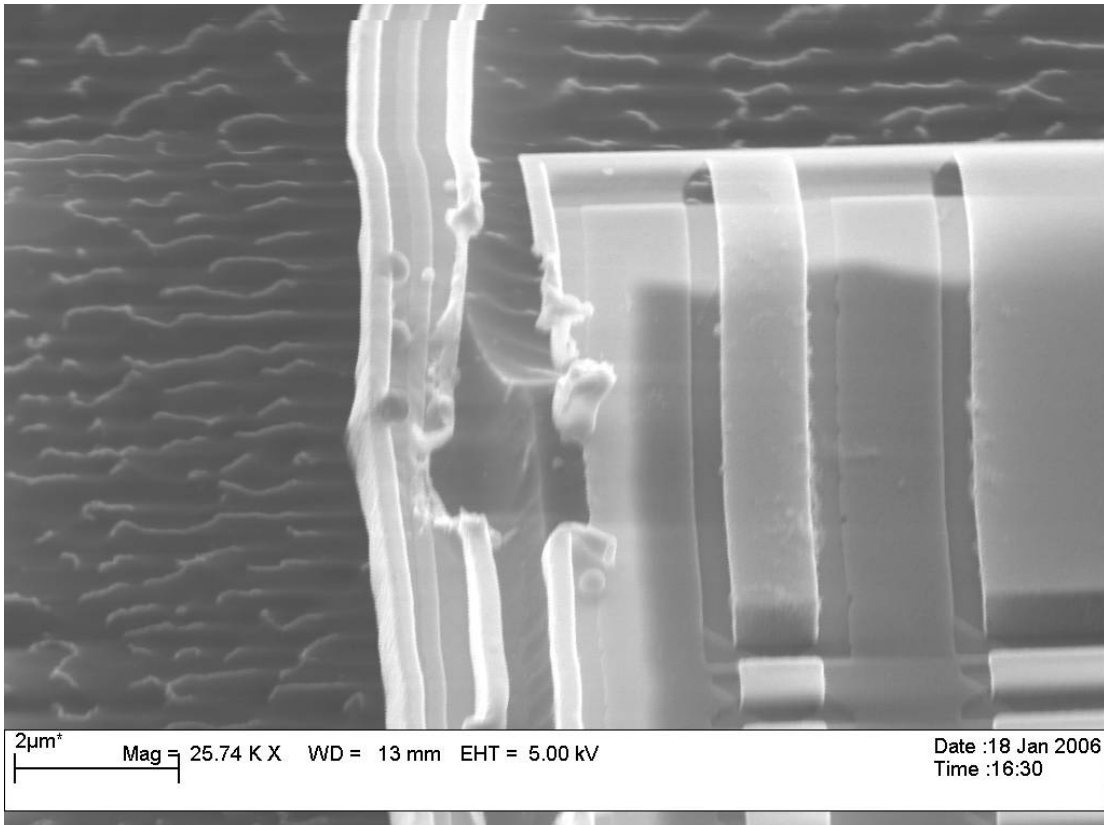
Figure 4.66: Close-up view of eroded beam and electrode showing one of the sites where discharge occurred and local melting

A possible solution to both electrostatic and electromagnetic actuation would be to reduce the gap distance further. This would put the resonant bridge structure deeper in the field of a parallel DC conductor and increase the induced current signals in it. A smaller gap distance could also prevent electrostatic discharge by reducing the gap to, or below, the electron avalanche distance for the device's particular cross-sectional shape. In this case, emitted electrons would cross the the electrode-bridge gap without causing electron avalanche and destructive discharge, i.e. a small gap distance could prevent the emitted electrons from ionizing the air between beam and electrode.

One could also control the resonator beam stress, and its resonant frequency in three ways.

– Increasing the number of parallel buckle beams on the buckle-beam suspension mechanisms would increase the force they exert on the resonator beam. In other words, a buckle beam suspension mechanism that has the same geometry for the buckle-beams, but comprises of two groups of eight buckle beams would result in twice larger tensile stress in the resonator beam. One could also achieve the same result by fabricating a buckle-beam suspension mechanism that comprises of four separate groups of four buckle-beams, connected by a straight beam along their central axis.

– Applying a DC component to the AC signal driving the resonator would heat-up the overall structure (suspension mechanisms and resonator) and result in further elongation for the separate beam components, which would then be translated into further stress-inversion by the buckle-beam mechanisms, i.e. the tensile stress within the resonator would increase.

– Decreasing the metal deposition rate during the sputtering process step would result in higher internal compressive stresses in the metal layer, which would then translate into higher tensile stresses in the suspended beam.

4.2.12 Applications and summary

The angled deposition peel-off fabrication process is material independent as it uses a geometrical self-shadowing effect. Hence, this process could be used to fabricate complex structures out of any material that is sputtered or that can be deposited directionally, or any materials combination in a laminar composite, by using multiple angled depositions. We have successfully demonstrated that internal stresses arising at the fabrication stage can be dealt with using careful engineering design.

The process is also substrate independent, as long as the substrate and resist layer can be etched separately. So, one could envision the same structures fabricated on a glass substrate, which is cheaper than silicon.

E-beam lithography is not necessary for implementing this process. Any process capable of producing narrow trenches in a resist layer (compared to the linewidth of intended channels) would be sufficient, i.e. one could also use laser lithography, UV lithography, X-ray lithography, Nanoimprint, etc.

One could also fabricate composite U-shaped cross-section structures using the same process, e.g. a structure that is made by four consecutive metal depositions, which is then oxidized for electrical insulation between channel and fluid, and than covered with gold by another four consecutive depositions. This would allow easy functionalization of the insides of the channel (as in an SPR "chip"), while separating the fluid and the channel electrically. One could also directly functionalize the metal oxide with a biomolecular layer, although this is is probably more difficult than with a gold layer.

The suspended open channel structures types that we have fabricated (coiled, meandering and straight bridges suspended by stress-inversion buckle-beam mechanisms) could be used for piezo-resistive measurements, where a change in the overall structure stress is induced by a bio-molecular layer, or multiple layers, on the channel walls. One can envision a whitstone bridge micro-system comprising four suspended channel devices, which are functionalized (or not) separately by using more than one reservoirs for spotting and capillary action, connected to individual devices.

An "individual device", in this context, doesn't need to be a single suspended structure. It could consist of several suspended structures with small anchors in between them, arranged in sequence with a single channel running across the anchors and structures. This may be needed in order to optimize an individual device's electrical resistance for best piezo-resistive measurement sensitivity; a single suspended structure has extremely low resistance.

More than one solutions could be delivered to individual devices by consecutive spotting, i.e. a solution is spotted in a reservoir, the fluid is delivered to the device via capillary action, the solution evaporates from the open channel and reservoir, then the process is repeated with a different solution.

One could have an array of such micro-systems on a chip, and perform many functionalizations and measurements in parallel using an automated spotting system, as in PCR array technology.

We have successfully demonstrated that a device consisting of parallel buckle-beams fabricated with the new process displaces along its central axis, under the influence of in-plane stress. The

same device could possibly be used for a bio-molecular layer induced stress detection by positioning an electrode contact on the displacement axis so that the device's "tip" (the foremost buckle-beam central point) and electrode make electrical contact after stress induced in the channel walls has resulted in displacement along that axis; compressive stress moves such a device in the direction of buckling, tensile stress moves such a device opposite the direction of buckling. Such a device could also be used in a capillary action micro-system array, like the one described above, and would probably offer better sensitivity, as surface stress would result in a digital signal ("on/off"), i.e. a biochemical interaction on the channel wall resulting in stress would "trigger" an electrical contact, rather than be the cause for an analogue signal. Precise digital measurements of analyte concentrations could be done using an array of those devices where the electrode-tip gap increases across the array. In this fashion, high concentrations would result in most of the devices in the array making electrical contact (most devices would displace by a large amount), and low concentrations would result in just the smaller gap devices making electrical contact.

Similarly, one could vary the devices segment lengths in an array, which would also result in different displacements for a constant analyte concentration.

One and the same single channel could connect all the devices on such an array, rather than having separate reservoirs per device.

It must be pointed out that this is not the only buckle-beam arrangement that can be used for motion/displacement amplification; cascaded buckle-beam devices [43] are also a useful approach to contact detection using hollow beams and stress induced on the channel insides. Most static electro-thermal actuator MEMS [37] device configurations would probably work for this purpose, as the two MEMS device families (static actuation electro-thermal MEMS and the "hollow suspended channel stress detection by electrical contact MEMS", that we propose) are essentially one and the same from an engineering stand point of view – both types of devices seek to translate a beam elongation into a deflection of a point of a suspended device.

A mixed solution between contact detection an piezo-resistive measurements is also possible with square double coiled spiral devices (Figure 4.35, top left), where surface channel stress results in internal coil rotation in the plane of the substrate and possibly out of plane twisting, until the coil makes electrical contact with itself, like in Figure 4.9, top right. This would lower its electrical resistance in a step fashion, i.e. such a device could also have a digital response to surface stress and be used in a parametrically varying array, as for the buckle-beam devices.

The angled deposition process also supports full integration of static channel devices such as chromatography columns, and could be used to create a fully-integrated lab-on-chip total analysis system for bio-applications, with various suspended and static devices operating in sequence or in parallel. Those could be calorimetric MEMS, chromatography columns, static suspended stress detection MEMS, dynamic/mass-sensing MEMS etc. All that is needed for a MEMS device design is a suspended, electrically conductive structure (so that it can move, and that there is electricity), and all that is needed of biological sensing is a way to deliver bio-agents and molecules (a solution) to it – we have successfully demonstrated how this can be done using U-shaped channels and capillary action.

Capillary action only works while the liquid channels are dry; once full the flow would stop. One way to alleviate this problem would be to use a enclosed channels system (rectangular cross-

section channels) with a fluid reservoir at one end and an open area evaporator at the other end of the system. Capillary action may not be sufficient to drive a liquid through such a system quickly enough for fast assays, and capillary action depends on the channels' top layer contact angle with respect to the fluid. To solve this problem one could also integrate one or more suspended MEMS pumping devices, that consist of one or more channels, and have a reciprocating motion in the axis of the channel(s), but whose channels have an isotropic resistance to fluid flow (a "Christmas tree"/"Connected arrowheads" channel form). One could use electrostatic actuator to move such a device along its axis. Electro-osmoticly driven flow is also a possibility. One could also use a reciprocation motion MEMS heat-engine to drive the pumping element(s). Such an engine could use an enzymatic reaction, or incorporate a secondary fluidic system for a high energy density fluid such as hydrazine which is catalyzed within a platinum covered channel.

Such a system needs not have specific applications. A MEMS device that switches the fluid flow between separate devices could possibly make it universally applicable to a wide range of bio-molecular assays. The switching action could also be provided by specific bio-molecular agents (such as DNA/RNA in the liquid solution under study), rather than externally.

Chapter 5

Conclusion

The main goal of this research has been to invent, design, research and implement alternative MEMS based devices and solutions that are market competitive.

In this research project we achieved the following:

– We invented, designed and researched parametrically a novel dynamic electro-thermal actuator. Our research shows that the new actuation principle is fully-scalable and lends itself to further improvement by downscaling.

– We characterized the performance of an electro-thermally actuated cantilever sensor using laser detection. Our research shows an order of magnitude better sensitivity to gas-sensing than theoretically expected.

– We discovered a novel detection method - rupture detection. We successfully detected the resonant frequency of a device using this novel method.

– We discovered a new structure that actuates to resonance, from our general research into resonant MEMS.

– We invented a novel process that allows dry-processing and fabrication of complex cross-section suspended structures out of any sputtered material, and on any substrate material.

– We invented a novel suspension mechanism that allows control over stress in a suspended structure fabricated out of an internally stressed fabrication layer.

– We invented a simple system that allows functionalization of suspended structures for sensing, using spotting and capillary action.

Our experience with MEMS research for bio-chemical and general sensing applications leaves us with the feeling that the field of MEMS bears an uncanny resemblance to the field of electronics, at its infancy.

Electronics applications began with spark radios; those were single elaborate devices designed to generate and detect radio waves that achieved very little in terms of actual applications. Research into single MEMS devices, like the dynamic-electro thermal actuation principle that we have investigated is likewise fraught with difficulty and involves complex phenomena investigation for little return in potential applications.

Commercially applicable Electronics began with the invention of the vacuum tube, which is a "switching"/"control" element that allows the design and invention of many different circuits using a small set of elements. The first commercial radios were made of glass vacuum tubes, paper-metal capacitors, wound coil inductors and resistors connected together in a circuit by wires on wooden boards. In essence, those were still overly elaborate devices that were complex to manufacture, required different manufacturing techniques per device, and only found commercial applications on ships (one radio per ship), i.e. the unit numbers manufactured were not particularly high, and the product (radios) did not really lend itself to mass-production. This is also borne out of recent MEMS research projects, such as the NANOMASS project, where different devices (a CMOS amplifier and a MEMS resonator) are fabricated using different techniques and connected in a piecemeal fashion, which ultimately drives cost up, and performance down.

It took the advent of CMOS fabrication for electronics to achieve the vast commercial success it enjoys today; CMOS and silicon manufacturing allow for all electronics elements to be fabricated simultaneously, using one and the same process, in one plane (that of an integrated circuit), along with the actual circuit.

In other words, commercial success was achieved when a process/fabrication method was found to fabricate all necessary circuit elements in parallel, using one and the same process (CMOS). Reducing element sizes, over the years, also helped driving the cost down by reducing the raw materials needed per circuit, i.e. by reducing the overall circuit area.

With that comparison in mind, our research has been very successful for three reasons

–   We have gained important insights into the design and operation of MEMS elements from our scientific and experimental investigation into dynamic-electro-thermal actuation and detection, as well as our general research into MEMS devices. Those insights will be invaluable when it comes to continuing our research into integrated systems.

–   We have been true to our motivation and stated research values and achieved fabrication of elements that can be as cheap as a gold covered glass slide, because they are essentially a metal layer on a substrate (that we have shaped into structures using lithography)

–   We have successfully demonstrated the feasibility of integration of bio-detection fluidic MEMS elements on a system level, using a novel process, that we believe can potentially be to the field of MEMS what CMOS fabrication was to the field of electronics.

Bibliography

[1]T. Mimura and S. Sakai. "Micro-Piezoelectric Head Technology of Color Inkjet Printer", *DPP 2001: Eye on the Future*, 230-234, 2001

[2] L. J. Hornbeck, "Digital light processing for high-brightness, high-resolution applications," *Proceedings of the SPIE - The International Society for Optical Engineering*, 3013:27–40, 1997

[3] P.F. Van Kessel, L.J. Hornbeck, R.E. Meier, M.R. Douglass, "A MEMS-based projection display", *Proceedings of the IEEE*, 86(8): 1687-1704,

[4] L. J. Hornbeck, "Digital light processing update-status and future applications", *Proceedings of SPIE - The International Society for Optical Engineering*, 3634: 158-170, 1999

[5] N. Barbour and G. Schmidt, "Inertial sensor technology trends" *Proceedings of the IEEE*, 1(Sensors J.): 332–9, 2001

[6] C. Acar and A. M. Shkel, "Experimental evaluation and comparative analysis of commercial variable-capacitance MEMS accelerometers", *J. Micromech. Microeng.* (13): 634-645, 2003

[7] G. Binnig, C.F. Quate, and C. Gerber. "Atomic force microscope". *Physical Review Letters*, 56(9):930–3, 1986.

[8] P. Vettiger, M. Despont, U. Drechsler, U. Du¨ rig, W. Ha¨ berle, M. I. Lutwyche, H. E. Rothuizen, R. Stutz, R. Widmer, G. K. Binnig, "The "Millipede"— More than one thousand tips for future AFM data storage", *IBM J. Res. Develop.* 44(3): 323-340, 2000

[9] J. M. McDonnell, "Surface plasmon resonance: towards an understanding of the mechanisms of biological molecular recognition", *Curr. Opin. Chem. Biol*, 572-577, 2001

[10] Chen, G. Y.; Thundat, T.; Wachter, E. A.; Warmack, R. J.Source, "Adsorption-induced surface stress and its effects on resonance frequency of microcantilevers".*Journal of Applied Physics*, 77(8): 3618-3623, 1995

[11] G. Meyer and N.M. Amer. "Novel optical approach to atomic force microscopy", *Applied Physics Letters*, 53(12):1045–7, 1988.

[12] A. Boisen, J. Thaysen, H. Jensenius, O. Hansen, "Environmental sensors based on micromachined cantilevers with integrated read-out". *Ultramicroscopy*, 82(1-4): 11-16, 2000

[13] M. Yue, H. Lin, D.E. Dedrick, S. Satyanarayana, A. Majumdar, A.S. Bedekar, J.W. Jenkins

and S. Sundaram "A 2-D microcantilever array for multiplexed biomolecular analysis". *Journal of Microelectromechanical Systems*, 13(2):290–299, 2004.

[14]F. Amiot, F. Hild, J.P. Roger, L.T. Tel "Model and parameter identification using non-contact loading and full-field measurement", *Proceedings of the 2005 SEM Annual Conference and Exposition on Experimental and Applied Mechanics,* 1089-1098, 2005

[15] E. Ollier, "Optical MEMS devices based on moving waveguides", *IEEE Journal on Selected Topics in Quantum Electronics*, 8(1):155 -162, 2002

[16] Y. Arntz, J. D. Seelig, H. P. Lang, J. Zhang, P. Hunziker, J. P. Ramseyer, E. Meyer, M. Hegner and Ch. Gerber, " Label-free protein assay based on a nanomechanical cantilever array", *Nanotechnology,* 14: 86-90, 2003

[17] F. Huber, M. Hegner, C. Gerber, H. J. Guntherodt, H. P. Lang, "Label free analysis of transcription factors using microcantilever arrays", *Biosensors and Bioelectronics*, 21(8):1599-605, 2006

[18] G. Christensen, "Mekanik", 9.1-9.22, 2000

[19] N. V. Lavrik, Michael J. Sepaniak, Panos G. Datskos, "Cantilever transducers as a platform for chemical and biological sensors"**,** *Review of Scientific Instruments*, 75(7): 2229-2253, 2004

[20] J. W. M. Chon, P. Mulvaney, J. E. Sader, "Experimental validation of theoretical models for the frequency response of atomic force microscope cantilever beams immersed in fluids".

Journal of Applied Physics, 87(8): 3978-3988, 2000

[21] G. Stemme. "Resonant silicon sensors. Journal of Micromechanics and Microengineering", 1(2):113–125, 1991.

[22] R. Sondberg, "Characterisation of the resonant properties of multy-layer cantilever sensors". PhD thesis, MIC, Technical University of Denmark, 2005

[23] J. Verd, G. Abdal, J. Teva, M.V. Gaudo, A. Uranga, X. Borrise, F. Campabadal, J. Esteve, E.F. Costa, F. Perez-Murano, Z.J. Davis, E. Forcen, A. Boisen, N. Barniol, "Design, fabrication, and characterization of a submicroelectromechanical resonator with monolithically integrated CMOS readout circuit", *Journal of Microelectromechanical Systems*, 14(3):508-519, 2005

[24] T. Lamminmaki, K. Ruokonen, I. Tittonen, T. Manila, O. Jaakola, A. Oja, H. Seppa, P.

Seppala, J. Kiihamaki, "Electromechanical analysis of micromechanical SOI-fabricated RF resonators",

2000 International Conference on Modeling and Simulation of Microsystems - MSM 2000, 217-220, 2000

[25] Z. J. Davis, "Nano-resonators for high resolution mass detection", PhD thesis, MIC, Technical University of Denmark, 2005

[26] K. L. Ekinci, Y. T. Yang, M. H. Huang and M. L. Roukes, "Balanced electronic detection of displacement in nanoelectromechanical systems", *Applied Physics Letters* , 81(12): 2253-2255, 2002

[27] T. Thundat, E.A. Wachter, S.L. Sharp, and R.J. Warmack. "Detection of mercury vapor using resonating microcantilevers". *Applied Physics Letters*, 66(13):1695–7, 1995.

[28] J.D. Adams, G. Parrott, C. Bauer, T. Sant, L. Manning, M. Jones, B. Rogers, D. McCorkle, and T.L. Ferrell. "Nanowatt chemical vapor detection with a self-sensing, piezoelectric microcantilever array". *Applied Physics Letters*, 83(16): 3428–3430, 2003.

[29] T. Thundat, G.Y. Chen, R.J.Warmack, D.P. Allison, and E.A.Wachter. "Vapor detection using resonating microcantilevers". *Analytical Chemistry*, 67(3):519–521, 1995.

[30] N. Ledermann, P. Muralt, J. Baborowski, M. Forster, and J.-P. Pellaux. "Piezoelectric pb(zr_x, ti_{1-x})o$_3$ thin film cantilever and bridge acoustic sensors for miniaturized photoacoustic gas detectors". *Journal of Micromechanics and Microengineering*, 14(12):1650– 1658, 2004.

[31] K.S.Hwang, J. H. Lee, J. Park, J. H. Park, and T. S. Kim. "Protein mass detection system in liquid for prostatespecific antigen (PSA) using PDMS liquid cell by resonant frequency shift of micromachined PZT cantilever". *Miniaturized Chemical and Biochemical Analysis Systems, 2003. 7th International Conference on*, 1267–1269, 2003.

[32] T.P. Burg and S.R. Manalis. "Suspended microchannel resonators for biomolecular detection". *Applied Physics Letters*, 83(13):2698–2700, 2003.

[33] B. Ilic, H.G. Craighead, S. Krylov, W. Senaratne, C. Ober, and P. Neuzil. "Attogram detection using nanoelectromechanical oscillators". *Journal of Applied Physics*, 95(7):3694–3703, 2004.

[34] G. Abadal, Z.J. Davis, B. Helbo, X. Borrise, R. Ruiz, A. Boisen, F. Campabadal, J. Esteve, E. Figueras, F. Perez-Murano, and N. Barniol. "Electromechanical model of a resonating nano-antilever-based sensor for high-resolution and high-sensitivity mass detection". *Nanotechnology,*

12(2):100–104, 2001.

[35] J. Jonsmann, O. Sigmund and S. Bouwstra, "Compliant electro-thermal microactuators" , *Micro Electro Mechanical Systems, 1999. MEMS '99. Twelfth IEEE International Conference on,* 588 -593,1999

[36] M. Emmenegger, S. Taschini, J.g. Korvinik and H. Baltes. "Simulation of a thermomechanically actuated gas sensor", *Micro Electro Mechanical Systems, 1998. MEMS 98. Proceedings.,* 184 -189, 1998

[37] E. S. Kolesar, P. B. Allen, J. T. Howard, J. M. Wilken, N. Boydston, "Thermally-actuated cantilever beam for achieving large in-plane mechanical deflections", *Thin Solid Films*, 355-356: 295-302, 1999

[38] G. Rogers, Y. Mayhew, "Engineering thermodynamics. Work and Heat Transfer", 4th Edition, 1992

[39] S. Kirstein, M. Mertesdorf, M. Schönhoff, "The influence of a viscous fluid on the vibration dynamics of scanning near-field optical microscopy fiber probes and atomic force microscopy cantilevers", *Journal Of Applied Physics*, 84(4):1782-1790, 1998

[40] E. Forsen, S. G. Nilsson, P. Carlberg, G. Abadal, F. Perez-Murano, J. Esteve, J. Montserrat, E. Figueras, F. Campabadal, J. Verd, L. Montelius, N. Barniol, A. Boisen , "Ultrasensitive mass sensor fully integrated with complementary metal-oxide-semiconductor circuitry", *Nanotechnology,* 15 (7): S628-S633, 2004

[41] K. A. Mørch, "Måletekniske begreber og behandling af måledata", 2000

[42] T. Tanaka, M. Morigami, H. Oizumi and T. Ogawa, "Freeze-drying process to avoid resist pattern collapse, *Japanese Journal of Applied Physics*, *Part 1* 32(12A):5813-5814, 1993

[43] L. Que, J.-S. Park, Y.B. Gianchandani, "Bent-beam electro-thermal actuators for high force applications", *Micro Electro Mechanical Systems, 1999. MEMS '99. Twelfth IEEE International Conference on ,* 31-36, 1999

[44] A. V. Grigorov, "RF micro electro-mechanical devices", 4th year project report, Department of Engineering Science, University of Oxford, 2002

[45] A.M. Howatson, P.G. Lund, J.D. Todd, "Engineering Tables and Data", 2nd edition, 1991

Appendix A

Publications

1. A.V. Grigorov, Z.J. Davis, P. Rasmussen, A. Boisen, "A longitudinal thermal actuation principle for mass detection using a resonant micro-cantilever in a fluid medium", *Microelectronic Engineering,* 73–74: 881–886, 2004

2. A.V. Grigorov, A. Boisen, "Novel resonant cantilever mass change detection and resonant frequency tuning", *Microelectronic Engineering,* 78–79: 190–194, 2005

3. P A Rasmussen, A. V. Grigorov, A. Boisen, "Double sided surface stress cantilever sensor", *J. Micromech. Microeng.* 15:1088-1091, 2005

4. A.V. Grigorov, Z.J. Davis, P. Rasmussen, A. Boisen, "A longitudinal thermal actuation principle for mass detection using a resonant micro-cantilever in a fluid medium", *Proceedings of MNE 2004*, 228-229, 2003

5. A.V. Grigorov, A. Boisen, "Novel resonant cantilever mass change detection and resonant frequency tuning", *Proceedings of MNE 2004*, 228-229, 2004

6. A.V. Grigorov, P. Rasmussen, A. Boisen, "Dynamic thermal actuation for resonating cantilevers", MRS conference abstract, 2004

Appendix B

Optical detection measurements processing

The software package Igor Pro 4.091 was used to do the statistical analysis of the measurements using the following code.

```
#pragma rtGlobals=1                // Use modern global access method.

function DisplayAmpAndPhase (wname)
        string      wname

        dowindow /k $wname
        Display /W=(10,10,400,250) Amp vs Frekvens
        AppendToGraph/R Phase2 vs Frekvens
        dowindow /c $wname

        ModifyGraph gbRGB=(61166,61166,61166)
        ModifyGraph margin(bottom)=48
        ModifyGraph margin(left)=51
        ModifyGraph margin(right)=51
        ModifyGraph lblMargin(bottom)=10
        ModifyGraph lblMargin(left)=7
        ModifyGraph lblMargin(right)=7
        ModifyGraph lblRot(right)=180
        Label bottom "Frequency / \u#2kHz"
        Label left "\\K(0,0,65280)Amplitude / dB"
        Label right "\\K(0,39168,19712)Phase / deg"

        ModifyGraph lsize(Amp)=2, rgb(Amp)=(0,0,65280)
        ModifyGraph lsize(Phase2)=2, rgb(Phase2)=(0,39168,19712)

        CurveFit /Q /L=1000 gauss Amp /X=Frekvens /D
        //CurveFit /Q /L=1000 poly 15, Amp /X=Frekvens /D

        CurveFit /Q /L=1000 sigmoid, Phase2 /X=Frekvens /D
        //CurveFit /Q /L=1000 poly 15, Phase2 /X=Frekvens /D
end

function Load (filename)
        string      filename

        loadwave /n /w /g /d filename
end

function FixPhase (displace)
        variable    displace

        duplicate /o Phase, Phase2
        variable    i1, i2
        // fix wrap arounds
        for (i1=0; i1<numpnts(Phase2)-1; i1+=1)
                variable    diff = Phase2[i1+1] - Phase2[i1]
                if (diff >= 180)
                        for (i2=i1+1; i2<numpnts(Phase2); i2+=1)
                                Phase2[i2] -= 360
                        endfor
                elseif (diff <= -180)
                        for (i2=i1+1; i2<numpnts(Phase2); i2+=1)
```

```
                                        Phase2[i2] += 360
                                endfor
                        endif
                endfor
        for (i1=0; i1<numpnts(Phase2); i1+=1)
                Phase2[i1] += displace
        endfor
end

function CalcDeviation ()
        variable    i
        variable    fmean = 0              // f mean for amplitude
        variable    f2mean = 0             // f mean for phase
        variable    amean = 0              // mean amplitude
        make /o /n=20 fmax                 // f max for amplitude
        make /o /n=20 f2max                // f max for phase
        make /o /n=20 amax                 // amplitude max

        for (i=0; i<20; i+=1)
                string      filename
                sprintf filename, "C:\\Documents and Settings\\Morten Fugl\\My Documents\\10061\\rap\\mofu5\\uncert_120s_big_%02d.txt", i+1
                Load (filename)
                FixPhase (0)
                //Smooth 1000, Amp
                DisplayAmpAndPhase ("mygraph")
                // Amp stats:
                WaveStats /q fit_Amp
                variable    fval = V_maxloc
                //variable   fval = ix[V_maxloc]
                variable    aval = V_max
                fmax[i] = fval
                amax[i] = aval
                fmean += fval
                amean += aval
                // Phase stats:
                FindLevel fit_Phase2, 0
                f2max[i] = V_LevelX
                f2mean += V_LevelX
        endfor
        fmean /= 20
        f2mean /= 20
        amean /= 20

        variable    f_u = 0
        variable    f2_u = 0
        variable    a_u = 0
        for (i=0; i<20; i+=1)
                f_u += (fmax[i] - fmean)^2
                f2_u += (f2max[i] - f2mean)^2
                a_u += (amax[i] - amean)^2
        endfor
        f_u = sqrt(f_u/(20 - 1))*1.03
        f2_u = sqrt(f2_u/(20 - 1))*1.03
        a_u = sqrt(a_u/(20 - 1))*1.03
        printf "Amplitude: mean(f_res)=%f, mean(A_res)=%f, u(f_res)=%f, u(A_res)=%f\r", fmean, amean, f_u, a_u
        printf "Phase: mean(f_res)=%f, u(f_res)=%f\r", f2mean, f2_u
end

function CreateDemoResonancePeak ()
        make /o /n=10000 Amp
        make /o /n=10000 Phase
        variable    omega0 = 2*pi
        variable    gamma =0.5
        Amp = 30/sqrt((omega0^2 - (x/100)^2)^2 + gamma^2*(x/100)^2)
```

```
Phase = atan(gamma*(x/100)/(omega0^2 - (x/100)^2))*180/pi
variable    i
variable    i2
for (i=0; i<10000; i+=1)
        if (Phase[i] < -1.0)
                for (i2=i; i2<10000; i2+=1)
                        Phase[i2] += 180
                endfor
                break
        endif
endfor
Display /W=(10,10,400,250) Amp
AppendToGraph/R Phase
ModifyGraph gbRGB=(61166,61166,61166)
ModifyGraph rgb(Amp)=(0,0,65280),lsize(Phase)=2,rgb(Phase)=(0,39168,19712)
ModifyGraph lsize=2
Label left "\\K(0,0,65280)Amplitude"
Label bottom "Frequency"
Label right "\\K(0,39168,19712)Phase / deg"
ModifyGraph lblRot(right)=180
ModifyGraph margin(bottom)=48
ModifyGraph margin(left)=51
ModifyGraph margin(right)=51
ModifyGraph lblMargin(bottom)=10
ModifyGraph lblMargin(left)=7
ModifyGraph lblMargin(right)=7

ModifyGraph tlblRGB(left)=(65535,65535,65535)
ModifyGraph tlblRGB(bottom)=(65535,65535,65535)
SetAxis bottom 400,900
end
```

Appendix C

Angled deposition masks generation macro

Parametric investigation into angled deposition fabrication of Z-cross-section structures, U-cross-section structures, rectangular anchoring, hexagonal anchoring and triangular fenced anchoring was performed using arrays of devices generated using the following code (L-Edit macro).

```c
module MEMS_module
{
#include <stdlib.h>
#include <math.h>
#include "ldata.h"


void  MEMSmacro ( void )
{
        /*****************************************************************/
        /* Draws spiral, rotates in 4 degree increments.  1995-11-27 Croft  */
        /*****************************************************************/
        double    overL, TL, W, S, N1, N2, L, movex, incr, finH,  finA, midH, midW, up, down, left, right, outw, AnchorX,  rot, wafB, wafT, zedH, zedL, outW,
                hexS, hexA, bacL, bacW;
        long      i, j, k, l,m, Points_Total;
         int        both, Imid, Tmid, Tmid2, Tmid2A, Iside, TopSide, m1, m2, m3, m4, res, waf, wafNo, zed, zedNo, zedE, hex, hexNo, bac, bacNo;

        LDerivedLayerParamEx830 MyPar;
        LDerivedLayerBoolOperation MyBool;
        LDerivedLayerOperation MyOper;

        LObject             Box;

        LPoint              points[4];
        LPoint              Translation ;
        LPoint              Temp;
        LRect               rect;

        LFile pFile = LFile_Find( "MacroFile" );
        if ( pFile )
        {
        LFile_Close (pFile);
        }

        LFile File_Draw  = LFile_Open( "H:\\masks\\MacroFile.tdb", LTdbFile );


        LCell Cell_Draw = LCell_Find( File_Draw, "Cell0" );


        /*total length */                  TL = (50)*1000;
        /*width*/                          W = (0.7)*1000;
        /*spacing*/                        S = (0.25*2 + 0.25 + 2*0.8)*1000;
        /*overlap*/                        overL = (0.25)*1000;
        /*start number*/                   N1 = (1);
        /*stop number*/                    N2 = (2);
        /*increment*/                      incr = (1);
        /*mid element length*/             midH = (10)*1000;
        /*mid element width*/              midW = (0.6)*1000;
        /*side element area*/              finA = (20)*1000000;
        /*modify sides*/                   Iside = (0);
        /*sides on top layer*/             TopSide = (0);
        /*both sides*/                     both = 1;
        /*mod bot mids W-N-W*/             Imid = (0);
        /*mod top mids W-N-W*/             Tmid = (1);
        /*mod top mids D-O-D*/             Tmid2 = (0);
        /*mod D-O-D all*/                  Tmid2A = (0);

        /*resistor bottom ON*/   res = 1;


        /*Z side achor*/                   zed = 0;
        /*Z side V height*/                zedH =(4)*1000;
        /*Z edge */                        zedE = 0;
```

```
/*waffle achor*/                        waf = 0;
/*waf bottom X*/                        wafB = (1.5)*1000;
/*waf Top X*/                           wafT = (0.25)*1000;

/*honeycomb anchor*/                    hex = 0;
/*hex side W*/                          hexA = (0.75)*1000;
/*hex spacing*/                         hexS = (0.15)* 1000;

/*bacterium anchor*/                    bac = 0;
/*leg width */                          bacW = (2)*1000;
/*leg legth*/                           bacL = (2)*1000;

Translation.x = (0)*1000*1000;
Translation.y = (0)*1000*1000;

/*mod res 1*/                           m1 = (1);
/*mod res 2*/                           m2 = (1);
/*mod res 3*/                           m3 = (1);
/*mod res 4*/                           m4 = (0);
/* up*/                                 up = (0.8)*1000;
/* down*/                               down = (0.8)*1000;
/* left*/                               left = (0.8)*1000;
/* right*/                              right = (0.8)*1000;
/* outline width */                     outW = (0.25)*1000;
/*rotate deg.*/                         rot = 0;

MyPar.name = "Derived Poly";
MyPar.enable_evaluation = 1;
MyPar.derivation_type = LDOT_Bool;

MyBool.src_layer1 = "Poly2";
MyBool.src_layer2 = "Poly2";
MyBool.layer2_not_op = 1;
MyBool.layer1_grow_amount = outW;
MyBool.layer1_bool_layer2 = 1;

MyOper.boolean = MyBool;
MyOper.operation = MyOper;
LLayer_SetDerivedParametersEx830(File_Draw, LLayer_Find ( File_Draw, "Derived Poly" ), &MyPar);

LSelection_DeselectAll ();


movex=  1000*1000;
j = N1-incr;
do { j=j+incr;

L= (TL-(2*W+S)*j)/j;

/*remove!!!!!!!*/
if (j == 2) midH = 5000;
/* remove!!!*/


Translation.x = Translation.x + movex;
finH = (finA - S*S)/(2*W+S);

LSelection_DeselectAll ();


if (res==1)
{
            /*draw 4 resistors minus the mid points */
i=0;
do {        i++;

            if (Tmid2 == 0)
            {
            Box = LBox_New ( Cell_Draw, LLayer_Find ( File_Draw, "Poly" ),
                            Translation.x  , Translation.y + ((2*i-1)*(W+S)) , Translation.x +  L/2- midH/2 + (right + left + S - up - down)/2 +
            overL, Translation.y +((2*i-1)*(W+S)) + W );
            LSelection_AddObject (Box);

            Box = LBox_New ( Cell_Draw, LLayer_Find ( File_Draw, "Poly" ),
                            Translation.x  , Translation.y + ((2*i-1)*(W+S)), Translation.x  - W, Translation.y + ((2*i)*(W+S)) + W);
            LSelection_AddObject (Box);

            Box = LBox_New ( Cell_Draw, LLayer_Find ( File_Draw, "Poly" ),
                            Translation.x  , Translation.y + ((2*i)*(W+S)) , Translation.x  + L/2 - midH/2 - (right + left + S - up - down)/2,
            Translation.y + ((2*i)*(W+S)) + W );
            LSelection_AddObject (Box);

            Box = LBox_New ( Cell_Draw, LLayer_Find ( File_Draw, "Poly" ),
                            Translation.x  + L/2 + midH/2 + (right + left + S - up - down)/2, Translation.y + ((2*i)*(W+S))  , Translation.x + L,
            Translation.y + ((2*i)*(W+S)) + W);
            LSelection_AddObject (Box);
```

```
                    Box = LBox_New ( Cell_Draw, LLayer_Find ( File_Draw, "Poly" ),
                                        Translation.x+ L  , Translation.y + ((2*i)*(W+S)) , Translation.x + L+W, Translation.y + ((2*i+1)*(W+S)) + W);
                    LSelection_AddObject (Box);


                    Box = LBox_New ( Cell_Draw, LLayer_Find ( File_Draw, "Poly" ),
                                        Translation.x + L/2 + midH/2 - (right + left + S - up - down)/2 - overL, Translation.y + ((2*i+1)*(W+S))  ,
                    Translation.x+ L, Translation.y  + ((2*i+1)*(W+S)) + W);
                    LSelection_AddObject (Box);
                    }
                    else
                    {
                    Box = LBox_New ( Cell_Draw, LLayer_Find ( File_Draw, "Poly" ),
                                        Translation.x  , Translation.y + ((2*i-1)*(W+S))  , Translation.x  + L/2 - midH/2 - (right + left + S - up - down)/2,
                    Translation.y +((2*i-1)*(W+S)) + W );
                    LSelection_AddObject (Box);

                    Box = LBox_New ( Cell_Draw, LLayer_Find ( File_Draw, "Poly" ),
                                        Translation.x  , Translation.y + ((2*i-1)*(W+S)), Translation.x  - W, Translation.y + ((2*i)*(W+S)) + W);
                    LSelection_AddObject (Box);

                    Box = LBox_New ( Cell_Draw, LLayer_Find ( File_Draw, "Poly" ),
                                        Translation.x  , Translation.y + ((2*i)*(W+S)) , Translation.x  + L/2 - midH/2 - (right + left + S - up - down)/2,
                    Translation.y + ((2*i)*(W+S)) + W );
                    LSelection_AddObject (Box);

                    Box = LBox_New ( Cell_Draw, LLayer_Find ( File_Draw, "Poly" ),
                                        Translation.x  + L/2 + midH/2 + (right + left + S - up - down)/2, Translation.y + ((2*i)*(W+S))  , Translation.x + L,
                    Translation.y + ((2*i)*(W+S)) + W);
                    LSelection_AddObject (Box);

                    Box = LBox_New ( Cell_Draw, LLayer_Find ( File_Draw, "Poly" ),
                                        Translation.x+ L  , Translation.y + ((2*i)*(W+S)) , Translation.x + L+W, Translation.y + ((2*i+1)*(W+S)) + W);
                    LSelection_AddObject (Box);

                    Box = LBox_New ( Cell_Draw, LLayer_Find ( File_Draw, "Poly" ),
                                        Translation.x  + L/2 + midH/2 + (right + left + S - up - down)/2, Translation.y + ((2*i+1)*(W+S))  , Translation.x+
                    L, Translation.y  + ((2*i+1)*(W+S)) + W);
                    LSelection_AddObject (Box);


                    }

        } while (i < j);
        }

                    AnchorX = L/2 + finH +W + S+7000;
                    if (AnchorX< 60000) AnchorX = 60000;

        if (waf==0 && zed==0 && hex == 0 && bac ==0)
        {

                    if (Tmid2A ==0)
                    {
                                Box = LBox_New ( Cell_Draw, LLayer_Find ( File_Draw, "Poly" ),
                                            Translation.x + L/2 , Translation.y + 2*W +S  , Translation.x + L/2+ AnchorX, Translation.y +2*W +S
                                - AnchorX );
                                LSelection_AddObject (Box);

                                Box = LBox_New ( Cell_Draw, LLayer_Find ( File_Draw, "Poly" ),
                                            Translation.x + L/2 , Translation.y + (2*j+1)*(W +S)  , Translation.x +L/2 - AnchorX, Translation.y
                                +(2*j+1)*(W+S) +  AnchorX );
                                LSelection_AddObject (Box);
                    }
                    else
                    {
                                Box = LBox_New ( Cell_Draw, LLayer_Find ( File_Draw, "Poly" ),
                                            Translation.x + L/2 , Translation.y + 2*W +S - outW  , Translation.x + L/2+ AnchorX, Translation.y
                                +2*W +S -  AnchorX );
                                LSelection_AddObject (Box);

                                Box = LBox_New ( Cell_Draw, LLayer_Find ( File_Draw, "Poly" ),
                                            Translation.x + L/2 , Translation.y + (2*j+1)*(W +S)  , Translation.x +L/2 - AnchorX, Translation.y
                                +(2*j+1)*(W+S) +  AnchorX );
                                LSelection_AddObject (Box);
                    }


        }
        else if (waf ==1)
        {

                    wafNo = AnchorX / (wafB + wafT) + 1;
                    AnchorX = (wafB+wafT)* wafNo + wafB;

                    l=-1;
                    do {l++;
```

```
                m = -1;
                do {m++;
                Box = LBox_New ( Cell_Draw, LLayer_Find ( File_Draw, "Poly" ),
                        Translation.x + L/2 + l*(wafB+wafT) , Translation.y + 2*W +S- m*(wafB+wafT)  , Translation.x + L/2+ l*(wafB+wafT) +
                wafB, Translation.y +2*W +S -  m*(wafB+wafT) - wafB );
                LSelection_AddObject (Box);
                Box = LBox_New ( Cell_Draw, LLayer_Find ( File_Draw, "Poly" ),
                        Translation.x + L/2 - l*(wafB+wafT)  , Translation.y + (2*j+1)*(W +S) + m*(wafB+wafT)  , Translation.x +L/2 -
                l*(wafB+wafT) - wafB, Translation.y +(2*j+1)*(W+S) +  m*(wafB+wafT) + wafB );
                LSelection_AddObject (Box);

                } while (m < wafNo);
                } while (l < wafNo);

}
else if (zed ==1)
{

zedNo = AnchorX / (zedH);
AnchorX = (zedH)* zedNo ;

if (zedE ==0)
{
Box = LBox_New ( Cell_Draw, LLayer_Find ( File_Draw, "Poly" ),
                Translation.x + L/2 , Translation.y + 2*W +S  , Translation.x + L/2+ AnchorX, Translation.y +2*W +S -  W );
LSelection_AddObject (Box);

Box = LBox_New ( Cell_Draw, LLayer_Find ( File_Draw, "Poly" ),
                Translation.x + L/2 , Translation.y + 2*W +S  - down - zedH -W , Translation.x + L/2+ AnchorX, Translation.y +2*W +S -
AnchorX );
LSelection_AddObject (Box);

}
else
{
Box = LBox_New ( Cell_Draw, LLayer_Find ( File_Draw, "Poly" ),
                Translation.x + L/2 , Translation.y + 2*W +S  - down - zedH , Translation.x + L/2+ AnchorX, Translation.y +2*W +S -
AnchorX );
LSelection_AddObject (Box);
}
                l=-1;
                do {l++;

                if (zedE==1)
                {

                        if (l==0)
                        {
                        points[0] = LPoint_Set(Translation.x + L/2 + l*zedH  , Translation.y + 2*W +S - down - down/2);
                        points[1] = LPoint_Set(Translation.x + L/2 + l*zedH, Translation.y + 2*W +S - down - down/2- zedH*2);
                        points[2] = LPoint_Set(Translation.x + L/2 + zedH+ l*zedH, Translation.y + 2*W +S - down- down/2 - zedH*2);
                        }
                        else
                        {
                        points[0] = LPoint_Set(Translation.x + L/2 + l*zedH  , Translation.y + 2*W +S - down);
                        points[1] = LPoint_Set(Translation.x + L/2 + l*zedH, Translation.y + 2*W +S - down - zedH*2);
                        points[2] = LPoint_Set(Translation.x + L/2 + zedH+ l*zedH, Translation.y + 2*W +S - down - zedH*2);
                        }

                        Box = LPolygon_New ( Cell_Draw, LLayer_Find ( File_Draw, "Poly" ), points, 3 );
                        LSelection_AddObject (Box);

                        points[0] = LPoint_Set(Translation.x + L/2+ l*zedH, Translation.y + 2*W +S - down - zedH*2);
                        points[1] = LPoint_Set(Translation.x + L/2 + zedH+ l*zedH, Translation.y + 2*W +S - down);
                        points[2] = LPoint_Set(Translation.x + L/2 + zedH+ l*zedH, Translation.y + 2*W +S - down - zedH*2);

                        Box = LPolygon_New ( Cell_Draw, LLayer_Find ( File_Draw, "Poly" ), points, 3 );
                        LSelection_AddObject (Box);

                        points[0] = LPoint_Set(Translation.x + L/2+ l*zedH - 25, Translation.y + 2*W +S - outW + 100  );
                        points[1] = LPoint_Set(Translation.x + L/2 + zedH+ l*zedH + 25, Translation.y + 2*W +S - outW + 100);
                        points[2] = LPoint_Set(Translation.x + L/2 + zedH/2+ l*zedH + 100, Translation.y + 2*W +S  - zedH + 400- outW );
                        points[3] = LPoint_Set(Translation.x + L/2 + zedH/2+ l*zedH - 100, Translation.y + 2*W +S - zedH + 400- outW );
                }
                else
                {

                        if (l==0)
                        {
                        points[0] = LPoint_Set(Translation.x + L/2 + l*zedH  , Translation.y + 2*W +S - down - down/2-W);
                        points[1] = LPoint_Set(Translation.x + L/2 + l*zedH, Translation.y + 2*W +S - down - down/2- zedH*2-W);
                        points[2] = LPoint_Set(Translation.x + L/2 + zedH+ l*zedH, Translation.y + 2*W +S - down- down/2 - zedH*2-W);
                        }
                        else
                        {
```

```
                        points[0] = LPoint_Set(Translation.x + L/2 + l*zedH  , Translation.y + 2*W +S - down -W);
                        points[1] = LPoint_Set(Translation.x + L/2 + l*zedH, Translation.y + 2*W +S - down - zedH*2 -W);
                        points[2] = LPoint_Set(Translation.x + L/2 + zedH+ l*zedH, Translation.y + 2*W +S - down - zedH*2-W);
                        }

                        Box = LPolygon_New ( Cell_Draw, LLayer_Find ( File_Draw, "Poly" ), points, 3 );
                        LSelection_AddObject (Box);

                        points[0] = LPoint_Set(Translation.x + L/2+ l*zedH, Translation.y + 2*W +S - down - zedH*2-W);
                        points[1] = LPoint_Set(Translation.x + L/2 + zedH+ l*zedH, Translation.y + 2*W +S - down-W);
                        points[2] = LPoint_Set(Translation.x + L/2 + zedH+ l*zedH, Translation.y + 2*W +S - down - zedH*2-W);

                        Box = LPolygon_New ( Cell_Draw, LLayer_Find ( File_Draw, "Poly" ), points, 3 );
                        LSelection_AddObject (Box);


                        points[0] = LPoint_Set(Translation.x + L/2+ l*zedH - 25, Translation.y + 2*W +S  + 100 -W  );
                        points[1] = LPoint_Set(Translation.x + L/2 + zedH+ l*zedH + 25, Translation.y + 2*W +S  + 100 -W);
                        points[2] = LPoint_Set(Translation.x + L/2 + zedH/2+ l*zedH + 100, Translation.y + 2*W +S  - zedH + 400 -W );
                        points[3] = LPoint_Set(Translation.x + L/2 + zedH/2+ l*zedH - 100, Translation.y + 2*W +S - zedH + 400 -W );
                }


                Box = LPolygon_New ( Cell_Draw, LLayer_Find ( File_Draw, "Poly" ), points, 4 );
                LSelection_AddObject (Box);

                } while (l < zedNo -1);

Box = LBox_New (  Cell_Draw, LLayer_Find ( File_Draw, "Poly" ),
                        Translation.x + L/2 , Translation.y + (2*j+1)*(W +S)  , Translation.x +L/2 - AnchorX, Translation.y +(2*j+1)*(W+S) +
                        AnchorX );
LSelection_AddObject (Box);

}
else if (hex ==1)
{

                hexNo = (AnchorX- 400) / (0.8660254038*(2*hexS + 2*hexA)) + 1;
                AnchorX = 0.8660254038*(2*hexS + 2*hexA)*(hexNo+1) ;


                m=-1;
                do {m++;
                l = -1;

                points[0] = LPoint_Set(Translation.x + L/2  , Translation.y + 2*W +S -m*0.8660254038*(2*hexS + 2*hexA));
                points[1] = LPoint_Set(Translation.x + L/2  , Translation.y + 2*W +S- (hexS*0.8660254038 + hexA*0.8660254038) +
                4*0.8660254038*hexS -m*0.8660254038*(2*hexS + 2*hexA));
                points[2] = LPoint_Set(Translation.x + L/2  + hexA/2 - 1.5* hexS  , Translation.y + 2*W +S -m*0.8660254038*(2*hexS + 2*hexA));

                Box = LPolygon_New ( Cell_Draw, LLayer_Find ( File_Draw, "Poly" ), points, 3 );
                LSelection_AddObject (Box);

                points[0] = LPoint_Set(Translation.x + L/2  , Translation.y + 2*W +S - (hexS*0.8660254038 + hexA*0.8660254038) -
                4*0.8660254038*hexS -m*0.8660254038*(2*hexS + 2*hexA));
                points[1] = LPoint_Set(Translation.x + L/2  , Translation.y + 2*W +S- 2*(hexS*0.8660254038 + hexA*0.8660254038)  -m*0.8660254038*
                (2*hexS + 2*hexA));
                points[2] = LPoint_Set(Translation.x + L/2 + hexA/2 - 1.5* hexS  , Translation.y + 2*W +S- 2*(hexS*0.8660254038 +
                hexA*0.8660254038)  -m*0.8660254038*(2*hexS + 2*hexA));

                Box = LPolygon_New ( Cell_Draw, LLayer_Find ( File_Draw, "Poly" ), points, 3 );
                LSelection_AddObject (Box);

                Temp.y = Translation.y;
                Translation.y = Translation.y + AnchorX + (2*j)*(W +S)-W ;

                points[0] = LPoint_Set(Translation.x + L/2  , Translation.y + 2*W +S -m*0.8660254038*(2*hexS + 2*hexA));
                points[1] = LPoint_Set(Translation.x + L/2  , Translation.y + 2*W +S- (hexS*0.8660254038 + hexA*0.8660254038) +
                4*0.8660254038*hexS -m*0.8660254038*(2*hexS + 2*hexA));
                points[2] = LPoint_Set(Translation.x + L/2  - hexA/2 + 1.5* hexS  , Translation.y + 2*W +S -m*0.8660254038*(2*hexS + 2*hexA));

                Box = LPolygon_New ( Cell_Draw, LLayer_Find ( File_Draw, "Poly" ), points, 3 );
                LSelection_AddObject (Box);

                points[0] = LPoint_Set(Translation.x + L/2  , Translation.y + 2*W +S - (hexS*0.8660254038 + hexA*0.8660254038) -
                4*0.8660254038*hexS -m*0.8660254038*(2*hexS + 2*hexA));
                points[1] = LPoint_Set(Translation.x + L/2  , Translation.y + 2*W +S- 2*(hexS*0.8660254038 + hexA*0.8660254038)  -m*0.8660254038*
                (2*hexS + 2*hexA));
                points[2] = LPoint_Set(Translation.x + L/2 - hexA/2 + 1.5* hexS  , Translation.y + 2*W +S- 2*(hexS*0.8660254038 +
                hexA*0.8660254038)  -m*0.8660254038*(2*hexS + 2*hexA));

                Box = LPolygon_New ( Cell_Draw, LLayer_Find ( File_Draw, "Poly" ), points, 3 );
                LSelection_AddObject (Box);

                Translation.y = Temp.y ;
```

```
do {l++;


points[0] = LPoint_Set(Translation.x + L/2 +l*(3*(hexA + hexS)) , Translation.y + 2*W +S - (hexS*0.8660254038 + hexA*0.8660254038)-
m*0.8660254038*(2*hexS + 2*hexA));
points[1] = LPoint_Set(Translation.x + L/2 + hexA*2+l*(3*(hexA + hexS)), Translation.y + 2*W +S - (hexS*0.8660254038 +
hexA*0.8660254038)-m*0.8660254038*(2*hexS + 2*hexA));
points[2] = LPoint_Set(Translation.x + L/2 + hexA*1.5 +l*(3*(hexA + hexS)), Translation.y + 2*W +S – hexS*0.8660254038-
m*0.8660254038*(2*hexS + 2*hexA));
points[3] = LPoint_Set(Translation.x + L/2 + hexA*0.5 +l*(3*(hexA + hexS)), Translation.y + 2*W +S – hexS*0.8660254038-
m*0.8660254038*(2*hexS + 2*hexA));

Box = LPolygon_New ( Cell_Draw, LLayer_Find ( File_Draw, "Poly" ), points, 4 );
LSelection_AddObject (Box);

points[0] = LPoint_Set(Translation.x + L/2 + 1.5*hexA + 1.5*hexS  +l*(3*(hexA + hexS)), Translation.y + 2*W +S-
m*0.8660254038*(2*hexS + 2*hexA));
points[1] = LPoint_Set(Translation.x + L/2 + 1.5*hexA + 1.5*hexS + 2*hexA +l*(3*(hexA + hexS)), Translation.y + 2*W +S-
m*0.8660254038*(2*hexS + 2*hexA));
points[2] = LPoint_Set(Translation.x + L/2 + 1.5*hexA + 1.5*hexS + 1.5*hexA  +l*(3*(hexA + hexS)), Translation.y + 2*W +S
-hexA*0.8660254038 -m*0.8660254038*(2*hexS + 2*hexA));
points[3] = LPoint_Set(Translation.x + L/2 + 1.5*hexA + 1.5*hexS + 0.5*hexA +l*(3*(hexA + hexS)) , Translation.y + 2*W +S
-hexA*0.8660254038 -m*0.8660254038*(2*hexS + 2*hexA));

Box = LPolygon_New ( Cell_Draw, LLayer_Find ( File_Draw, "Poly" ), points, 4 );
LSelection_AddObject (Box);

points[0] = LPoint_Set(Translation.x + L/2 +l*(3*(hexA + hexS)) , Translation.y + 2*W +S - (hexS*0.8660254038 + hexA*0.8660254038)-
m*0.8660254038*(2*hexS + 2*hexA));
points[1] = LPoint_Set(Translation.x + L/2 + hexA*2+l*(3*(hexA + hexS)), Translation.y + 2*W +S - (hexS*0.8660254038 +
hexA*0.8660254038)-m*0.8660254038*(2*hexS + 2*hexA));
points[2] = LPoint_Set(Translation.x + L/2 + hexA*1.5 +l*(3*(hexA + hexS)), Translation.y + 2*W +S - (hexS*0.8660254038 +
2*hexA*0.8660254038)-m*0.8660254038*(2*hexS + 2*hexA));
points[3] = LPoint_Set(Translation.x + L/2 + hexA*0.5 +l*(3*(hexA + hexS)), Translation.y + 2*W +S - (hexS*0.8660254038 +
2*hexA*0.8660254038)-m*0.8660254038*(2*hexS + 2*hexA));

Box = LPolygon_New ( Cell_Draw, LLayer_Find ( File_Draw, "Poly" ), points, 4 );
LSelection_AddObject (Box);

points[0] = LPoint_Set(Translation.x + L/2 + 1.5*hexA + 1.5*hexS  +l*(3*(hexA + hexS)), Translation.y + 2*W +S - 0.8660254038 *
(hexA+hexS)*2 -m*0.8660254038*(2*hexS + 2*hexA));
points[1] = LPoint_Set(Translation.x + L/2 + 1.5*hexA + 1.5*hexS + 2*hexA +l*(3*(hexA + hexS)), Translation.y + 2*W +S -
0.8660254038 * (hexA+hexS)*2-m*0.8660254038*(2*hexS + 2*hexA));
points[2] = LPoint_Set(Translation.x + L/2 + 1.5*hexA + 1.5*hexS + 1.5*hexA  +l*(3*(hexA + hexS)), Translation.y + 2*W +S
-hexA*0.8660254038 - 2*hexS*0.8660254038  -m*0.8660254038*(2*hexS + 2*hexA));
points[3] = LPoint_Set(Translation.x + L/2 + 1.5*hexA + 1.5*hexS + 0.5*hexA +l*(3*(hexA + hexS)) , Translation.y + 2*W +S
-hexA*0.8660254038 - 2*hexS*0.8660254038-m*0.8660254038*(2*hexS + 2*hexA) );

Box = LPolygon_New ( Cell_Draw, LLayer_Find ( File_Draw, "Poly" ), points, 4 );
LSelection_AddObject (Box);

/*top anch*/
Temp.y = Translation.y;
Translation.y = Translation.y + AnchorX + (2*j)*(W +S)-W ;

points[0] = LPoint_Set(Translation.x + L/2 -l*(3*(hexA + hexS)) , Translation.y + 2*W +S - (hexS*0.8660254038 + hexA*0.8660254038)-
m*0.8660254038*(2*hexS + 2*hexA));
points[1] = LPoint_Set(Translation.x + L/2 - hexA*2-l*(3*(hexA + hexS)), Translation.y + 2*W +S - (hexS*0.8660254038 +
hexA*0.8660254038)-m*0.8660254038*(2*hexS + 2*hexA));
points[2] = LPoint_Set(Translation.x + L/2 - hexA*1.5 -l*(3*(hexA + hexS)), Translation.y + 2*W +S – hexS*0.8660254038-
m*0.8660254038*(2*hexS + 2*hexA));
points[3] = LPoint_Set(Translation.x + L/2 - hexA*0.5 -l*(3*(hexA + hexS)), Translation.y + 2*W +S – hexS*0.8660254038-
m*0.8660254038*(2*hexS + 2*hexA));

Box = LPolygon_New ( Cell_Draw, LLayer_Find ( File_Draw, "Poly" ), points, 4 );
LSelection_AddObject (Box);

points[0] = LPoint_Set(Translation.x + L/2 - 1.5*hexA - 1.5*hexS  -l*(3*(hexA + hexS)), Translation.y + 2*W +S-
m*0.8660254038*(2*hexS + 2*hexA));
points[1] = LPoint_Set(Translation.x + L/2 - 1.5*hexA - 1.5*hexS - 2*hexA -l*(3*(hexA + hexS)), Translation.y + 2*W +S-
m*0.8660254038*(2*hexS + 2*hexA));
points[2] = LPoint_Set(Translation.x + L/2 - 1.5*hexA - 1.5*hexS - 1.5*hexA -l*(3*(hexA + hexS)), Translation.y + 2*W +S
-hexA*0.8660254038 -m*0.8660254038*(2*hexS + 2*hexA));
points[3] = LPoint_Set(Translation.x + L/2 - 1.5*hexA - 1.5*hexS - 0.5*hexA -l*(3*(hexA + hexS)) , Translation.y + 2*W +S
-hexA*0.8660254038 -m*0.8660254038*(2*hexS + 2*hexA));

Box = LPolygon_New ( Cell_Draw, LLayer_Find ( File_Draw, "Poly" ), points, 4 );
LSelection_AddObject (Box);

points[0] = LPoint_Set(Translation.x + L/2 -l*(3*(hexA + hexS)) , Translation.y + 2*W +S - (hexS*0.8660254038 + hexA*0.8660254038)-
m*0.8660254038*(2*hexS + 2*hexA));
points[1] = LPoint_Set(Translation.x + L/2 - hexA*2-l*(3*(hexA + hexS)), Translation.y + 2*W +S - (hexS*0.8660254038 +
hexA*0.8660254038)-m*0.8660254038*(2*hexS + 2*hexA));
points[2] = LPoint_Set(Translation.x + L/2 - hexA*1.5 -l*(3*(hexA + hexS)), Translation.y + 2*W +S - (hexS*0.8660254038 +
2*hexA*0.8660254038)-m*0.8660254038*(2*hexS + 2*hexA));
```

```
points[3] = LPoint_Set(Translation.x + L/2 - hexA*0.5 -l*(3*(hexA + hexS)), Translation.y + 2*W +S - (hexS*0.8660254038 +
2*hexA*0.8660254038)-m*0.8660254038*(2*hexS + 2*hexA));

Box = LPolygon_New ( Cell_Draw, LLayer_Find ( File_Draw, "Poly" ), points, 4 );
LSelection_AddObject (Box);

points[0] = LPoint_Set(Translation.x + L/2 - 1.5*hexA - 1.5*hexS -l*(3*(hexA + hexS)), Translation.y + 2*W +S - 0.8660254038 *
(hexA+hexS)*2 -m*0.8660254038*(2*hexS + 2*hexA));
points[1] = LPoint_Set(Translation.x + L/2 - 1.5*hexA - 1.5*hexS - 2*hexA -l*(3*(hexA + hexS)), Translation.y + 2*W +S - 0.8660254038
* (hexA+hexS)*2-m*0.8660254038*(2*hexS + 2*hexA));
points[2] = LPoint_Set(Translation.x + L/2 - 1.5*hexA - 1.5*hexS - 1.5*hexA  -l*(3*(hexA + hexS)), Translation.y + 2*W +S
-hexA*0.8660254038 - 2*hexS*0.8660254038  -m*0.8660254038*(2*hexS + 2*hexA));
points[3] = LPoint_Set(Translation.x + L/2 - 1.5*hexA - 1.5*hexS - 0.5*hexA -l*(3*(hexA + hexS)) , Translation.y + 2*W +S
-hexA*0.8660254038 - 2*hexS*0.8660254038-m*0.8660254038*(2*hexS + 2*hexA) );

Box = LPolygon_New ( Cell_Draw, LLayer_Find ( File_Draw, "Poly" ), points, 4 );
LSelection_AddObject (Box);

Translation.y = Temp.y ;

} while (l < (hexNo/(2*0.8660254038))-2 );

l ++;
points[0] = LPoint_Set(Translation.x + L/2 +l*(3*(hexA + hexS)) , Translation.y + 2*W +S - (hexS*0.8660254038 + hexA*0.8660254038)-
m*0.8660254038*(2*hexS + 2*hexA));
points[1] = LPoint_Set(Translation.x + L/2 + hexA*2+l*(3*(hexA + hexS)), Translation.y + 2*W +S - (hexS*0.8660254038 +
hexA*0.8660254038)-m*0.8660254038*(2*hexS + 2*hexA));
points[2] = LPoint_Set(Translation.x + L/2 + hexA*1.5 +l*(3*(hexA + hexS)), Translation.y + 2*W +S – hexS*0.8660254038-
m*0.8660254038*(2*hexS + 2*hexA));
points[3] = LPoint_Set(Translation.x + L/2 + hexA*0.5 +l*(3*(hexA + hexS)), Translation.y + 2*W +S – hexS*0.8660254038-
m*0.8660254038*(2*hexS + 2*hexA));

Box = LPolygon_New ( Cell_Draw, LLayer_Find ( File_Draw, "Poly" ), points, 4 );
LSelection_AddObject (Box);

points[0] = LPoint_Set(Translation.x + L/2 +l*(3*(hexA + hexS)) , Translation.y + 2*W +S - (hexS*0.8660254038 + hexA*0.8660254038)-
m*0.8660254038*(2*hexS + 2*hexA));
points[1] = LPoint_Set(Translation.x + L/2 + hexA*2+l*(3*(hexA + hexS)), Translation.y + 2*W +S - (hexS*0.8660254038 +
hexA*0.8660254038)-m*0.8660254038*(2*hexS + 2*hexA));
points[2] = LPoint_Set(Translation.x + L/2 + hexA*1.5 +l*(3*(hexA + hexS)), Translation.y + 2*W +S - (hexS*0.8660254038 +
2*hexA*0.8660254038)-m*0.8660254038*(2*hexS + 2*hexA));
points[3] = LPoint_Set(Translation.x + L/2 + hexA*0.5 +l*(3*(hexA + hexS)), Translation.y + 2*W +S - (hexS*0.8660254038 +
2*hexA*0.8660254038)-m*0.8660254038*(2*hexS + 2*hexA));

Box = LPolygon_New ( Cell_Draw, LLayer_Find ( File_Draw, "Poly" ), points, 4 );
LSelection_AddObject (Box);

Temp.y = Translation.y;
Translation.y = Translation.y + AnchorX + (2*j)*(W +S)-W ;

points[0] = LPoint_Set(Translation.x + L/2 -l*(3*(hexA + hexS)) , Translation.y + 2*W +S - (hexS*0.8660254038 + hexA*0.8660254038)-
m*0.8660254038*(2*hexS + 2*hexA));
points[1] = LPoint_Set(Translation.x + L/2 - hexA*2-l*(3*(hexA + hexS)), Translation.y + 2*W +S - (hexS*0.8660254038 +
hexA*0.8660254038)-m*0.8660254038*(2*hexS + 2*hexA));
points[2] = LPoint_Set(Translation.x + L/2 - hexA*1.5 -l*(3*(hexA + hexS)), Translation.y + 2*W +S – hexS*0.8660254038-
m*0.8660254038*(2*hexS + 2*hexA));
points[3] = LPoint_Set(Translation.x + L/2 - hexA*0.5 -l*(3*(hexA + hexS)), Translation.y + 2*W +S – hexS*0.8660254038-
m*0.8660254038*(2*hexS + 2*hexA));

Box = LPolygon_New ( Cell_Draw, LLayer_Find ( File_Draw, "Poly" ), points, 4 );
LSelection_AddObject (Box);

points[0] = LPoint_Set(Translation.x + L/2 -l*(3*(hexA + hexS)) , Translation.y + 2*W +S - (hexS*0.8660254038 + hexA*0.8660254038)-
m*0.8660254038*(2*hexS + 2*hexA));
points[1] = LPoint_Set(Translation.x + L/2 - hexA*2-l*(3*(hexA + hexS)), Translation.y + 2*W +S - (hexS*0.8660254038 +
hexA*0.8660254038)-m*0.8660254038*(2*hexS + 2*hexA));
points[2] = LPoint_Set(Translation.x + L/2 - hexA*1.5 -l*(3*(hexA + hexS)), Translation.y + 2*W +S - (hexS*0.8660254038 +
2*hexA*0.8660254038)-m*0.8660254038*(2*hexS + 2*hexA));
points[3] = LPoint_Set(Translation.x + L/2 - hexA*0.5 -l*(3*(hexA + hexS)), Translation.y + 2*W +S - (hexS*0.8660254038 +
2*hexA*0.8660254038)-m*0.8660254038*(2*hexS + 2*hexA));

Box = LPolygon_New ( Cell_Draw, LLayer_Find ( File_Draw, "Poly" ), points, 4 );
LSelection_AddObject (Box);

Translation.y = Temp.y;


l = l-1;
} while (m < hexNo);


}
else if (bac==1)
{
```

```
                              /* up, left, down, right are assumed to be equal !!!! */

                              Box = LBox_New ( Cell_Draw, LLayer_Find ( File_Draw, "Poly" ),
                                                      Translation.x + L/2 , Translation.y + 2*W +S  , Translation.x + L/2+ AnchorX, Translation.y +2*W +S
                              - AnchorX );
                              LSelection_AddObject (Box);

                              Box = LBox_New ( Cell_Draw, LLayer_Find ( File_Draw, "Poly" ),
                                                      Translation.x + L/2 , Translation.y + (2*j+1)*(W +S)  , Translation.x +L/2 - AnchorX, Translation.y
                              +(2*j+1)*(W+S) +  AnchorX );
                              LSelection_AddObject (Box);

                              /*to be cont..*/

}


LSelection_Duplicate ();
LSelection_FlipHorizontal ();
LSelection_Move ((AnchorX)*2, 0);
LSelection_Duplicate ();
LSelection_FlipHorizontal ();
LSelection_Move (0, (2*j)*(W+S) - W  +  (AnchorX)*2 );
LSelection_Duplicate ();
LSelection_FlipHorizontal ();
LSelection_Move (-(AnchorX)*2, 0);

LSelection_DeselectAll ();

if (res==1)
{
              /*draw side fins where needed */
if (Iside == 1 && TopSide == 0)
{


i=0;
              do
              {         i++;


                              Box = LBox_New ( Cell_Draw, LLayer_Find ( File_Draw, "Poly" ),
                                                      Translation.x -W , Translation.y+ ((2*i-1)*(W+S)) +W, Translation.x - W-S , Translation.y +
                              ((2*i)*(W+S)));
                              LSelection_AddObject (Box);
                              Box = LBox_New ( Cell_Draw, LLayer_Find ( File_Draw, "Poly" ),
                                                      Translation.x - W-S , Translation.y  + ((2*i-1)*(W+S)) , Translation.x - W-S-finH  , Translation.y +
                              ((2*i)*(W+S))+ W);
                              LSelection_AddObject (Box);

                              if (both != 0)
                              {
                              Box = LBox_New ( Cell_Draw, LLayer_Find ( File_Draw, "Poly" ),
                                                      Translation.x + L +W  , Translation.y + ((2*i)*(W+S)) + W , Translation.x + L+W +S, Translation.y  +
                              ((2*i+1)*(W+S)));
                              LSelection_AddObject (Box);
                              Box = LBox_New ( Cell_Draw, LLayer_Find ( File_Draw, "Poly" ),
                                                      Translation.x  + L +W +S , Translation.y + ((2*i)*(W+S)) , Translation.x + L+W +S+finH ,
                              Translation.y + ((2*i+1)*(W+S)) +W );
                              LSelection_AddObject (Box);
                              }
              } while (i < j);
if (m1==1) LSelection_Duplicate ();
LSelection_FlipHorizontal ();
LSelection_Move ((AnchorX)*2, 0);

if (m2==1) LSelection_Duplicate ();
LSelection_FlipVertical ();
LSelection_Move (0, (2*j)*(W+S) - W  +  (AnchorX)*2 );

if (m3==1) LSelection_Duplicate ();
LSelection_FlipHorizontal ();
LSelection_Move (-(AnchorX)*2, 0);

if (m4==0) LSelection_Clear ();

LSelection_DeselectAll ();
}

/* draw normal mids on poly layer */


              /*draw 1 set of normal mid points and move to where needed according to m1-4 */
i=0;
do {         i++;
```

```
                if (Tmid2 == 0)
                {
                        Box = LBox_New ( Cell_Draw, LLayer_Find ( File_Draw, "Poly" ),
                                Translation.x + L/2- midH/2  + (right + left + S - up - down)/2, Translation.y  + ((2*i-1)*(W+S)) , Translation.x +
                        L/2 + midH/2- (right + left + S - up - down)/2, Translation.y  + ((2*i-1)*(W+S)) + W );
                        LSelection_AddObject (Box);

                        Box = LBox_New ( Cell_Draw, LLayer_Find ( File_Draw, "Poly" ),
                                Translation.x + L/2- midH/2 - (right + left + S - up - down)/2 - overL , Translation.y + ((2*i)*(W+S)), Translation.x
                        + L/2 + midH/2+ (right + left + S - up - down)/2 + overL , Translation.y + ((2*i)*(W+S)) + W);
                        LSelection_AddObject (Box);


                        if (i ==j)
                        {
                        Box = LBox_New ( Cell_Draw, LLayer_Find ( File_Draw, "Poly" ),
                                        Translation.x  + L/2- midH/2 + (right + left + S - up - down)/2 , Translation.y  + ((2*i+1)*(W+S)) ,
                        Translation.x + L/2 + midH/2- (right + left + S - up - down)/2 , Translation.y + ((2*i+1)*(W+S)) + W );
                        LSelection_AddObject (Box);
                        }
                }
                else
                {

                        if (zedE == 1 && i==1)
                        {
                                Box = LBox_New ( Cell_Draw, LLayer_Find ( File_Draw, "Poly" ),
                                        Translation.x + L/2- midH/2 - (right + left + S - up - down)/2 - overL ,
                                Translation.y  + ((2*i-1)*(W+S)) , Translation.x + L/2 + (right + left + S - up - down)/2 + overL, Translation.y +
                                ((2*i-1)*(W+S)) + W );
                                LSelection_AddObject (Box);

                                Box = LBox_New ( Cell_Draw, LLayer_Find ( File_Draw, "Poly" ),
                                                Translation.x + L/2- midH/2 - (right + left + S - up - down)/2 - overL , Translation.y +
                                ((2*i)*(W+S)), Translation.x + L/2 + midH/2+ (right + left + S - up - down)/2 + overL , Translation.y +
                                ((2*i)*(W+S)) + W);
                                LSelection_AddObject (Box);
                        }
                        else
                        {
                                Box = LBox_New ( Cell_Draw, LLayer_Find ( File_Draw, "Poly" ),
                                                Translation.x + L/2- midH/2 - (right + left + S - up - down)/2 - overL ,
                                Translation.y  + ((2*i-1)*(W+S)) , Translation.x + L/2 + midH/2+ (right + left + S - up - down)/2 + overL,
                                Translation.y  + ((2*i-1)*(W+S)) + W );
                                LSelection_AddObject (Box);

                                Box = LBox_New ( Cell_Draw, LLayer_Find ( File_Draw, "Poly" ),
                                                Translation.x + L/2- midH/2 - (right + left + S - up - down)/2 - overL , Translation.y +
                                ((2*i)*(W+S)), Translation.x + L/2 + midH/2+ (right + left + S - up - down)/2 + overL , Translation.y +
                                ((2*i)*(W+S)) + W);
                                LSelection_AddObject (Box);
                        }

                        if (i ==j)
                        {
                        Box = LBox_New ( Cell_Draw, LLayer_Find ( File_Draw, "Poly" ),
                                Translation.x + L/2 - midH/2 - (right + left + S - up - down)/2 - overL , Translation.y +
                                ((2*i+1)*(W+S)) , Translation.x + L/2 + midH/2+ (right + left + S - up - down)/2 + overL , Translation.y +
                                ((2*i+1)*(W+S)) + W );
                        LSelection_AddObject (Box);
                        }
                }

        } while (i < j);
        if (m1==0 || (Imid ==0 && Tmid2 == 0)) LSelection_Duplicate ();
        LSelection_FlipHorizontal ();
        LSelection_Move ((AnchorX)*2, 0);
        if (m2==0 || (Imid ==0 && Tmid2 == 0)) LSelection_Duplicate ();
        LSelection_FlipHorizontal ();
        LSelection_Move (0, (2*j)*(W+S) - W  +  (AnchorX)*2 );
        if (m3==0 || (Imid ==0 && Tmid2 == 0)) LSelection_Duplicate ();
        LSelection_FlipHorizontal ();
        LSelection_Move (-(AnchorX)*2, 0);
        if (m4==1 && (Imid ==1 || Tmid2 == 1)) LSelection_Clear ();


        LSelection_DeselectAll ();

                /*draw 1 set of wide/narrow mid points and move to where needed according to m1-4 */
        i=0;
        do {    i++;

                if (i>1)
                {
```

```
Box = LBox_New ( Cell_Draw, LLayer_Find ( File_Draw, "Poly" ),
                  Translation.x + L/2- midH/2 + (right + left + S - up - down)/2 , Translation.y + ((2*i-1)*(W+S)) - midW ,
Translation.x + L/2 + midH/2 - (right + left + S - up - down)/2 , Translation.y + ((2*i-1)*(W+S)) + W + midW );
LSelection_AddObject (Box);
}
else
{
Box = LBox_New ( Cell_Draw, LLayer_Find ( File_Draw, "Poly" ),
          Translation.x+ L/2- midH/2 + (right + left + S - up - down)/2 , Translation.y + ((2*i-1)*(W+S))  , Translation.x +
          L/2 + midH/2 -(right + left + S - up - down)/2, Translation.y + ((2*i-1)*(W+S)) + W + midW );
LSelection_AddObject (Box);
}


Box = LBox_New ( Cell_Draw, LLayer_Find ( File_Draw, "Poly" ),
          Translation.x + L/2- midH/2 - (right + left + S - up - down)/2 - overL, Translation.y + ((2*i)*(W+S)) + midW  , Translation.x +
          L/2 + midH/2+ (right + left + S - up - down)/2 + overL, Translation.y + ((2*i)*(W+S)) + W - midW );
LSelection_AddObject (Box);

if (i ==j)
{
Box = LBox_New ( Cell_Draw, LLayer_Find ( File_Draw, "Poly" ),
          Translation.x + L/2- midH/2 + (right + left + S - up - down)/2 , Translation.y + ((2*i+1)*(W+S)) - midW  , Translation.x + L/2 +
          midH/2 -(right + left + S - up - down)/2, Translation.y + ((2*i+1)*(W+S)) + W);
LSelection_AddObject (Box);
}


} while (i < j);

if (m1==1 && Imid==1) LSelection_Duplicate ();
LSelection_FlipHorizontal ();
LSelection_Move ((AnchorX)*2, 0);
if (m2==1 && Imid==1) LSelection_Duplicate ();
LSelection_FlipHorizontal();
LSelection_Move (0, (2*j)*(W+S) - W  +  (AnchorX)*2 );
if (m3==1 && Imid==1) LSelection_Duplicate ();
LSelection_FlipHorizontal ();
LSelection_Move (-(AnchorX)*2, 0);
if (m4==0 || Imid==0) LSelection_Clear ();

LSelection_DeselectAll ();

/*end draw normal mids on Poly layer*/

/* draw overlap mids on bottom layer*/
i=0;
do {        i++;

        if (zedE==1 && i ==1)
        {
                Box = LBox_New ( Cell_Draw, LLayer_Find ( File_Draw, "Poly" ),
                Translation.x + L/2- midH/2 - (right + left + S - up - down)/2 - overL , Translation.y   + ((2*i-
                1)*(W+S)) , Translation.x + L/2 + (right + left + S - up - down)/2 + overL, Translation.y + ((2*i-1)*(W+S)) + W- midW );
                LSelection_AddObject (Box);

                Box = LBox_New ( Cell_Draw, LLayer_Find ( File_Draw, "Poly" ),
                Translation.x + L/2- midH/2 - (right + left + S - up - down)/2 - overL , Translation.y + ((2*i)*(W+S)) , Translation.x + L/2 +
                midH/2+ (right + left + S - up - down)/2 + overL , Translation.y + ((2*i)*(W+S)) + W - midW);
                LSelection_AddObject (Box);
        }
        else
        {
                Box = LBox_New ( Cell_Draw, LLayer_Find ( File_Draw, "Poly" ),
                Translation.x + L/2- midH/2 - (right + left + S - up - down)/2 - overL , Translation.y   + ((2*i-1)*(W+S)) , Translation.x + L/2 +
                midH/2+ (right + left + S - up - down)/2 + overL, Translation.y  + ((2*i-1)*(W+S)) + W- midW );
                LSelection_AddObject (Box);


                Box = LBox_New ( Cell_Draw, LLayer_Find ( File_Draw, "Poly" ),
                Translation.x + L/2- midH/2 - (right + left + S - up - down)/2 - overL , Translation.y + ((2*i)*(W+S)) , Translation.x + L/2 +
                midH/2+ (right + left + S - up - down)/2 + overL , Translation.y + ((2*i)*(W+S)) + W - midW);
                LSelection_AddObject (Box);


        }


        if (i ==j)
        {
        Box = LBox_New ( Cell_Draw, LLayer_Find ( File_Draw, "Poly" ),
        Translation.x + L/2- midH/2 - (right + left + S - up - down)/2 - overL, Translation.y  + ((2*i+1)*(W+S)) , Translation.x + L/2 + midH/2+
        (right + left + S - up - down)/2 + overL, Translation.y + ((2*i+1)*(W+S)) + W- midW );
        LSelection_AddObject (Box);
        }
```

```
} while (i < j);

if (m1==1 && Tmid2==1) LSelection_Duplicate ();
LSelection_FlipHorizontal ();
LSelection_Move ((AnchorX)*2, 0);
if (m2==1 && Tmid2==1) LSelection_Duplicate ();
LSelection_FlipHorizontal ();
LSelection_Move (0, (2*j)*(W+S) - W  +  (AnchorX)*2 );
if (m3==1 && Tmid2==1) LSelection_Duplicate ();
LSelection_FlipHorizontal ();
LSelection_Move (-(AnchorX)*2, 0);
if (m4==0 || Tmid2==0) LSelection_Clear ();

} /*end res ==1*/

LSelection_DeselectAll ();
/*end draw overlap*/

/*---------------------- top layer begin-----------------------*/

LSelection_DeselectAll ();

            /*draw 4 resistors minus the mid points */
i=0;
do {         i++;

            Box = LBox_New ( Cell_Draw, LLayer_Find ( File_Draw, "Poly2" ),
            Translation.x - left , Translation.y + ((2*i-1)*(W+S)) - down , Translation.x +  L/2- midH/2 + (right + left + S - up - down)/2 + right +
            overL, Translation.y +((2*i-1)*(W+S)) + W + up);
            LSelection_AddObject (Box);



            Box = LBox_New ( Cell_Draw, LLayer_Find ( File_Draw, "Poly2" ),
            Translation.x + right , Translation.y + ((2*i-1)*(W+S)) - down, Translation.x  - W - left, Translation.y + ((2*i)*(W+S)) + W + up);
            LSelection_AddObject (Box);

            Box = LBox_New ( Cell_Draw, LLayer_Find ( File_Draw, "Poly2" ),
            Translation.x - left , Translation.y + ((2*i)*(W+S)) - down , Translation.x  + L/2 - midH/2 - (right + left + S - up - down)/2 + right  ,
            Translation.y + ((2*i)*(W+S)) + W + up );
            LSelection_AddObject (Box);

            Box = LBox_New ( Cell_Draw, LLayer_Find ( File_Draw, "Poly2" ),
            Translation.x  + L/2 + midH/2 + (right + left + S - up - down)/2 - left , Translation.y + ((2*i)*(W+S)) - down , Translation.x + L + right,
            Translation.y + ((2*i)*(W+S)) + W + up);
            LSelection_AddObject (Box);


            Box = LBox_New ( Cell_Draw, LLayer_Find ( File_Draw, "Poly2" ),
            Translation.x+ L -left , Translation.y + ((2*i)*(W+S)) - down , Translation.x + L+W + right, Translation.y + ((2*i+1)*(W+S)) + W + up);
            LSelection_AddObject (Box);


            Box = LBox_New ( Cell_Draw, LLayer_Find ( File_Draw, "Poly2" ),
            Translation.x + L/2 + midH/2 - (right + left + S - up - down)/2 - left - overL, Translation.y + ((2*i+1)*(W+S)) - down, Translation.x+ L +
            right, Translation.y  + ((2*i+1)*(W+S)) + W + up);
            LSelection_AddObject (Box);

} while (i < j);



Box = LBox_New ( Cell_Draw, LLayer_Find ( File_Draw, "Poly2" ),
Translation.x + L/2 -left , Translation.y + 2*W +S + up , Translation.x +  L/2 + AnchorX + right, Translation.y +2*W +S -  AnchorX - down );
LSelection_AddObject (Box);
Box = LBox_New ( Cell_Draw, LLayer_Find ( File_Draw, "Poly2" ),
Translation.x + L/2 + right, Translation.y + (2*j+1)*(W +S)-down , Translation.x +L/2 - AnchorX - left, Translation.y +(2*j+1)*(W+S) +  AnchorX +
up);
LSelection_AddObject (Box);


LSelection_Duplicate ();
LSelection_FlipHorizontal ();
LSelection_Move ((AnchorX)*2, 0);
LSelection_Duplicate ();
LSelection_FlipVertical ();
LSelection_Move (0, (2*j)*(W+S) - W  +  (AnchorX)*2  );
LSelection_Duplicate ();
LSelection_FlipHorizontal ();
LSelection_Move (-(AnchorX)*2 , 0);

LSelection_DeselectAll ();

            /*draw side fins where needed */
if (Iside == 1)
```

```
{
        if (TopSide == 0)
        {
                i=0;
                do
                {       i++;

                        Box = LBox_New ( Cell_Draw, LLayer_Find ( File_Draw, "Poly2" ),
                        Translation.x -W +right , Translation.y+ ((2*i-1)*(W+S)) +W -down, Translation.x - W-S -left, Translation.y +
                        ((2*i)*(W+S)) + up);
                        LSelection_AddObject (Box);
                        Box = LBox_New ( Cell_Draw, LLayer_Find ( File_Draw, "Poly2" ),
                        Translation.x - W-S + right , Translation.y + ((2*i-1)*(W+S)) - down, Translation.x - W-S-finH - left , Translation.y
                        + ((2*i)*(W+S))+ W + up);
                        LSelection_AddObject (Box);

                        if (both != 0)
                        {
                        Box = LBox_New ( Cell_Draw, LLayer_Find ( File_Draw, "Poly2" ),
                        Translation.x + L +W - left , Translation.y + ((2*i)*(W+S)) + W - down, Translation.x + L+W +S +right,
                        Translation.y   ((2*i+1)*(W+S)) + up);
                        LSelection_AddObject (Box);
                        Box = LBox_New ( Cell_Draw, LLayer_Find ( File_Draw, "Poly2" ),
                        Translation.x  + L +W +S - left , Translation.y + ((2*i)*(W+S)) - down , Translation.x + L+W +S+finH + right,
                        Translation.y + ((2*i+1)*(W+S)) +W + up );
                        LSelection_AddObject (Box);
                        }
                } while (i < j);
        }

        if (TopSide == 1)
        {
                i=0;
                do
                {       i++;

                        Box = LBox_New ( Cell_Draw, LLayer_Find ( File_Draw, "Poly2" ),
                        Translation.x -W - left , Translation.y+ ((2*i-1)*(W+S)) +W, Translation.x - W-S -left, Translation.y +
                        ((2*i)*(W+S)) );
                        LSelection_AddObject (Box);
                        Box = LBox_New ( Cell_Draw, LLayer_Find ( File_Draw, "Poly2" ),
                        Translation.x - W-S - left , Translation.y  + ((2*i-1)*(W+S)), Translation.x - W-S-finH - left , Translation.y +
                        ((2*i)*(W+S))+ W );
                        LSelection_AddObject (Box);

                        if (both != 0)
                        {
                        Box = LBox_New ( Cell_Draw, LLayer_Find ( File_Draw, "Poly2" ),
                        Translation.x + L +W + right  , Translation.y + ((2*i)*(W+S)) + W , Translation.x + L+W +S +right, Translation.y
                        + ((2*i+1)*(W+S)) );
                        LSelection_AddObject (Box);
                        Box = LBox_New ( Cell_Draw, LLayer_Find ( File_Draw, "Poly2" ),
                        Translation.x  + L +W +S + right , Translation.y + ((2*i)*(W+S)) , Translation.x + L+W +S+finH + right,
                        Translation.y + ((2*i+1)*(W+S)) +W );
                        LSelection_AddObject (Box);
                        }
                } while (i < j);
        }


    if (m1==1) LSelection_Duplicate ();
    LSelection_FlipHorizontal ();
    LSelection_Move ((AnchorX)*2, 0);

    if (m2==1) LSelection_Duplicate ();
    LSelection_FlipVertical ();
    LSelection_Move (0, (2*j)*(W+S) - W  +  (AnchorX)*2 );

    if (m3==1) LSelection_Duplicate ();
    LSelection_FlipHorizontal ();
    LSelection_Move (-(AnchorX)*2, 0);

    if (m4==0) LSelection_Clear ();

    LSelection_DeselectAll ();
    }


    /* draw normal mids on poly2 layer */

                        /*draw 1 set of normal mid points and move to where needed according to m1-4 */
    i=0;
```

```
do {        i++;

            Box = LBox_New ( Cell_Draw, LLayer_Find ( File_Draw, "Poly2" ),
            Translation.x  + L/2- midH/2  + (right + left + S - up - down)/2 + right, Translation.y -down + ((2*i-1)*(W+S)), Translation.x + L/2 +
            midH/2 - (right + left + S - up - down)/2 - left, Translation.y +up + ((2*i-1)*(W+S)) + W );
            LSelection_AddObject (Box);

            Box = LBox_New ( Cell_Draw, LLayer_Find ( File_Draw, "Poly2" ),
            Translation.x + L/2- midH/2 - (right + left + S - up - down)/2  + right -overL, Translation.y -down + ((2*i)*(W+S)), Translation.x + L/2 +
            midH/2+ (right + left + S - up - down)/2  - left +overL, Translation.y + up + ((2*i)*(W+S)) + W);
            LSelection_AddObject (Box);

            Box = LBox_New ( Cell_Draw, LLayer_Find ( File_Draw, "Poly2" ),
            Translation.x  + L/2- midH/2 + (right + left + S - up - down)/2  + right, Translation.y -down + ((2*i+1)*(W+S)) , Translation.x + L/2 +
            midH/2 - (right + left + S - up - down)/2 - left, Translation.y + up+ ((2*i+1)*(W+S)) + W );
            LSelection_AddObject (Box);

} while (i < j);
if (m1==0 || (Tmid ==0 )) LSelection_Duplicate ();
LSelection_FlipHorizontal ();
LSelection_Move ((AnchorX)*2, 0);
if (m2==0 || (Tmid ==0 )) LSelection_Duplicate ();
LSelection_FlipVertical ();
LSelection_Move (0, (2*j)*(W+S) - W  +  (AnchorX)*2 );
if (m3==0 || (Tmid ==0)) LSelection_Duplicate ();
LSelection_FlipHorizontal ();
LSelection_Move (-(AnchorX)*2, 0);
if (m4==1 && (Tmid ==1 )) LSelection_Clear ();


LSelection_DeselectAll ();

            /*draw 1 set of wide/narrow mid points and move to where needed according to m1-4 */
i=0;
do {        i++;

            if (i>1)
            {
            Box = LBox_New ( Cell_Draw, LLayer_Find ( File_Draw, "Poly2" ),
            Translation.x + L/2- midH/2 + (right + left + S - up - down)/2 - left , Translation.y -down+ ((2*i-1)*(W+S)) - midW , Translation.x + L/2 +
            midH/2 - (right + left + S - up - down)/2 + right , Translation.y +up + ((2*i-1)*(W+S)) + W + midW );
            LSelection_AddObject (Box);
            }
            else
            {
            Box = LBox_New ( Cell_Draw, LLayer_Find ( File_Draw, "Poly2" ),
            Translation.x + L/2- midH/2 + (right + left + S - up - down)/2 - left , Translation.y -down+ ((2*i-1)*(W+S))  , Translation.x + L/2 + midH/2 -
            (right + left + S - up - down)/2 + right, Translation.y +up+ ((2*i-1)*(W+S)) + W + midW );
            LSelection_AddObject (Box);
            }


            Box = LBox_New ( Cell_Draw, LLayer_Find ( File_Draw, "Poly2" ),
            Translation.x+ L/2- midH/2 - (right + left + S - up - down)/2 + right -overL , Translation.y -down+ ((2*i)*(W+S)) + midW  , Translation.x +
            L/2 + midH/2+ (right + left + S - up - down)/2 - left + overL, Translation.y +up+ ((2*i)*(W+S)) + W - midW );
            LSelection_AddObject (Box);

            if (i ==j)
            {
            Box = LBox_New ( Cell_Draw, LLayer_Find ( File_Draw, "Poly2" ),
            Translation.x + L/2- midH/2 + (right + left + S - up - down)/2 - left , Translation.y -down+ ((2*i+1)*(W+S)) - midW  , Translation.x + L/2 +
            midH/2 - (right + left + S - up - down)/2 + right, Translation.y +up+ ((2*i+1)*(W+S)) + W);
            LSelection_AddObject (Box);
            }


} while (i < j);

if (m1==1 && Tmid==1) LSelection_Duplicate ();
LSelection_FlipHorizontal ();
LSelection_Move ((AnchorX)*2, 0);
if (m2==1 && Tmid==1) LSelection_Duplicate ();
LSelection_FlipVertical ();
LSelection_Move (0, (2*j)*(W+S) - W  +  (AnchorX)*2 );
if (m3==1 && Tmid==1) LSelection_Duplicate ();
LSelection_FlipHorizontal ();
LSelection_Move (-(AnchorX)*2, 0);
if (m4==0 || Tmid==0) LSelection_Clear ();

LSelection_DeselectAll ();

/*overlap????*/

if (Tmid2A==0)
{
```

```
                    i=0;
                    do {        i++;

                            Box = LBox_New ( Cell_Draw, LLayer_Find ( File_Draw, "Poly2" ),
                            Translation.x + L/2- midH/2 - (right + left + S - up - down)/2 , Translation.y + ((2*i +1)*(W+S)) - down + overL , Translation.x
                            + L/2 + midH/2+ (right + left + S - up - down)/2 , Translation.y + ((2*i +1)*(W+S)) -down - midW);
                            LSelection_AddObject (Box);


                    } while (i < j);
            }
            else
            {
                    Box = LBox_New ( Cell_Draw, LLayer_Find ( File_Draw, "Poly2" ),
                    Translation.x + L/2- midH/2 - (right + left + S - up - down)/2 , Translation.y + W/2 +(W+S) , Translation.x + L/2 + midH/2+ (right + left + S
                    - up - down)/2 , Translation.y + (2*j+1)*(W+S) +W/2  );
                    LSelection_AddObject (Box);
            }


            if (m1==1 && Tmid2==1) LSelection_Duplicate ();
            LSelection_FlipHorizontal ();
            LSelection_Move ((AnchorX)*2, 0);
            if (m2==1 && Tmid2==1) LSelection_Duplicate ();
            /*LSelection_FlipVertical ();*/
            LSelection_Move (0, (2*j)*(W+S) - W  +  (AnchorX)*2 );
            if (m3==1 && Tmid2==1) LSelection_Duplicate ();
            LSelection_FlipHorizontal ();
            LSelection_Move (-(AnchorX)*2, 0);
            if (m4==0 || Tmid2==0) LSelection_Clear ();

            LSelection_DeselectAll ();


            /*overlap end*/

            /*end draw normal mids on Poly2 layer*/

            rect = LRect_Set(Translation.x - AnchorX,Translation.y-AnchorX,Translation.x + 30000 + 3*AnchorX + L/2+ W, Translation.y +4*AnchorX +
            2*(2*j)*(W+S));

                    LSelection_AddAllObjectsInRect (&rect);
                    LSelection_RotateAroundPoint( rot, 0, 0, LTRUE );
                    LSelection_DeselectAll ();


            /*--------------------- top layer end-----------------------*/


} while (j<N2 & L>0 );


        LCell_SetView ( Cell_Draw, LCell_GetMbb ( Cell_Draw ) );

        LCell_GenerateLayersEx00(Cell_Draw, 1000*1000, LLayer_Find ( File_Draw, "Derived Poly" ), LFALSE, LFALSE);

        LSelection_AddAllObjectsOnLayer( LLayer_Find ( File_Draw, "Poly2" ) );
        LSelection_Clear ();
        LSelection_AddAllObjectsOnLayer( LLayer_Find ( File_Draw, "Derived Poly" ) );
        LSelection_ChangeLayer( LLayer_Find ( File_Draw, "Derived Poly" ), LLayer_Find ( File_Draw, "Poly" ) );
        LSelection_DeselectAll ();


}

void  MEMS_macro_register ( void )
{
        LMacro_Register("MEMS", "MEMSmacro");
}


}/* End of Module */
MEMS_macro_register();
```